People's Democratic Republic of Algeria
Ministry of Higher Education and Scientific Research
University of May 8, 1945 - Guelma

College of Science and Technology
Department of Mechanical Engineering
Laboratory of Applied Mechanics of New Materials

Thesis

Submitted in Partial Fulfillment for the Degree of *Doctorate in Third Cycle*

Field: **Sciences & Technology**   Stream: **Mechanical Engineering**
Specialty: **Energy**

Presented by

BOUGHAZI Nahla

Title

Design of Asymmetric Supersonic Propulsion Nozzles:
A Computational Analysis

Date: 29 February 2024

Examination Panel:

Mr. GUENFOUD Salah	Professor	U. 8 Mai 1945, Guelma	President
Mr. HADDAD Abdelkrim	Professor	U. 8 Mai 1945, Guelma	Supervisor
Mr. OULD LAHOUCINE Cherif	Professor	U. 8 Mai 1945, Guelma	Examiner
Mr. KHEZZAR Lyes	Professor	Ecole Nationale Polytechnique, Constantine	Examiner
Mr. HANCHI Samir	Professor	UST Houari Boumediene	Examiner

Academic Year : 2023-2024

ABSTRACT

Air-breathing hypersonic systems require better integration of their constituting elements in order to achieve higher thrust-minus-drag capabilities. Asymmetric supersonic nozzles are pivotal parts of these systems. On the basis of axisymmetric flow-field calculations, a technique for designing complex arbitrary cross-section nozzles is provided. The method of characteristics (MoC) is applied for the design of the original axisymmetric configuration profile having the required length and Mach number. The needed asymmetric profile is then defined at its exit cross-section and described by an adequate number of stations that define its geometry. They are therefore followed back to the throat, resulting in the required asymmetric configuration.

Two asymmetric nozzles were created using this method, one with an elliptic cross-section and a corrugated one. The Ansys-Fluent environment was used to analyze the three-dimensional (3D) flow-fields within the asymmetric profiles, and the k-ω SST turbulence model was applied to close the system required to offset the effect of the boundary layer. The numerical results obtained were compared to those gathered from an analogous elliptical nozzle. They were further compared to the results obtained on the original axisymmetric configuration from which the two asymmetric elliptic and corrugated profiles were generated earlier.

The good agreement obtained between the diverse components of the study provides much credence to the method developed, proving that it is possible to design satisfying asymmetric configurations.

Key words: Asymmetric nozzle, Design, Method of characteristics, Supersonic flow, Computational Fluid Dynamics, Elliptic nozzle, Corrugated nozzle.

———————————————

مُلَخَّــــص

تتطلب الأنظمة التي تستعمل الهواء وتفوق سرعة الصوت تكاملا ٍ أفضل للعناصر المكونة لها من أجل تحقيق قدرات دفع ناقص إعاق. الفوهات الأسرع من الصوت غير المتكافئة هي أجزاء محورية من هذه الأنظمة. على أساس حسابات مجال التدفق المتماثل المحوري ، يوفر البحث الحالي تقنية لتصميم فوهات ذات مقطع عرضي هندسي معقد. يتم تطبيق طريقة الخصائص (Method of Characteristics) لتصميم الفوهة الأصلية المتماثلة المحور والتي تتوفر على الطول ورقم ماخ (Mach) المطلوبين. يتم بعدها تحديد الشكل غير المتماثل المطلوب عند المقطع العرضي المخرجي ويتم تحديد شكله بعدد كاف من النقاط التي يتم متابعتها مرة أخرى إلى حلق الفوهة ، مما يؤدي إلى الشكل الهندسي غير المتماثل المطلوب.

تم تصميم فوهان غير متماثلتان باستخدام هذه الطريقة : واحدة ذات مقطع عرضي بيضاوي الشكل والثانية مموجة الشكل، كما تم استخدام البرنامج الحاسوبي التخصصي (Ansys-Fluent) لتحليل حقول التدفق ثلاثية الأبعاد (3D-) داخل التشكيلات غير المتماثلة ، وتم تطبيق نموذج الاضطراب (k-ω SST) لإغلاق مجموعة المعادلات المطلوب لتعويض تأثير الطبقة الحدودية. تمت مقارنة النتائج العددية التي تم الحصول عليها مع تلك التي تم جمعها من فوهة بيضاوية مماثلة، كما تمت مقارنتها أيضٍ ٍ ا بالنتائج التي تم الحصول عليها في الفوهة الأصلية غير المتماثلة المحوروالتي تم على أساسها إنشاء فوهة ٍ بيضاوية الشكل وأخرى مموجة ٍ .

الإتفاقوللجيد الذي تم الحصول عليه بين مختلف نتائج الدراسة مصداقية ٍ هامـٍـ ة ٍ للطريقة التي تم تطويرها ، مما يثبت أنه من الممكن تصميم فوهات ٍ غير متماثلة ٍ مرضية ٍ .

الكلمات المفتاحية: رئيسية: فوهة غير متماثلة ، تصميم ، طريقة الخصائص ، تدفق فوق صوتي ، ديناميكيات السوائل الحسابية ، فوهة بيضاوية الشكل ، فوهة مموجة الشكل.

RÉSUMÉ

Les engins volant à des vitesses hypersoniques nécessitent une meilleure intégration des éléments qui les constituent afin de résulter en des performances de poussée-moins-traînée plus élevées. Les tuyères supersoniques asymétriques sont des éléments essentiels de ces engins. Sur la base de calculs de champ d'écoulement axisymétrique, une technique de conception de tuyères complexes à section transversale arbitraire est proposée. La méthode des caractéristiques (MoC) est appliquée pour la conception du profil axisymétrique original ayant la longueur et le nombre de Mach requis. Le profil asymétrique nécessaire est ensuite défini au niveau de la section droite de sortie axisymétrique et décrit par un nombre adéquat de points qui définissent sa géométrie. Ces derniers sont donc suivis jusqu'au col de la tuyère résultant ainsi en la configuration asymétrique requise.

En appliquant l'approche développée, deux tuyères asymétriques ont été conçues: l'une de section droite elliptique et une autre ondulée. L'environnement Ansys-Fluent a été exploité pour l'analyse des champs d'écoulement tridimensionnels (3D) se tenant au sein des profils asymétriques, et le modèle de turbulence k-ω SST a été appliqué pour fermer le système nécessaire pour compenser l'effet de la couche limite. Les résultats numériques obtenus ont été comparés à ceux expérimentaux obtenus sur une tuyère elliptique analogue. Ils ont ensuite été comparés aux résultats obtenus sur la configuration axisymétrique originale à partir de laquelle les deux profils asymétriques elliptique et ondulé ont été générés.

L'accord obtenu entre les diverses composantes de l'étude crédite la méthode développée, prouvant qu'il est possible de concevoir des configurations asymétriques satisfaisantes.

Mots clés: tuyère asymétrique, Conception, Méthode des caractéristiques, Ecoulement supersonique, Dynamique des fluides computationnelle, Tuyère elliptique, Tuyère ondulée.

_____

PUBLICATIONS DURING CANDIDATURE

Peer-reviewed papers

Boughazi, N., Haddad, A., Kbab, H. (2022). Design approach and performance analysis of a truncated ideal contour propulsion nozzle. *U.P.B. Sci. Bull*., 84 (2), 167-184.

Dai, L., **Boughazi, N**., & Haddad, A. (2023). Design and Computational Analysis of an Axisymmetric Contoured Supersonic Propulsion Nozzle. *International Journal of Advanced Natural Sciences and Engineering Researches*, *7*(6), 244-249. https://doi.org/10.59287/ijanser.1160

Conference papers

Boughazi, N., & Haddad, A. (2020, July). A Simple Method for the Design of Supersonic Nozzles of Arbitrary Cross Section Shape. In *Fluids Engineering Division Summer Meeting* (Vol. 83723, p. V002T03A021). American Society of Mechanical Engineers. https://doi.org/10.1115/FEDSM2020-20197

Boughazi, N., Haddad, A. (2020, March 17-18). *A simple method for the design of supersonic nozzles of arbitrary cross-section shape*. In *Twelfth Conf. on Mechanical Engg-cme2020*, Bordj El-Bahri, Algiers, Algeria.

Boughazi, N., Haddad, A. (2021, May 02-04). *Design and cold flow simulation of a supersonic single bell nozzle*. In *Second Al Farabi International Congress on Applied Sciences*, Nakhchivan university, Azerbaijan.

Boughazi, N., Haddad, A. (2022, October, 25-26). *Conception et analyse de l'écoulement supersonique dans une tuyère convergente-divergente axisymétrique*. In *First Nat. Conf. on Thermal Engg*, University of Batna-2, Algeria.

Boughazi, N., Haddad, A., Kbab, H. (2022, March 15-16). *Design and CFD analysis of supersonic nozzles of elliptic cross-section shape*. In *Thirteenth Conf. on Mechanical Engg-cme2022*, Bordj El-Bahri, Algiers, Algeria.

Boughazi, N., Haddad, (2022, March 15-16). *Numerical study comparing k-ε and k-ω SST turbulence models with application to supersonic convergent-divergent nozzles*. In *First Nat. Conf. of Materials Sciences and Engineering-MSE'22*, Abbes Lagrour Khenchela University, Algeria.

Dai, L., **Boughazi, N**., Haddad, A. (2023, July, 04-05). *Simulation of the supersonic flowfield within the divergent section of a propulsion nozzle*. In *Seventh ICONTECH Conf. on Innovative surveys in positive sciences*, Ankara, Türkiye.

ACKNOWLEDGMENTS

_____

LIST OF CONTENTS

———————————————————————————

LIST OF FIGURES

_____

LIST OF TABLES

Coordinate system

In the two-dimensional computations (sections 3 and 4) involving the calculation of the flow-field within the axisymmetric nozzle, the system of coordinate is represented by:

x Axial coordinate direction,
y Radial coordinate direction,
u Axial component of the velocity,
v Radial component of the velocity.

When the three-dimensional computations are involved (sections 5 and 6), the system of coordinate is then represented by:

z Axial coordinate direction,
y Radial coordinate direction,
x Azimuthal coordinate direction,
w Axial component of the velocity,
v Radial component of the velocity,
u Azimuthal component of the velocity.

Latin notation:

a	Speed of sound or ellipse shape coefficients or Van der Waals equation constant
A	Area or Attachment point
A_w, B_w, C_w	2nd-order polynomial wall coefficient
b	Ellipse shape coefficient or Van der Waals equation constant
$c*$	Characteristic velocity
C_1, C_2, C_3, C_4	Sutherland's law gas constants
C_p	Specific heat at constant pressure
C_v	Specific heat at constant volume
C_T	Thrust coefficient
D	Diameter or characteristic dimension
D_ω	Cross-diffusion term in the transport equations (SST k-ω model
E_i	Internal energy per unit mass
E_p	Potential energy per unit mass
E_t	Total energy per unit mass
F	representative variable
G	representative variable or gravity acceleration
$\tilde{G}_k$	Generation of k due to mean velocity gradients (SST k-ω model)
G_ω	Generation of ω (SST k-ω model)
h	Enthalpy
I_{sp}	Specific impulse

k	Turbulent kinetic energy or conductibility coefficient
L	Dimensional characteristic or length
$\dot{m}$	Mass flow rate
M	Mach number
P	Pressure
Q, q	Heat or amount of heat
P_a	Ambient pressure or Pascal
P_t	Total (or stagnation) pressure
R_e	Reynolds number
R_G	Specific gas constant
R_{td}	Downstream throat radius of curvature
R_{tu}	Upstream throat radius of curvature
S	Entropy or surface or Modulus of the mean rate-of-strain tensor (sst k-ω model)
s	Entropy per unit volume
S_{ij}	Rate of strain tensor
S_k, S_ω	User-defined source terms (sst k-ω model)
t	Time
T	Temperature
T_t	Total (or stagnation) temperature
U	Internal energy
V	Velocity or volume
ϑ	Volume
W	Work
x_A, y_A	Attachment point axial and radial coordinates
x_E	Nozzle length
Y_k, Y_ω	Dissipation of k and ω due to turbulence (sst k-ω model)
y_E	Nozzle radius at exit
y_t	Throat radius

Greek notation:

α	Oblique shock angle or angle
α^*	Damping coefficient for the turbulent viscosity allowing a low Reynolds-number correction
β	Deflection angle of an oblique shock wave or angle
Γ_k	Effective diffusivity for turbulent kinetic energy k
Γ_ω	Effective diffusivity for specific turbulent dissipation rate ω
γ	Specific heat ratio ($\gamma = C_p/C_v$)
δ	Kronecker delta function (=0 if the flow is axisymmetric and =1 if it is planar).
δ^*	Boundary layer displacement thickness
θ	Angle
θ_A	Attachment angle
θ_E	Exit angle
λ	Correction factor in conical nozzles
μ	Dynamic viscosity
μ_1, μ_2	Mach angles

v	Kinematic viscosity
Π_{ij}	Stress tensor integrating both normal and shear stresses
ρ	Density
σ	Normal stress
σ_{ij}	Stress tensor
σ_k	Turbulent Prandtl number for k
σ_ω	Turbulent Prandtl number for ω
τ	Shear stress
Φ	Dissipation function
ω	Specific turbulent dissipation rate

Subscripts and superscripts:

$(\ )_a$	ambient state
$(\ )_e$	exit state
$(\ )_{eff}$	effective state
$(\ )_t$	total (or stagnation) state
$(\ )_w$	wall state
$(\ )^*$	critical state (choked nozzle)
$(\overline{\ })$	average value of property
$(\ )'$	fluctuation of property

Acronyms:

1-D	One-Dimensional
2-D	Two-Dimensional
3-D	Three-Dimensional
C-D	Convergent-Divergent
CFD	Computational Fluid Dynamics
E-D	Expansion-Deflection
FDM	Finite-Difference Method
FVM	Finite Volume Method
IC	Ideal Contour
MGP	Multi-Grid Profile
MNG	Multi-Nozzle Grid
MoC	Method of Characteristics
RANS	Reynolds-Averaged Navier-Stokes
SST	Shear Stress Transport
TIC	Truncated Ideal Contour
TOC	Thrust-Optimized Contour
TOP	Thrust-Optimized Parabolic
UAV	Unmanned Aerial Vehicle

Chapter1:
INTRODUCTION

1.1. General

The present work focuses on a simple and reliable procedure for the design of supersonic nozzles of arbitrary cross-sectional geometries that would make available a wide range of complex shapes whose design would be quite difficult even with three-dimensional computational approaches. It may also provide a method of solving some critical aerodynamic problems encountered in hypersonic flows as numerous aerospace applications need non-uniform or asymmetric nozzles that show altered geometries and therefore fit better to complex geometries leading to improved performance, maneuverability, or other specific characteristics.

1.2. Limitations of existing designs

Hypersonic air breathing vehicles have been the subject of great interest for the middle of the 20th century, and resurgence in interest has been recently perceived. A large spectrum of performances such as launch vehicle flexibility, emissions, and efficiency can be increased with the application of scramjet-powered hypersonic vehicles (McTaggart, 2022). Unfortunately, the drag penalty associated with the corrective trim increases and may achieve as much as 25% during engine operation (Preller, 2018; Ward, 2021). Asymmetric nozzles that can minimize drag and hence optimize thrust-minus-drag performances of such vehicles are required, as they permit achieving better airframe/propulsion system integration.

The streamline tracing approach (Haddad & Moss, 1990) has been applied and shown to produce good results, and the 3-D stream-traced approach has been showing considerable advancements recently (Kunze et al., 2022). However, such approaches may lead to extended operating and turnaround periods that would result in high costs that would be added to those engendered by the complexity of the design process that may range from the initial concept through the in-depth aero-thermodynamic simulation and performance evaluation. A simple and reliable method for the preliminary design of asymmetric supersonic nozzles of diverse cross sectional geometries is therefore needed.

1.3. Applications and scope

1.3.1. Applications

The asymmetry in the supersonic or hypersonic nozzles can take different forms such as variations in the divergent section shape, the primary purpose being the tailoring of the flow expansion and pressure distribution to achieve specific aerodynamic effects or performance benefits. These asymmetric profiles find applications in scenarios where conventional axisymmetric nozzles may not provide optimal performance, such as in supersonic and hypersonic vehicles,

including scramjets and spaceplanes, where asymmetric nozzles can optimize expansion and flow characteristics, therefore enhancing the engine performance in these extreme speed regimes along with achieving efficient propulsion at high speeds and altitudes. The asymmetry can also enhance maneuverability by providing thrust vectoring capabilities to aircrafts.

Asymmetric nozzles may also be found in Unmanned Aerial Vehicles (UAVs) where they can be employed for enhancing stability, control, and maneuverability, making them more effective for surveillance, reconnaissance, and other mission profiles. They can furthermore improve the efficiency and thrust of rocket engines used in launch vehicles, enhancing their payload capacity and reducing launch costs.

1.3.2. Scope

The present approach involves the development and investigation of a preliminary design method for determining theoretical profiles of supersonic nozzles of arbitrary cross-section shape from known axisymmetric flows. Its primary objective is the development of a procedure that leads to the production of complex asymmetric shapes and the production of vying designs of asymmetric supersonic nozzles based on axisymmetric primary computations. The original axisymmetric configuration profile is designed using the MoC. The asymmetric shape required is then defined at its exit cross-section and described by the necessary geometrical points which will be followed back to the throat to outline the asymmetric geometry needed.

Using this approach, two asymmetric nozzles were designed: an elliptical nozzle and a corrugated one. The validation of such an approach was performed through performing a 3-D simulation of the flow-field within the two asymmetric configurations using the "Ansys-Fluent" platform (Ansys, 2022). The results obtained were compared to the symmetric ones derived from the original axisymmetric configuration through the application of the MoC. Furthermore, the elliptic results were compared to the experimental results carried out on a similar elliptical nozzle (Haddad & Moss, 1990). The experimental results gathered from the literature and 3-D calculations carried out would show how the flow-field behaves in the asymmetric nozzles designed, while the MoC used to carry out the axisymmetric flow-field computations illustrates the overall performance of the initial axisymmetric configurations. Comparing the various aspects of such an investigation, in terms mainly of the pressure distributions, exit Mach and performance characteristics would show the method's propensity for producing relatively simply effective asymmetric nozzle designs.

The present thesis has been organized into seven sections. While the first exhibits the limitations of the existing designs represented mainly by the symmetric propulsion nozzles that have been used over the years along with the scope and applications of the asymmetric new configurations designed using the proposed procedure, the second section examines the literature that has been of benefit to the present research. This includes reviewing the principles that drive a compressible flow along with the equations that govern it and the turbulence models that close the system of equations. The MoC is presented as well as comprehensive review of the concept, importance and application of asymmetric nozzles.

The basis and implementation of the MoC along with its application to a 2-D inviscid flow-field are outlined in Section 3. The following chapter depicts the application of such method to the design of a Truncated Ideal Contour (TIC) nozzle.

Section 5 demonstrates how the proposed approach depicted earlier can be applied for the conversion of axisymmetric profile nozzles into asymmetric ones. The detailed procedure of the design of both the elliptic and corrugated nozzles is presented. The following section summarizes the results obtained from the three-dimensional simulation of both configurations along with the comparisons to the 2-D original design and the experimental validation pertaining to the elliptical nozzle.

The last section i.e. section 7 introduces the conclusions drawn along with some recommendations that may be useful for further work.

_____

Chapter2:

LITERATURE REVIEW

2.1. General

This chapter covers a review of the research on propulsion nozzles with a focus on three specific areas. The first deals with the compressible flow that takes place within a nozzle along with equations that describe it. The flow-field being turbulent, the turbulence phenomenon is introduced with the most applied models needed to close the system of equations. The isentropic flow simplifications are presented. They are followed by a review of the early and more recent designs in terms of rocket propulsion nozzles along with their characteristic performance parameters. The MoC needed for the design of such nozzles is presented and illustrated in detail.

There has recently been a lot of interest in incorporating asymmetric nozzles into supersonic and hypersonic air breathing vehicles. This would enhance their performance and provide numerous advantages such as thrust efficiency, maneuverability and control. Recent research and results achieved are summarized.

2.2. Compressible flows and the universal conservation equations

Flow-fields are represented by the movement of fluids and may be classified in various ways. A flow can be steady or unsteady given the dependence on time or not. It also can be inviscid or viscous depending on the fact that the friction effects, represented by viscosity, can be neglected or must be taken into account. A flow-field can furthermore be laminar or turbulent. In laminar flows, the streamlines tend to slide past each other while remaining parallel. Disorder and intensive particle mixing indicates a turbulent flow. This property is determined using the dimensionless Reynolds number:

$$\mathrm{Re} = \frac{\rho V D}{\mu} = \frac{V D}{\nu} \tag{2.1}$$

2.2.1. Compressible flows

Compressible flows play a key role in a wide variety of natural as well as artificial phenomena (the generation of various atmospheric events and the different sounds we hear are natural phenomena whereas the vehicles we drive and the systems we build to generate energy are artificial ones). All depend, in one way or another, on the mechanics and thermodynamics of compressible flows (Benhamouda, 2008).

The compressibility inherent to a real fluid cannot be neglected for high flow velocities. The compressibility criterion is therefore represented by the Mach number defined as the ratio of the flow velocity to that of the sound under the same pressure and temperature conditions:

$$M = \frac{V}{a} \tag{2.2}$$

If: $M \leq 0,3$, the variations in the density are small enough to consider the flow as incompressible.

$M \succ 0,3$, the variations in density can no longer be neglected, and the flow has to be considered compressible.

In the case of compressible flows, variations in density will necessarily lead to significant fluctuations in pressure and temperature. The equations governing such a flow will therefore be represented by the equation of conservation of mass (or continuity equation), the equation of conservation of momentum (that may be developed as what is known as the Navier-Stokes equations), the equation of conservation of energy reflecting the first law of thermodynamics, and the equation of state. These equations will have to be solved simultaneously in terms of the unknowns represented by flow velocity, pressure, temperature, density, and temperature.

In most elementary conditions, studies may be limited to the case of ideal gases whose specific heats as well as their ratio are considered constant and are expressed as:

$$\gamma = \frac{C_p}{C_v} \tag{2.3}$$

$$R = C_p - C_v \tag{2.4}$$

For all real gases, (C_p) and (C_v) vary only slightly with temperature (The specific heat at constant pressure i.e. *Cp* of air increases by 30% when the temperature increases from -18°C to 2760°C) while variations in their ratio (γ) have only a slight effect on the results of calculations inherent to compressible flows where air is most used.

2.2.2. Universal conservation equations

2.2.2.1. Mass conservation or continuity equation

A mass cannot be created nor destroyed. It may only be transformed. It is on this basic principle of 'conservation of mass' that the first universal law has been founded. It has been developed by considering a volume element whose surface is fixed in space (the Eulerian control volume) through which flows a fluid of density (ρ) whose velocity components are denoted (*u*, *v* and *w*) relative to a Cartesian coordinate system (*x*, *y* and *z*). Within such an unsteady and compressible flow, all variables depend on both position and time (*t*). In this case, the principle of conservation of mass or continuity may be stated as:

$$\left\langle \begin{array}{c} \text{mass accumulation rate} \\ \text{within the control volume} \end{array} \right\rangle = \left\langle \begin{array}{c} \text{Mass flow rate entering} \\ \text{the control volume} \end{array} \right\rangle - \left\langle \begin{array}{c} \text{Mass flow rate leaving} \\ \text{the control volume} \end{array} \right\rangle$$

which, in differential form, may be written as:

$$\frac{\partial \rho}{\partial t} + \nabla \cdot \left(\rho \vec{V} \right) = 0 \tag{2.5}$$

$$\frac{\partial \rho}{\partial t} + \frac{\partial}{\partial x}(\rho u) + \frac{\partial}{\partial x}(\rho v) + \frac{\partial}{\partial x}(\rho w) = 0 \tag{2.6}$$

2.2.2.2. Momentum conservation equation

Newton's three main laws of motion were stated in his work 'Philosophiae naturalis principia mathematica' originally published in Latin in 1687 (Newton, 1687; Gabbey, 1976). They constitute the fundamental principles of Newton's theory concerning the movement of bodies commonly known as 'Newtonian mechanics' or more simply 'classical mechanics'.

Newton's second law known as the 'fundamental relation of dynamics' or simply 'equation of motion' states that:

$$\left\langle \begin{matrix} \text{Rate of change} \\ \text{of momentum} \end{matrix} \right\rangle = \left\langle \begin{matrix} \text{Sum of the forces acting} \\ \text{on the external element} \end{matrix} \right\rangle$$

That, for a constant mass, may be expressed as:

$$\frac{d\left(m\vec{V}\right)}{dt} = \sum \vec{F} \tag{2.7}$$

In the case of flowing fluids, the external forces are exerted either through the mass of the element considered (mass or gravitational forces) or through its surface (pressure and friction forces). By considering a volume element ($\Delta \vartheta = dxdydz$), expressing these forces and arranging, it comes (Anderson et al., 2020):

$$\frac{\partial}{\partial t}\left(\rho\vec{V}\right) + \vec{\nabla} \cdot \rho\vec{V}\vec{V} = \rho\vec{g} + \vec{\nabla} \cdot \prod_{ij} \tag{2.8}$$

Using the stress tensor, the previous equation can be written as:

$$\begin{cases} \dfrac{\partial \rho u}{\partial t} + \dfrac{\partial}{\partial x}\left(\rho u^2 + p - \sigma_{xx}\right) + \dfrac{\partial}{\partial y}\left(\rho uv - \sigma_{xy}\right) + \dfrac{\partial}{\partial z}\left(\rho uw - \sigma_{xz}\right) = \rho g_x \\[2mm] \dfrac{\partial \rho v}{\partial t} + \dfrac{\partial}{\partial x}\left(\rho uv - \sigma_{xy}\right) + \dfrac{\partial}{\partial y}\left(\rho v^2 + p - \sigma_{yy}\right) + \dfrac{\partial}{\partial z}\left(\rho uw - \sigma_{yz}\right) = \rho g_y \\[2mm] \dfrac{\partial \rho w}{\partial t} + \dfrac{\partial}{\partial x}\left(\rho uw - \sigma_{xz}\right) + \dfrac{\partial}{\partial y}\left(\rho uw - \sigma_{yz}\right) + \dfrac{\partial}{\partial z}\left(\rho w^2 + p - \sigma_{zz}\right) = \rho g_z \end{cases} \tag{2.9}$$

Equation 2.9 is the general momentum equation applicable for any fluid in motion. To specify a particular fluid requires the viscosity stresses to be expressed as a function of the velocity components. In the case of a Newtonian fluid, they have been found to be proportional to the strain rate and the viscosity coefficient (Anderson et al., 2020):

$$\begin{cases} \sigma_{xx} = \dfrac{2}{3}\mu\left(2\dfrac{\partial u}{\partial x} - \dfrac{\partial v}{\partial y} - \dfrac{\partial w}{\partial z}\right) \quad ; \quad \sigma_{yy} = \dfrac{2}{3}\mu\left(2\dfrac{\partial v}{\partial y} - \dfrac{\partial u}{\partial x} - \dfrac{\partial w}{\partial z}\right) \\[3mm] \sigma_{zz} = \dfrac{2}{3}\mu\left(2\dfrac{\partial w}{\partial z} - \dfrac{\partial u}{\partial x} - \dfrac{\partial v}{\partial y}\right) \end{cases} \tag{2.10}$$

$$\begin{cases} \sigma_{xy} = \sigma_{yx} = \mu\left(\dfrac{\partial u}{\partial y} + \dfrac{\partial v}{\partial x}\right) \quad ; \quad \sigma_{xz} = \sigma_{zx} = \mu\left(\dfrac{\partial w}{\partial x} + \dfrac{\partial v}{\partial z}\right) \\[3mm] \sigma_{yz} = \sigma_{zy} = \mu\left(\dfrac{\partial v}{\partial z} + \dfrac{\partial w}{\partial y}\right) \end{cases} \tag{2.11}$$

Replacing the expressions of the viscosity stresses (Equations 2.10 and 2.11) in the general equation of motion 2.9 leads to express the well-known Navier-Stokes equations named after both the French Engineer Claude Louis Navier (Navier, 1821; Navier, 1827) and British George Gabriel Stokes (Stokes, 1880):

$$
\begin{cases}
\rho\left(\dfrac{\partial u}{\partial t}+u\dfrac{\partial u}{\partial x}+v\dfrac{\partial u}{\partial y}+w\dfrac{\partial u}{\partial z}\right)=\rho g_x-\dfrac{\partial p}{\partial x}+\dfrac{\partial}{\partial x}\left[\dfrac{2}{3}\mu\left(2\dfrac{\partial u}{\partial x}-\dfrac{\partial v}{\partial y}-\dfrac{\partial w}{\partial z}\right)\right]\\
\qquad\qquad\qquad\qquad\qquad +\dfrac{\partial}{\partial y}\left[\mu\left(\dfrac{\partial v}{\partial x}+\dfrac{\partial u}{\partial y}\right)\right]+\dfrac{\partial}{\partial z}\left[\mu\left(\dfrac{\partial u}{\partial z}+\dfrac{\partial w}{\partial x}\right)\right]\\
\rho\left(\dfrac{\partial v}{\partial t}+u\dfrac{\partial v}{\partial x}+v\dfrac{\partial v}{\partial y}+w\dfrac{\partial v}{\partial z}\right)=\rho g_y-\dfrac{\partial p}{\partial y}+\dfrac{\partial}{\partial x}\left[\mu\left(\dfrac{\partial v}{\partial x}+\dfrac{\partial u}{\partial y}\right)\right]\\
\qquad\qquad\qquad\qquad\qquad +\dfrac{\partial}{\partial y}\left[\dfrac{2}{3}\mu\left(2\dfrac{\partial v}{\partial y}-\dfrac{\partial u}{\partial x}-\dfrac{\partial w}{\partial z}\right)\right]+\dfrac{\partial}{\partial z}\left[\mu\left(\dfrac{\partial w}{\partial y}+\dfrac{\partial v}{\partial z}\right)\right]\\
\rho\left(\dfrac{\partial w}{\partial t}+u\dfrac{\partial w}{\partial x}+v\dfrac{\partial w}{\partial y}+w\dfrac{\partial w}{\partial z}\right)=\rho g_z-\dfrac{\partial p}{\partial z}+\dfrac{\partial}{\partial x}\left[\mu\left(\dfrac{\partial u}{\partial z}+\dfrac{\partial w}{\partial x}\right)\right]\\
\qquad\qquad\qquad\qquad\qquad +\dfrac{\partial}{\partial y}\left[\mu\left(\dfrac{\partial w}{\partial y}+\dfrac{\partial v}{\partial z}\right)\right]+\dfrac{\partial}{\partial z}\left[\dfrac{2}{3}\mu\left(2\dfrac{\partial w}{\partial z}-\dfrac{\partial u}{\partial x}-\dfrac{\partial v}{\partial y}\right)\right]
\end{cases}
\tag{2.12}
$$

2.2.2.3. Conservation of energy equation

When there is a flow of fluid and if the system is not considered adiabatic, it is accompanied by a flow of heat. Determining the temperature distribution requires combining the application of the equations of motion along with that describing the conservation of energy based on the first law of thermodynamics. Applied to a fluid flowing through a fixed infinitesimal volume, the first law of thermodynamics allows the energy conservation equation to be expressed in the form (Anderson et al., 2020):

$$
\frac{\partial E_t}{\partial t}+\nabla\cdot E_t V=\frac{\partial Q}{\partial t}-\nabla\cdot q+p\mathrm{f}\cdot V+\nabla\cdot\left(\prod_{ij}\cdot V\right)
\tag{2.13}
$$

where: - the total energy per unit mass (E_t) and the internal energy per unit mass (E_i) are related through the relationship:

$$
E_t=\rho\left(E_i+E_c+E_p\right)=\rho\left(E_i+\frac{V^2}{2}+E_p\right)
\tag{2.14}
$$

- $\dfrac{\partial E_t}{\partial t}$:   Rate of increase in total energy (E_t),

- $\nabla\cdot E_t V$:   Rate of total energy (E_t) lost by convection per unit volume through the control surface.

- $\dfrac{\partial Q}{\partial t}$:   Rate of heat produced per unit volume by external sources.

- $\nabla\cdot q$:   Rate of heat lost by conduction per unit volume through the control surface.

- $p\mathrm{f}\cdot V$:   Work performed by volume forces per unit volume.

- $\nabla\cdot\left(\prod_{ij}\cdot V\right)$:   Work done by surface forces per unit volume.

Expressed in terms of the Cartesian coordinates, the energy equation 2.13 is written as:

$$\frac{\partial E_t}{\partial t} - \frac{\partial Q}{\partial t} - \rho\left(f_x u + f_y v + f_z w\right) + \frac{\partial}{\partial x}\left(E_t u + pu - u\sigma_{xx} - v\sigma_{xy} - w\sigma_{xz} + q_x\right)$$
$$+ \frac{\partial}{\partial y}\left(E_t v + pv - u\sigma_{xy} - v\sigma_{yy} - w\sigma_{yz} + q_y\right) \tag{2.15}$$
$$+ \frac{\partial}{\partial z}\left(E_t w + pw - u\sigma_{xz} - v\sigma_{yz} - w\sigma_{zz} + q_z\right) = 0$$

Applying the continuity equation, considering the internal and kinetic energies as the sole significant to be taken into account and replacing the viscosity stresses by their expressions represented by equation 2.10 and equation 2.11, equation 2.13, for a Newtonian fluid, becomes:

$$\rho\frac{dE_i}{dt} + p\left(\nabla \cdot V\right) = \frac{dQ}{dt} - \nabla \cdot q + \Phi \tag{2.16}$$

where: - $\dfrac{d}{dt} = \dfrac{\partial}{\partial t} + V \cdot \nabla = \dfrac{\partial}{\partial t} + u\dfrac{\partial}{\partial x} + v\dfrac{\partial}{\partial y} + w\dfrac{\partial}{\partial z}$ is the material derivative.

   - the dissipation function (Φ) expresses the rate at which the mechanical energy is lost in the process of deformation of the fluid due to strain rate:

$$\Phi = \mu\left[2\left(\frac{\partial u}{\partial x}\right)^2 + 2\left(\frac{\partial v}{\partial y}\right)^2 + 2\left(\frac{\partial w}{\partial z}\right)^2 + \left(\frac{\partial v}{\partial x} + \frac{\partial u}{\partial y}\right)^2 + \left(\frac{\partial w}{\partial y} + \frac{\partial v}{\partial z}\right)^2\right.$$
$$\left. + \left(\frac{\partial u}{\partial z} + \frac{\partial w}{\partial x}\right)^2 - \frac{2}{3}\left(\frac{\partial u}{\partial x} + \frac{\partial v}{\partial y} + \frac{\partial w}{\partial z}\right)^2\right] \tag{2.17}$$

The complexity of equation 2.16 only allows its integration numerically. It is generally customary to undertake approximations in order to achieve an analytical solution (Schlichting & Gersten, 2016). In the case of an incompressible fluid and considering the conductivity coefficient (k) as constant, equation 2.16 may be simplified to become:

$$\rho\frac{dE_i}{dt} = \frac{dQ}{dt} + k\nabla^2 T + \Phi \tag{2.18}$$

2.2.2.4. Equation of state

The conservation equations expressed in the previous sections contain seven unknowns represented by the three components of the velocity (u, v and w), the pressure (p), the density (ρ), the internal energy (E_i) and the temperature (T). The transport coefficients (μ and k) being linked to the thermodynamic properties through the Sutherland's law (equation 2.25), they are subsequently not included among the unknowns. It is therefore imperative that two additional equations be developed to close the system. They are generally obtained by deriving the relationships linking the various thermodynamic parameters and are called equations of state 2.19. In the present case where

the internal energy and the density are chosen as independent variables, these equations are expressed as:

$$p = f\left(E_i, \rho\right) \quad ; \quad T = f\left(E_i, \rho\right)$$ (2.19)

The first relationship, widely applied in the case of gas flows, is that assuming the gas to be perfect, i.e. a gas whose intermolecular forces are negligible. It is expressed as:

$$p = \rho R T$$ (2.20)

For gases flowing under high pressure or low temperature, the intermolecular forces become important. In this case, the equation of state represented by the ideal gas law 2.20 can no longer be applied. An equation such as that of Van der Waals (Van der Waals, 1910; Silbey et al., 2021) could be used:

$$\left(p + a\rho^2\right)\left(\frac{1}{\rho} - b\right) = RT$$ (2.21)

Another case is that represented by the assumption of a calorically perfect gas i.e. whose specific heats at constant pressure (C_p) and volume (C_v) are considered as constants:

$$C_v = \frac{R}{\gamma - 1} = \text{constante} \quad ; \quad C_p = \frac{\gamma R}{\gamma - 1} = \text{constante}$$ (2.22)

where: $E_i = C_v T \quad ; \quad h = C_p T \quad ; \quad \gamma = \dfrac{C_p}{C_v}$ (2.23)

In the case of a calorically ideal gas, equations 2.19 become:

$$p = \left(\gamma - 1\right)\rho E_i \qquad \text{and} \qquad k = C_3 \frac{T^{\frac{3}{2}}}{T + C_4}$$ (2.24)

The dynamic viscosity (μ) and thermal conductivity (k) can also be linked using Sutherland's law (Sutherland, 1893; Hirschfelder et al., 1964):

$$\mu = C_1 \frac{T^{\frac{3}{2}}}{T + C_2} \qquad \text{and} \qquad k = C_3 \frac{T^{\frac{3}{2}}}{T + C_4}$$ (2.25)

Where: (C_1, C_2, C_3 and C_4) are constants specific to each gas.

2.3. The turbulence

Turbulence is used to refer to many physical phenomena characterized by disorder and complexity. It is moreover a fact that most real flows are turbulent. Laminar flows are those where viscosity predominates. They are regular and predictable. On the other hand, turbulent flows appear

when the source of kinetic energy that drives the moving fluid is so intense that it overcomes the effects of viscosity that tend to slow the flow down.

2.3.1. Laminar and turbulent flow – Reynolds number

In 1883, Osborne Reynolds (Reynolds, 1883; Reynolds, 1895) highlighted the transition between laminar and turbulent flows by injecting dye on the centerline of a pipe like the one illustrated in figure 2.1. In the laminar regime, the dye will form a straight line that does not mix with the surrounding fluid (except by molecular diffusion). Above a certain velocity, the sequence becomes unstable and the dye quickly disperses through the whole pipe: it is the turbulent regime which is in fact effective for the mixing of fluids.
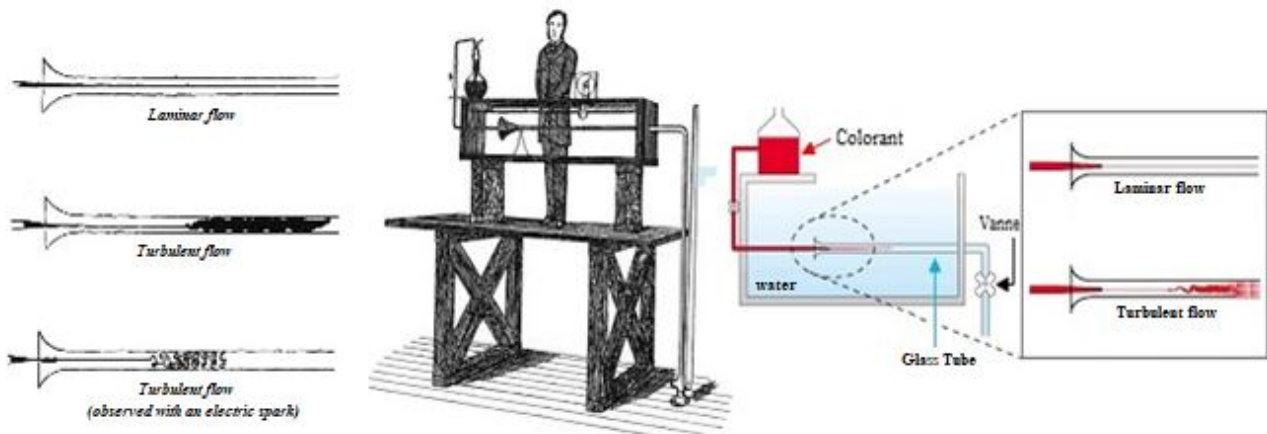
Figure 2.1: Experimental setup of Reynolds' experiment
(The Science Museum, founded 1857, Exhibition Road, South Kensington, London)

Reynolds applied dimensional analysis to pipe flows and concluded that the transition takes place for a fixed value of a certain parameter that can be interpreted as the ratio of the forces of inertia to those of viscosity. In his honor, this parameter has since been called: the Reynolds number and is expressed as:

$$\text{Re} = \frac{\text{Inertial Forces}}{\text{Viscosity Forces}} = \frac{\text{mass} \times \text{acceleration}}{\text{hear stress} \times \text{area}} = \frac{\rho V^2 L^2}{\mu V L}$$

$$\text{Re} = = \frac{\rho V L}{\mu} = \frac{V L}{v} \tag{2.26}$$

2.3.2. Mean (Reynolds) Navier-Stokes equations

A turbulent flow is a movement in which irregular fluctuations are superimposed on a main flow, and all turbulence modeling schemes require some 'breakdown' of the dependent variables. Figure 2.2 illustrates the Reynolds decomposition of the axial component of the velocity.
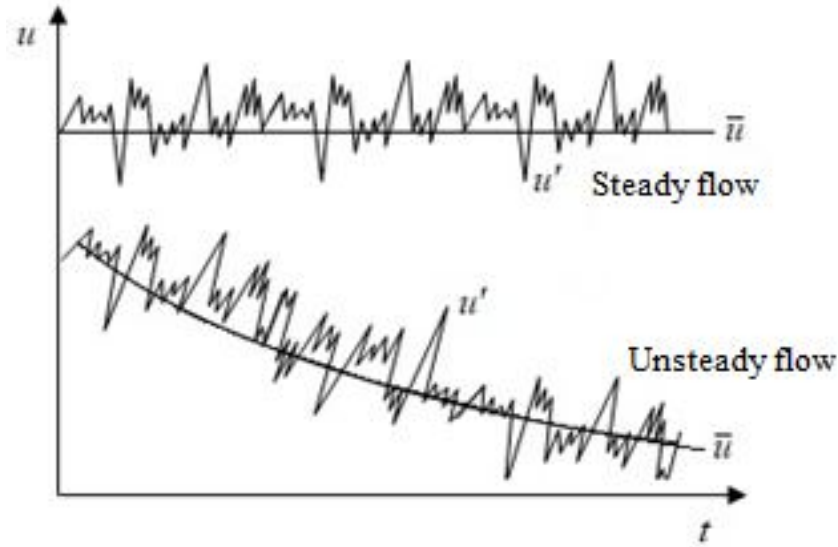
Figure 2.2: Reynolds decomposition involving the axial component of the velocity of steady and unsteady flows

A turbulent flow can therefore be described by the superposition of an average flow added to fluctuations. It is therefore appropriate to decompose the instantaneous variables (e.g. components of velocity and pressure) into an average value and a fluctuating one, i.e.:

$$\begin{cases} u_i = \bar{u}_i + u_i' \\ \bar{\bar{u}}_i = \bar{u}_i \\ \overline{u_i'} = 0 \end{cases} \qquad \begin{cases} p = \bar{p} + p' \\ \bar{\bar{p}} = \bar{p} \\ \overline{p'} = 0 \end{cases} \tag{2.27}$$

One of the reasons why variables are decomposed this way is represented by the fact that when they are measured, it is generally their average values rather than the history of their fluctuations that will be taken into account. Another important reason relates to the problem of numerical resolution of the Navier-Stokes equations that would require an extremely refined mesh in order to be able to take into account the levels of the turbulent scales. It would also require fine resolution over time, as turbulent flows are generally unsteady.

If the flow is compressible with heat transfer, fluctuation terms of both density and temperature are added. Thus:

$$\begin{cases} \rho = \bar{\rho} + \rho' \\ \bar{\bar{\rho}} = \bar{\rho} \\ \overline{\rho'} = 0 \end{cases} \qquad \begin{cases} T = \bar{T} + T' \\ \bar{\bar{T}} = \bar{T} \\ \overline{T'} = 0 \end{cases} \tag{2.28}$$

It is clear that for such representative variables denoted (*f*) and (*g*), the operations involving average values and fluctuations will result in:

$$\begin{cases} \bar{\bar{f}} = \bar{f} \;\; ; \;\; \overline{f+g} = \bar{f} + \bar{g} \;\; ; \;\; \overline{\bar{f} \cdot g} = \bar{f} \cdot \bar{g} \;\; ; \;\; \overline{\bar{f}g'} = 0 \;\; ; \;\; \overline{\bar{f}\bar{g}} = \bar{f}\bar{g} \\ \overline{\alpha f} = \alpha \bar{f} \; (\alpha \text{ constante}) \;\; ; \;\; \overline{\dfrac{\partial f}{\partial x_i}} = \dfrac{\partial \bar{f}}{\partial x_i} \;\; ; \;\; \overline{\dfrac{\partial f}{\partial t}} = \dfrac{\partial \bar{f}}{\partial t} \;\; ; \;\; \overline{\int f ds} = \int \bar{f} ds \end{cases} \tag{2.29}$$

2.3.2.1. Mass conservation equation – Reynolds form

By replacing the variables of the equation for the conservation of mass expressed in Cartesian coordinates in (equation 2.30) by the sum of their average values and fluctuations, and by simplifying (equations 2.27 and 2.28), the Reynolds form of this equation is written as:

$$\frac{\partial \rho}{\partial t} + \frac{\partial}{\partial x}(\rho u) + \frac{\partial}{\partial x}(\rho v) + \frac{\partial}{\partial x}(\rho w) = 0 \tag{2.6}$$

$$\frac{\partial \overline{\rho}}{\partial t} + \frac{\partial \overline{\rho}'}{\partial t} + \frac{\partial}{\partial x_j}\left(\overline{\overline{\rho}\,\overline{u}_j}\right) + \frac{\partial}{\partial x_j}\left(\overline{\rho'\overline{u}_j}\right) + \frac{\partial}{\partial x_j}\left(\overline{\overline{\rho}\,u_j'}\right) + \frac{\partial}{\partial x_j}\left(\overline{\rho'u_j'}\right) = 0$$

$$\frac{\partial \overline{\rho}}{\partial t} + \frac{\partial}{\partial x_j}\left(\overline{\rho}\,\overline{u}_j\right) = 0 \tag{2.30}$$

2.3.2.2. Navier-Stokes equations - Reynolds form

The average relative to time of the momentum conservation equations (equation 2.7) are obtained in the same way as the continuity equation i.e. by replacing the variables by the sum of their average values and fluctuations (equations 2.27 and 2.28) and simplifying. In the axial direction (i.e. x), it comes:

$$\frac{\partial}{\partial t}\Big[\big(\overline{\rho}+\rho'\big)\big(\overline{u}+u'\big)\Big] + \frac{\partial}{\partial x}\Big[\big(\overline{\rho}+\rho'\big)\big(\overline{u}+u'\big)\big(\overline{u}+u'\big)\big(\overline{p}+p'\big)-\sigma_{xx}\Big]$$
$$+\frac{\partial}{\partial y}\Big[\big(\overline{\rho}+\rho'\big)\big(\overline{u}+u'\big)\big(\overline{v}+v'\big)-\sigma_{yx}\Big] \tag{2.31}$$
$$+\frac{\partial}{\partial z}\Big[\big(\overline{\rho}+\rho'\big)\big(\overline{u}+u'\big)\big(\overline{w}+w'\big)-\sigma_{zx}\Big]=0$$

Taking the time average of the whole equation, the linear parts in terms of fluctuations become null. Eliminating them and applying the continuity equation to regroup the remaining ones, the axial component of the conservation of momentum equation may then be written as:

$$\frac{\partial}{\partial t}\left(\overline{\rho}\,\overline{u}+\overline{\rho'u'}\right) + \frac{\partial}{\partial x}\left(\overline{\rho}\,\overline{uu}+\overline{u}\,\overline{\rho'u'}\right)$$
$$+\frac{\partial}{\partial y}\left(\overline{\rho}\,\overline{uv}+\overline{u}\,\overline{\rho'v'}\right) + \frac{\partial}{\partial z}\left(\overline{\rho}\,\overline{uw}+\overline{u}\,\overline{\rho'w'}\right)$$
$$=-\frac{\partial \overline{p}}{\partial x} + \frac{\partial}{\partial x}\left[\mu\left(2\frac{\partial \overline{u}}{\partial x}-\frac{2}{3}\frac{\partial \overline{u}_k}{\partial x_k}\right)-\overline{u}\,\overline{\rho'u'}-\overline{\rho}\,\overline{u'u'}-\overline{\rho'u'u'}\right] \tag{2.32}$$
$$+\frac{\partial}{\partial y}\left[\mu\left(\frac{\partial \overline{u}}{\partial y}+\frac{\partial \overline{v}}{\partial x}\right)-\overline{v}\,\overline{\rho'u'}-\overline{\rho}\,\overline{u'v'}-\overline{\rho'u'v'}\right]$$
$$+\frac{\partial}{\partial z}\left[\mu\left(\frac{\partial \overline{u}}{\partial z}+\frac{\partial \overline{w}}{\partial x}\right)-\overline{w}\,\overline{\rho'u'}-\overline{\rho}\,\overline{u'w'}-\overline{\rho'u'w'}\right]$$

The same procedure can be applied for the other two components of the momentum conservation equation. In turbulent flow, the Navier-Stokes equations may finally be expressed as:

$$\frac{\partial}{\partial t}\left(\overline{\rho}\overline{u}_i + \overline{\rho' u'_i}\right) + \frac{\partial}{\partial x_j}\left(\overline{\rho}\overline{u}_i\overline{u}_j + \overline{u}_i\overline{\rho' u'_j}\right)$$
$$= -\frac{\partial \overline{p}}{\partial x_i} + \frac{\partial}{\partial x_j}\left(\overline{\sigma}_{ij} - \overline{u}_j\overline{\rho' u'_i} - \overline{\rho}\overline{u'_i u'_j} - \overline{\rho' u'_i u'_j}\right) \tag{2.33}$$

with: $\overline{\sigma}_{ij} = \mu\left[\left(\frac{\partial \overline{u}_i}{\partial x_j} + \frac{\partial \overline{u}_j}{\partial x_i}\right) - \frac{2}{3}\delta_{ij}\frac{\partial \overline{u}_k}{\partial x_k}\right]$ \tag{2.34}

and: $\delta_{ij} = \begin{cases} 1 & \text{si } i = j \\ 0 & \text{si } i \neq j \end{cases}$ represents the Kronecker symbol (Kronecker, 1968)

In the case of an incompressible flow, equation 2.33 may be simplified to become:

$$\frac{\partial}{\partial t}\left(\rho\overline{u}_i\right) + \frac{\partial}{\partial x_j}\left(\rho\overline{u}_i\overline{u}_j\right) = -\frac{\partial \overline{p}}{\partial x_i} + \frac{\partial}{\partial x_j}\left[\overline{\sigma}_{ij} - \rho\overline{u'_i u'_j}\right] \tag{2.35}$$

with: $\overline{\sigma}_{ij} = \mu\left(\frac{\partial \overline{u}_i}{\partial x_j} + \frac{\partial \overline{u}_j}{\partial x_i}\right)$ \tag{2.36}

2.3.2.3. Energy conservation equation - Reynolds form

The energy conservation equation can take various forms, depending on the parameter chosen to be the thermal variable transported. It is often desirable to use the temperature as the transport variable. The Reynolds average form of the energy equation is obtained in the same way both the conservation of mass and momentum equations have been derived previously. The dependent variables in equation 2.13 are replaced by the sum of the average and fluctuations of equations 2.27 and 2.28. After time averaging, the equation becomes:

$$\frac{\partial}{\partial t}\left(C_p\overline{\rho}\overline{T} + C_p\overline{\rho' T'}\right) + \frac{\partial}{\partial x_j}\left(\overline{\rho}C_p\overline{T}\overline{u}_j + C_p\overline{T}\overline{u}_i\overline{\rho' u'_j}\right)$$
$$= \frac{\partial \overline{p}}{\partial t} + \overline{u}_j\frac{\partial \overline{p}}{\partial x_j} + \overline{u'_j\frac{\partial p'}{\partial x_j}}$$
$$+ \frac{\partial}{\partial x_j}\left(k\frac{\partial \overline{T}}{\partial x_j} - \overline{\rho}C_p\overline{T' u'_j} - C_p\overline{\rho' T' u'} - \overline{u}_jC_p\overline{\rho' T'}\right) + \Phi \tag{2.37}$$

where: $\overline{\Phi} = \overline{\sigma_{ij}\frac{\partial u_i}{\partial x_j}} = \overline{\sigma}_{ij}\frac{\partial \overline{u}_i}{\partial x_j} + \overline{\sigma'_{ij}\frac{\partial u'_i}{\partial x_j}}$ \tag{2.38}

and: $\overline{\sigma}_{ij} = \mu\left[\left(\frac{\partial \overline{u}_i}{\partial x_j} + \frac{\partial \overline{u}_j}{\partial x_i}\right) - \frac{2}{3}\delta_{ij}\frac{\partial \overline{u}_k}{\partial x_k}\right]$ \tag{2.39}

2.3.3. Equations and Reynolds stresses

The Reynolds forms of the conservation equations 2.30, 2.33 and 2.37 derived previously and often referred to as RANS equations are likely to be quite complex. Nevertheless and for many cases, they can be simplified.

The mean equations of motion relate the acceleration of the flowing fluid to the stress gradients. Knowing how the acceleration for the mean flow-field is expressed, it would therefore be appropriate to consider any new term as a stress gradient due to turbulence.

The incompressible momentum (equation 2.40) can be rewritten in another form by applying the continuity equation and highlighting the particle derivative. The following equation is obtained:

$$\frac{\partial}{\partial t}\left(\rho \bar{u}_i\right) + \frac{\partial}{\partial x_j}\left(\rho \bar{u}_i \bar{u}_j\right) = -\frac{\partial \bar{p}}{\partial x_i} + \frac{\partial}{\partial x_j}\left[\bar{\sigma}_{ij} - \rho \overline{u_i' u_j'}\right] \tag{2.40}$$

$$\left\{\rho \frac{\partial \bar{u}_i}{\partial t} + \frac{\partial}{\partial x_j}\left(\rho \bar{u}_i \bar{u}_j\right)\right\} = \left\{-\frac{\partial \bar{p}}{\partial x_i}\right\} + \left\{\frac{\partial \bar{\sigma}_{ij}}{\partial x_j}\right\} + \left\{\frac{\partial\left(-\rho \overline{u_i' u_j'}\right)}{\partial x_j}\right\}$$

which can expressed as:

$$\underbrace{\rho \frac{d\bar{u}_i}{dt}}_{\substack{\text{Acceleration of}\\\text{mean flow}}} = \underbrace{-\frac{\partial \bar{p}}{\partial x_i}}_{\substack{\text{Aerage pressure}\\\text{gradient}}} + \underbrace{\frac{\partial\left(\bar{\sigma}_{ij}\right)_{\text{laminaire}}}{\partial x_j}}_{\substack{\text{laminar stress gradients}\\\text{of the mean flow}}} + \underbrace{\frac{\partial\left(\bar{\sigma}_{ij}\right)_{\text{turbulent}}}{\partial x_j}}_{\substack{\text{stress gradients apparently due to}\\\text{turbulent fluctuations dynamics}}} \tag{2.41}$$

leading to: $\left(\bar{\sigma}_{ij}\right)_{\text{turbulent}} = -\rho \overline{u_i' u_j'}$ (2.42)

These additional stresses are commonly known as 'Reynolds stresses', and they represent a symmetrical tensor of 2$^{\text{nd}}$ order. A similar development of the Reynolds equations of motion and energy for compressible flows will identify the terms involving the fluctuations involving both the velocity and temperature i.e. the gradients of the stresses and heat flux:

$$\left(\bar{\sigma}_{ij}\right)_{\text{turb.}} = \overline{-\rho u_i' u_j'} + \mu\left[\left(\frac{\partial \bar{u}_i'}{\partial x_j} + \frac{\partial \bar{u}_j'}{\partial x_i}\right) - \frac{2}{3}\delta_{ij}\frac{\partial \bar{u}_k'}{\partial x_k}\right] \tag{2.43}$$

$$-\left(\nabla \cdot q\right)_{\text{turb.}} = \frac{\partial}{\partial x_j}\left(-\bar{\rho}C_p \overline{T' u_j'} - C_p \overline{\rho' T' u_j'} - \bar{u}_j C_p \overline{\rho' T'}\right) \tag{2.44}$$

The Reynolds' turbulent conservation equations cannot be solved in their current forms, as the new turbulent stresses and turbulent heat-flow that have been introduced are unknowns.

The solution resides either in the derivation of new equations involving these turbulent new terms, or the addition of relationships linking them to the time-averaged variables developed. This closure problem is often solved through 'turbulence modeling'.

2.3.4. The closure problem – modelling and turbulence models

Any turbulence model should be validated. Its predictions should therefore be verified and compared with the corresponding experimental results. This is a limitation as it requires the user to apply it only within the range of conditions for which it has been validated. Three main classes of turbulence models are generally distinguished. They are represented in Figure 2.3 taking into account their computational cost, degrees of freedom, geometric complexity and modeling importance.
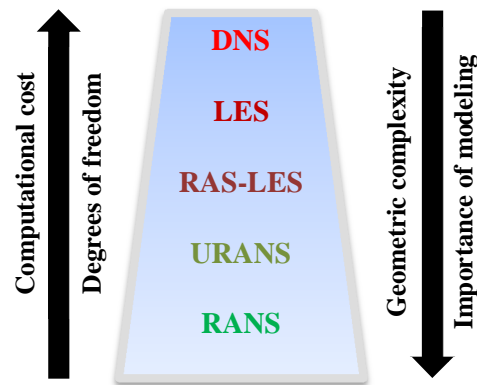
Figure 2.3: Various turbulence models from the simplest to the most complex

The first class or Class I is represented by models that applied the principle of turbulent viscosity of Boussinesq proposed in 1877 (Boussinesq, 1877). These are the turbulence models most used in engineering calculations. The turbulent viscosity hypothesis has been validated in numerous flow cases by experimental results. They integrate the so-called zero-equation models, the best known of which is that of the Prandtl mixing length (Prandtl, 1926). More complex models integrate one equation expressing the turbulent kinetic energy (k) or several equations such as k-ε, k-ω, k-τ…etc. (Durbin, 2017; Dup & Rosenbaum, 1968).

Class II includes models concerned with the closure of the system of Reynolds equations without applying this hypothesis. These are the second-order models where the Reynolds stresses are determined directly. They include the so-called Reynolds Stress Models or RSM. This category can also be classified according to the number of additional partial differential equations that must be solved to provide the modeling parameters. In the most complex cases, this number can reach the value of 12 (Dup & Rosenbaum, 1968; Davidson, 2003).

A final category (class III) can finally be defined. It is the one whose models are not entirely based on the Reynolds equations. The so-called Large Eddy Simulation (or LES) model fall within this category. It comprises a set of conservation equations that is solved instead of those of Reynolds (McDonough, 2007).

The direct numerical solution of the Navier-Stokes equations or Direct Numerical Simulation (DNS) in which these equations are solved numerically without any turbulence model seems to be the ultimate approach. However and due to the wide range of temporal and spatial scales, a direct solution of the Navier-Stokes equations is extremely computationally expensive. The mesh resolution and time steps required to properly resolve the complexity of fluid structures make the DNS approach virtually impossible for engineering applications.

All turbulence models have various advantages but also limits or handicaps mainly caused by the assumptions made during the modelling. No model can be applied effectively to all turbulent flows. Adjustments and some 'experience' are essential to select the most appropriate model for the particular case under consideration that would be able to perform accurate, consistent and robust simulations.

2.3.5. The SST *k-ω* model of turbulence

Shear Stress Transport *k-ω* model combines the best elements of the two-equation eddy viscosity models *k-ε* and *k-ω* turbulence models. In the proximity of solid boundaries, it acts as *k-ω* model that is directly accommodated to the wall without any additional corrections as in the case with almost all the k-ε models. The behavior of the system reverts to a *k-ε* model in the free stream and shear layers thus abrogating the strong freestream sensitivity of *k-ω* models. The complete formulation of the SST *k-ω* model has been provided by (Menter, 1994). The Reynolds Averaged Navier-Stokes (RANS) equations and the transport equations for *k* and *ω* are provided (Ansys, 2022; Matsson, 2023).

The choice of the k-ω SST model was based essentially on its ability to transition modeling capabilities leading it to be suitable for predicting laminar-to-turbulent transition in boundary layers. Its effectiveness to simulate boundary layer separation, reattachment, and flow with recirculation regions rends it quite adequate for the computations of a large spectrum of engineering cases, including aerodynamics analysis, external and internal flows such as those occurring in propulsion nozzles.

2.3.5.1. Transport equations for the SST *k-ω* model

The development of the SST *k-ω* model is similar to that of the conventional *k-ω* model. It has been developed by (Menter, 1994) leading to the following transport equations for both *k* and *ω* that would be solved in Fluent in conjunction with the Reynolds Averaged Navier-Stokes (RANS) equations (Ansys, 2022). As a result:

$$\frac{\partial}{\partial t}(\rho k) + \frac{\partial}{\partial x_i}(\rho k u_i) = \frac{\partial}{\partial x_j}\left(\Gamma_k \frac{\partial k}{\partial x_j}\right) + \tilde{G}_k - Y_k + S_k \tag{2.45}$$

$$\frac{\partial}{\partial t}(\rho \omega) + \frac{\partial}{\partial x_i}(\rho \omega u_i) = \frac{\partial}{\partial x_j}\left(\Gamma_\omega \frac{\partial \omega}{\partial x_j}\right) + G_\omega - Y_\omega + D_\omega + S_\omega \tag{2.46}$$

2.3.5.2. Effective diffusivity model

In the sst *k-ω* model applied, the effective diffusivities for (*k*) and (*ω*) are expressed as (Ansys, 2022):

$$\Gamma_k = \mu + \frac{\mu_t}{\sigma_k} \qquad \text{and} \qquad \Gamma_\omega = \mu + \frac{\mu_t}{\sigma_\omega} \tag{2.47}$$

with the turbulent viscosity expressed as: $\mu_t = \alpha^* \dfrac{\rho k}{\omega}$ (2.48)

2.3.5.3. Correction in case of low Reynolds numbers flows

In the specific case of low Reynolds flows, the turbulent viscosity is dumped by the coefficient (α^*) given by (Ansys, 2022):

$$\alpha^* = \alpha_\infty^* \left[\frac{\alpha_0^* \left(\dfrac{Re_t}{R_k} \right)}{1 + \dfrac{Re_t}{R_k}} \right] \tag{2.49}$$

With: $\quad Re_t = \dfrac{\rho k}{\mu \omega} \qquad ; \qquad R_k = 6 \qquad ; \qquad \alpha_0^* = \dfrac{\beta_i}{3} \quad$ and $\quad \beta_i = 0.072 \tag{2.50}$

In the case of high Reynolds flows, the damping coefficient (α^*) is taken from the k-ω model and expressed as (Menter, 1994):

$$\alpha^* = \alpha_\infty^* = 1 \tag{2.51}$$

2.3.5.4. Turbulence production model

The term representing the productions of turbulence kinetic energy of k (G_k) and od ω (G_ω) are drawn from the exact equation for the transport of (k) and (ω) that have to be consistent of the Boussinesq hypothesis (Boussinesq, 1877):

$$G_k = -\rho \overline{u_i' u_j'} \frac{\partial u_j}{\partial x_i} = \mu_t S^2 \tag{2.52}$$

$$G_\omega = \alpha \frac{\omega}{k} G_k \tag{2.53}$$

with: $\quad - \quad S = \sqrt{2 S_{ij} S_{ij}} \qquad ; \qquad S_{ij} = \frac{1}{2} \left(\frac{\partial u_j}{\partial x_i} + \frac{\partial u_i}{\partial x_j} \right) \tag{2.54}$

$$- \quad \alpha = \frac{\alpha_\infty}{\alpha^*} \left[\frac{\alpha_0 \left(\dfrac{Re_t}{R_\omega} \right)}{1 + \dfrac{Re_t}{R_\omega}} \right] \qquad ; \qquad R_\omega = 2.95 \tag{2.55}$$

In this case also and in high Reynolds flows:

$$\alpha = \alpha_\infty = 1 \tag{2.56}$$

2.3.5.5. Turbulence dissipation model

The term representing the dissipation of k (Y_k) and of ω (Y_ω) may be expressed as (Ansys, 2022):

$$Y_k = \rho \beta^* f_{\beta^*} k \omega \tag{2.57}$$

$$Y_\omega = \rho \beta f_\beta \omega^2 \tag{2.58}$$

with: - $\beta^* = \beta_i^* \left[1 + \varsigma^* F(M_t) \right]$; $\quad f_{\beta^*} = \begin{cases} 1 & \text{for } \chi_k \leq 0 \\ \dfrac{1 + 680 \chi_k^2}{1 + 400 \chi_k^2} & \text{for } \chi_k \succ 0 \end{cases} \tag{2.59}$

- $\beta = \beta_i \left[1 - \dfrac{\beta_i^*}{\beta_i} \varsigma^* F(M_t) \right]$; $\quad f_\beta = \dfrac{1 + 70 \chi_\omega}{1 + 80 \chi_\omega} \tag{2.60}$

- $\beta^* = \beta_i^* \left[1 + \varsigma^* F(M_t) \right]$; $\quad \beta_i^* = \beta_\infty^* \left[\dfrac{\dfrac{4}{15} + \left(\dfrac{\mathrm{Re}_t}{R_\beta} \right)^4}{1 + \left(\dfrac{\mathrm{Re}_t}{R_\beta} \right)^4} \right] \tag{2.61}$

- $\chi_k = \dfrac{1}{\omega^3} \dfrac{\partial k}{\partial x_j} \dfrac{\partial \omega}{\partial x_j}$; $\quad \chi_\omega = \left| \dfrac{\Omega_{ij} \Omega_{jk} S_{ki}}{\left(\beta_\infty^* \omega \right)^3} \right| \tag{2.62}$

- $\Omega_{ij} = \dfrac{1}{2} \left(\dfrac{\partial u_i}{\partial x_j} - \dfrac{\partial u_j}{\partial x_i} \right)$; $\quad f(M_t) = \begin{cases} 0 & \text{for } M_t \leq M_{t_0} \\ M_t^2 - M_{t_0}^2 & \text{for } M_t \succ M_{t_0} \end{cases} \tag{2.63}$

and: - $\varsigma^* = 1.5$; $R_\beta = 8$; $\beta_\infty^* = 0.09$; $M_t^2 = \dfrac{2k}{a^2}$; $M_{t_0} = 0.25$; $a = \sqrt{\gamma R_G T} \tag{2.64}$

- $a_\infty^* = 1$; $\mathrm{a}_\infty = 0.52$; $\alpha_0 = \dfrac{1}{9}$; $\beta_\infty^* = 0.09$; $\beta_i = 0.072$; $R_\beta = 8$

$R_k = 6$; $R_\omega = 2.95$; $\varsigma^* = 1.5$; $M_{t_0} = 0.25$; $\sigma_k = 2.0$; $\sigma_\omega = 2.0 \tag{2.65}$

2.4. The isentropic flow and its describing equations

2.4.1. Entropy

Unlike energy, entropy is a non-conservative property and therefore there is no principle of conservation of entropy. The second law of thermodynamics often leads to expressions involving inequalities. The one stated by by R.J.E. Clausius in 1865 (Clausius, 1865) is applicable to any thermodynamic cycle whether reversible or not, and may be expressed as:

$$\oint \frac{\delta Q}{T} \leq 0 \tag{2.66}$$

By focusing on the case of a volume of gas that has been compressed then expanded in a piston-cylinder system, it is clear that the volume gets back to its initial value leading to a zero net variation of volume. This may be expressed by:

$$\oint d\mathrm{V} = 0 \tag{2.67}$$

This can apply to any property. A quantity whose integral during a cycle is zero depends in fact solely on the initial and final states (not on the process between them). Hence $\left(\dfrac{\delta Q}{T} \right)_{rev.}$

represents a property in differential form. It was this analysis that led R.J.E. Clausius to define the entropy property that was noted (S) and expressed in (kJ/K) as:

$$dS = \left(\frac{\delta Q}{T}\right)_{\text{rév.}}$$
(2.68)

During a process, the entropy is determined by integrating its differential expression (equation 2.68) between the initial state (1) and the final state (2):

$$\Delta S = S_2 - S_1 = \int_1^2 \left(\frac{\delta Q}{T}\right)_{\text{rév.}} = \int_1^2 \left(\frac{\delta Q}{T_0}\right)_{\text{rév.}} = \frac{1}{T_0} \int_1^2 (\delta Q)_{\text{rév.}} = \frac{Q}{T_0}$$
(2.69)

where: T_0 :   is the constant temperature of the system,

Q :   is the amount of heat transferred during the reversible process.

Entropy can also be expressed in terms of internal energy and enthalpy. By considering the energy conservation equation for a steady flow:

$$\delta Q_{\text{rév.}} - \delta W_{\text{rév.}} = dU$$
(2.70)

Replacing heat and work by their respective expressions leads to:

$$TdS - PdV = dU$$

or: $$TdS = dU + PdV$$
(2.71)

or by unit mass:

$$Tds = du + Pd\vartheta$$
(2.72)

thus: $$ds = \frac{du}{T} + \frac{Pd\vartheta}{T}$$
(2.73)

By applying the definition of enthalpy and substituting into equation 2.72, it comes:

$$h = u + P\vartheta \implies dh = du + Pd\vartheta + \vartheta dP$$

$$Tds = dh - \vartheta dP$$
(2.74)

thus: $$ds = \frac{dh}{T} - \frac{\vartheta dP}{T}$$
(2.75)

During a process, the variation in entropy is established by integrating either equation 2.73 or 2.75 between the initial and final states. The application for an ideal gas:

$$du = C_v dT \;\; ; \;\; dh = C_p dT \;\; ; \;\; P\vartheta = R_G T \implies P = \frac{R_G T}{\vartheta} \;\; \text{ou} \;\; \vartheta = \frac{R_G T}{P}$$
(2.76)

leads to:

$$ds = C_v(T)\frac{dT}{T} + R_G \frac{d\vartheta}{\vartheta} \implies s_2 - s_1 = \int_1^2 C_v(T)\frac{dT}{T} + R_G \ln\left(\frac{\vartheta_2}{\vartheta_1}\right)$$
(2.77)

$$ds = C_p(T)\frac{dT}{T} - R_G \frac{dP}{P} \implies s_2 - s_1 = \int_1^2 C_p(T)\frac{dT}{T} - R_G \ln\left(\frac{P_2}{P_1}\right)$$
(2.78)

Any Simplification of integration procedure would require assuming both the specific heats at constant volume and constant pressure. For an ideal gas, this is a fairly common approximation whose resulting error is generally acceptable:

$$s_2 - s_1 = C_v \ln\left(\frac{T_2}{T_1}\right) + R_G \ln\left(\frac{\vartheta_2}{\vartheta_1}\right) \tag{2.79}$$

$$s_2 - s_1 = C_p \ln\left(\frac{T_2}{T_1}\right) - R_G \ln\left(\frac{P_2}{P_1}\right) \tag{2.80}$$

2.4.2. Isentropic flow of ideal gases

An isentropic flow is a thermodynamic process, during which the entropy of the fluid (S) remains constant, i.e.:

$$\Delta S = 0 \quad \text{or} \quad s_2 = s_1 \quad \text{or} \quad s_2 - s_1 = 0 \tag{2.81}$$

An isentropic flow is in fact adiabatic and reversible. Such an idealized mechanism is very useful in engineering as it can serve as a basis of comparison to real processes (Çengel et al., 2019). In the case of an isentropic flow and knowing that $R_G = C_p - C_v$ and $\gamma = \dfrac{C_p}{C_v}$, equations 2.79 and 2.80 become:

$$\ln\left(\frac{T_2}{T_1}\right) = -\frac{R_G}{C_v} \ln\left(\frac{\vartheta_2}{\vartheta_1}\right) = \ln\left(\frac{\vartheta_1}{\vartheta_2}\right)^{\frac{R_G}{C_v}}$$

$$\left(\frac{T_2}{T_1}\right)_{s=cste} = \left(\frac{\vartheta_1}{\vartheta_2}\right)^{\gamma-1} \tag{2.82}$$

$$\ln\left(\frac{T_2}{T_1}\right) = \frac{R_G}{C_p} \ln\left(\frac{P_2}{P_1}\right) = \ln\left(\frac{P_2}{P_1}\right)^{\frac{R_G}{C_p}}$$

$$\left(\frac{T_2}{T_1}\right)_{s=cste} = \left(\frac{P_2}{P_1}\right)^{\frac{\gamma-1}{\gamma}} \tag{2.83}$$

Leading to:

$$\left(\frac{P_2}{P_1}\right) = \left(\frac{\vartheta_1}{\vartheta_2}\right)^{\gamma} \tag{2.84}$$

or: $\quad P\vartheta^{\gamma} = \text{constant} \quad ; \quad T\vartheta^{\gamma-1} = \text{constant} \quad ; \quad TP^{\frac{1-\gamma}{\gamma}} = \text{constant} \tag{2.85}$

2.4.3. High-speed isentropic flow and total properties

For high-velocity flows, such as those occurring in a nozzle during the expansion of the combustion gases, the potential energy of the fluid is negligible against that of the kinetic energy. In

such cases, it is convenient to combine the enthalpy and kinetic energy of the fluid into a single term called total or stagnation enthalpy which is defined per unit mass as:

$$h_0 = h + \frac{V^2}{2} \tag{2.86}$$

In the case of an ideal gas whose enthalpy is expressed as a function of the temperature (Equation 2.76) and where it is common to approximate the specific heat as a constant, equation 2.86 becomes:

$$C_p T_0 = C_p T + \frac{V^2}{2} \Rightarrow T_0 = T + \frac{V^2}{2C_p} \tag{2.87}$$

where: - T_0 : is the total or stagnation temperature,

- $\dfrac{V^2}{2C_p}$: is the dynamic temperature.

In the same way, and using equations 2.822 and 2.83 while expressing the density as: $\left(\rho = \dfrac{1}{\vartheta} \right)$, we can write:

$$\frac{\rho_0}{\rho} = \left(\frac{T_0}{T} \right)^{\frac{1}{\gamma-1}} \tag{2.88}$$

$$\frac{P_0}{P} = \left(\frac{T_0}{T} \right)^{\frac{\gamma}{\gamma-1}} \tag{2.89}$$

2.4.4. Speed of sound and Mach number

An important parameter in compressible flows is represented by the speed of sound defined as the speed at which an infinitesimal pressure wave travels within a medium. Considering an isentropic flow, it can be demonstrated (Moran et al., 2014) that the speed of sound may be expressed as:

$$a^2 = \left(\frac{\partial P}{\partial \rho} \right)_{s=constant} = \frac{\gamma P}{\rho} = \gamma R_G T$$

and: $\quad a = \sqrt{\gamma R_G T} \tag{2.90}$

A second equally important parameter in the study of compressible fluid flows is represented by the Mach number defined as the ratio of the fluid actual velocity to that of the sound in the same medium:

$$M = \frac{V}{a} \tag{2.91}$$

2.4.5. Isentropic relations of an ideal gas

Using the relationship defining the speed of sound (Equation 2.90) as well as that of the Mach number (Equation 2.91) and expressing the specific heat at constant pressure as a function

only of both the ideal gases constant (R_G) and the ratio of specific heats (γ), the relationships combining the static properties to the total or stagnation ones expressed by equations 2.87, 2.88 and 2.89 can be derived and expressed solely in terms of the Mach number:

$$\frac{T_0}{T} = 1 + \left(\frac{\gamma-1}{2}\right)M^2 \tag{2.92}$$

$$\frac{P_0}{P} = \left[1 + \left(\frac{\gamma-1}{2}\right)M^2\right]^{\frac{\gamma}{\gamma-1}} \tag{2.93}$$

$$\frac{\rho_0}{\rho} = \left[1 + \left(\frac{\gamma-1}{2}\right)M^2\right]^{\frac{1}{\gamma-1}} \tag{2.94}$$

2.5. The propulsion nozzles: Operation, types and main performance parameters

2.5.1. General

A nozzle can be defined as a pipe of non-constant circular section. It is a fundamental element associated with the expansion of gases, their flow rate at high velocities and consequently propulsion. It can be convergent or divergent. The present section focuses on the profile that has been initially developed in the 19th century by the Swedish engineer Carl Gustaf Patrik de Laval (1845-1913) for an initial application to steam turbines, and has since then be used in almost all rocket engines. A Convergent-Divergent (C-D) nozzle, such as the one illustrated in Figure 2.4, that can achieve supersonic exit velocities is essentially constituted by a convergent section, a throat and a divergent section.

A supersonic (or de-Laval) nozzle is therefore a convergent-divergent configuration located between the combustion chamber (or tank at high pressure) and the external environment of any jet engine that equips rockets. Its main function is to accelerate the combustion gases coming from the combustion chamber (or the gases possessing high pressures of a tank) to speeds greater than the speed of sound. Its profile allows gases to be expanded, transforming the potential energy of the gases into kinetic energy. All along the nozzle, the speed of the gases increases while its pressure and temperature decrease.
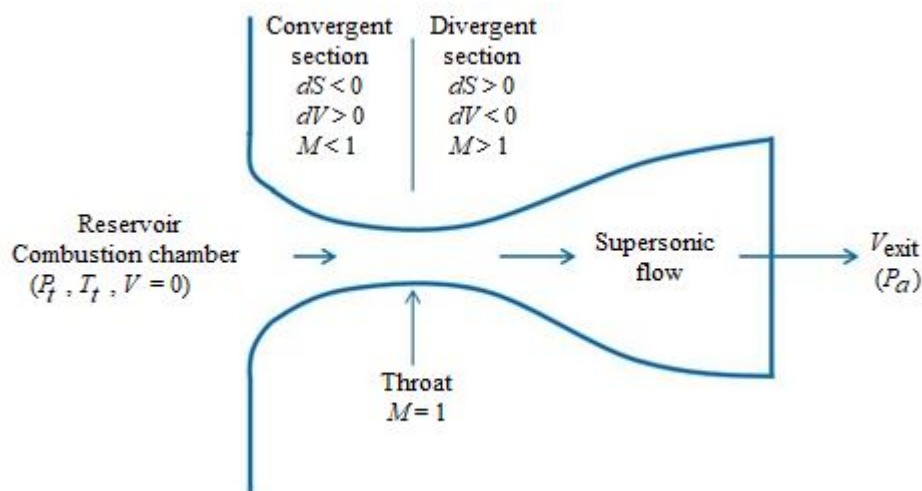
Figure 2.4: Convergent divergent nozzle

2.5.2. Operation of supersonic nozzles: the isentropic flow

A simulation of the operation of a propulsion nozzle is essential to the understanding of the process of the gases' expansion during their passage through the convergent, throat and divergent. An understanding of the operation that takes place within a C-D nozzle requires examining the procedure within a convergent-only type nozzle. To this end,

Knowledge of relationships linking essential parameters such as the pressure, the temperature, the density and the velocity to the area and Mach number within a one-dimensional isentropic flow is essential. For such a flow, the mass flow rate may be expressed as:

$$\dot{m} = \rho V S = \text{constante} \Rightarrow \frac{d\rho}{\rho} + \frac{dV}{V} + \frac{dS}{S} = 0 \tag{2.95}$$

For a steady flow without heat exchange, and neglecting the potential energy, the relationship that expresses the conservation of momentum and mass equations may be written as:

$$\frac{dP}{\rho} + VdV = 0 \tag{2.96}$$

$$\left. \begin{array}{l} \frac{d\rho}{\rho} + \frac{dV}{V} + \frac{dS}{S} = 0 \\[2mm] \frac{dP}{\rho} + VdV = 0 \end{array} \right\} \Rightarrow \frac{dS}{S} = \frac{dP}{\rho}\left(\frac{1}{V^2} - \frac{d\rho}{dP}\right) \quad \text{ou} \quad \frac{dS}{S} = \frac{dP}{\rho V^2}\left(1 - M^2\right) \tag{2.97}$$

Applying equation 2.96 to express the ratio: $\left(\frac{dP}{\rho} = -VdV\right)$, and substituting into equation 2.97 leads to:

$$\frac{dS}{S} = -\frac{dV}{V}\left(1 - M^2\right) \tag{2.98}$$

Equation 2.98 is the relationship that governs the profile of a nozzle (whether convergent or divergent) and the flow (whether isentropic subsonic or supersonic). Indeed:

- At subsonic speeds : $M \prec 1 \Rightarrow \dfrac{dS}{dV} \prec 0$

- At supersonic speeds : $M \succ 1 \Rightarrow \dfrac{dS}{dV} \succ 0$

- At sonic speeds : $M = 1 \Rightarrow \dfrac{dS}{dV} = 0$
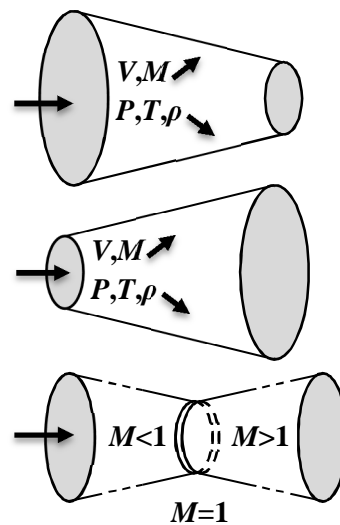
It therefore appears that a supersonic flow-field can only be reached within a nozzle if the flow is sonic at the throat ($M=1$) where the properties are called critical and are labelled with a (*).

The critical ratios are expressed by equations 2.92, 2.93 and 2.94. By setting the Mach number equal to 1 in the latter relationships, the critical ratios would be expressed as:

$$\frac{T^*}{T_0} = \frac{2}{\gamma+1} \tag{2.99}$$

$$\frac{P^*}{P_0} = \left(\frac{2}{\gamma+1}\right)^{\frac{\gamma}{\gamma-1}} \tag{2.100}$$

$$\frac{\rho^*}{\rho_0} = \left(\frac{2}{\gamma+1}\right)^{\frac{1}{\gamma-1}} \tag{2.101}$$

2.5.2.1. Convergent nozzles

In the case of a converging nozzle such as that illustrated in Figure 2.5, the cross section area gradually decreases in the direction of flow. The velocity increases up to that of the sound at throat i.e. where the Mach number reaches unity when chocked.
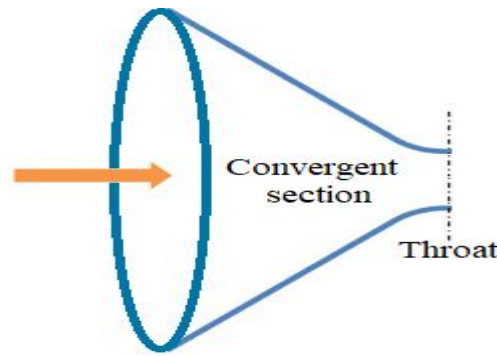
Figure 2.5: Convergent nozzle

Under steady flow conditions, the mass flow rate through a nozzle is constant, and may be expressed as:

$$\dot{m} = \rho V S = \left(\frac{P}{R_G T}\right)\left(M\sqrt{\gamma R_G T}\right)S = PMS\sqrt{\frac{\gamma}{R_G T}} \tag{2.102}$$

Replacing (T) and (P) with their expressions in equations 2.92 and 2.93 will introduce the stagnation properties and express the mass flow rate as:

$$\dot{m} = \frac{MSP_0\sqrt{\dfrac{\gamma}{R_G T_0}}}{\left[1+\dfrac{(\gamma-1)M^2}{2}\right]^{\frac{\gamma+1}{2(\gamma-1)}}} \tag{2.102}$$

For specified stagnation temperature and pressure, and for a defined cross-sectional area, the maximum mass flow rate that may occur in a nozzle is obtained for a unity Mach number:

$$\dot{m}_{max.} = S^*P_0\sqrt{\frac{\gamma}{R_G T_0}}\left(\frac{2}{\gamma+1}\right)^{\frac{\gamma+1}{2(\gamma-1)}} \tag{2.103}$$

The preceding equations 2.102 and 2.103 provide a relationship that links the variation of any cross-section area to that at the throat:

$$\frac{S}{S^*} = \frac{1}{M}\left[\left(\frac{2}{\gamma+1}\right)\left(1+\frac{\gamma-1}{2}M^2\right)\right]^{\frac{\gamma+1}{2(\gamma-1)}} \tag{2.104}$$

The various properties of an isentropic one-dimensional compressible flow may then be expressed as function of the Mach number. An overview of these data is presented in Table 2.1.

Table 2.1: Properties of the compressible flow of an ideal gas with $\gamma=1.4$ (Elger et al., 2022)

M	P/P_t	ρ/ρ_t	T/T_t	S/S^*
0.0	1.0000	1.0000	1.0000	∞
0.2	0.9725	0.9803	0.9921	2.9630
0.4	0.8956	0.9243	0.9690	1.5901
0.6	0.7840	0.8405	0.9328	1.1882
0.8	0.6560	0.7400	0.8865	1.0382
1.0	0.5283	0.6339	0.8333	1.000
2.0	0.1278	0.2300	0.5556	1.688
3.0	0.02722	0.07623	0.3571	4.235
4.0	0.006586	0.02766	0.2381	10.72
5.0	0.001890	0.01134	0.1667	25.00
6.0	0.006334	0.005194	0.1220	53.18
7.0	0.0002416	0.002609	0.09259	104.1
8.0	0.0001024	0.001414	0.07246	190.1
9.0	0.00004739	0.0008150	0.05814	327.2
10.0	0.00002356	0.0004948	0.04762	535.9
0.0	1.0000	1.0000	1.0000	∞

2.5.2.2. Convergent-Divergent (de Laval) nozzles

In the case of a de-Laval nozzle where a diverging section is located immediately downstream of the convergent and as soon as the velocity at the throat reaches the speed of sound, the flow velocity will increase along with the decrease of the back pressure (i.e. the downstream pressure). In this case, supersonic velocities can be attained within the divergent. However, 'forcing' a fluid through a C-D nozzle does not guarantee achieving supersonic speeds. This is because the fluid may find itself slowing down in the diverging section instead of accelerating if the back pressure is not within the necessary required range. The flow regime within a nozzle is determined by the overall pressure ratio. Therefore and for given inlet conditions, the flow rate through the nozzle is controlled by the downstream pressure.

Considering the C-D nozzle of Figure 2.6, the different flow scenarios that take place within a Condi nozzle may be simulated by reducing the downstream pressure (P_{back}).
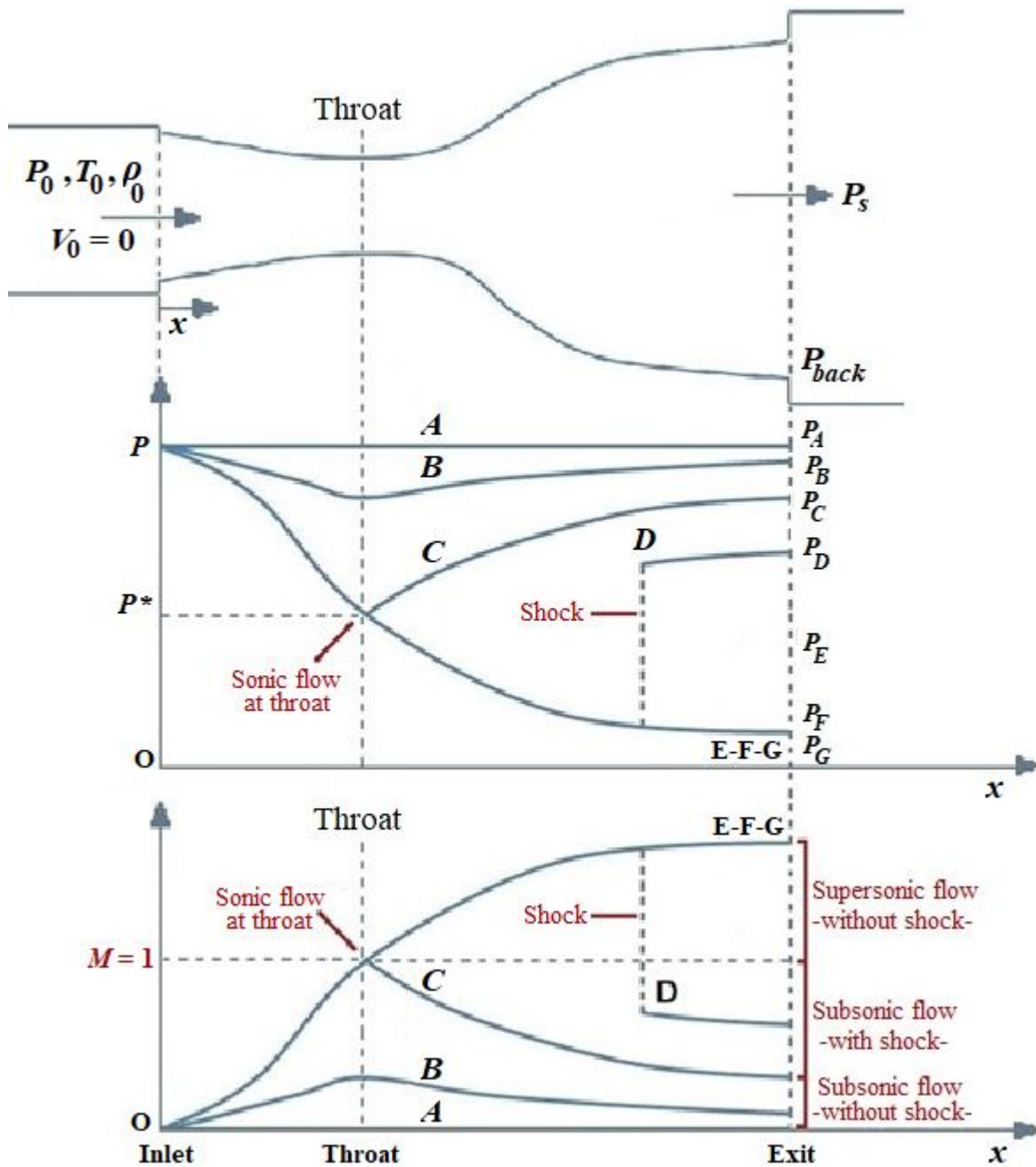
Figure 2.6: C-D nozzle and pressure and Mach profiles

Case 1 : $P_{back} = P_0$ There is no flow. This is predictable given that the flow is driven by the difference in pressure at inlet and exit.

Case 2 : $P_{back} > P_0$

    $P_{back} < P_C$ The flow remains subsonic all along the nozzle, and the flow rate is lower than the critical value. The velocity increases in the converging section, reaches its maximum at the throat. With a Mach lower that unity ($M_{throat} < 1$) at throat, the velocity will decrease in the divergent section which will therefore act as a diffuser. Conversely, the pressure decreases and reaches a minimum at the throat before increasing.

Case 3: $P_{back} = P_C$ In this case, the pressure at the throat reaches the critical value (P^*) leading to a sonic velocity there ($M_{throat} = 1$), but the divergent section of the nozzle continues to act as a diffuser slowing the flow to subsonic

speeds. The mass flow rate which increased with the decrease of the back pressure (P_{back}) also reached its maximum value. Any subsequent additional reduction in back pressure will have no influence either on the speed of the flow or on its flow rate within the converging section of the nozzle. However, it influences the character of the flow in its divergent section.

Case 4 : $P_{back} > P_E$

$P_{back} < P_C$ The fluid having reached the sonic velocity at the throat will continue its acceleration in order to reach, as the pressure decreases, supersonic speeds in the divergent section. This acceleration is nevertheless stopped because of the appearance of a normal shock that tends to develop along a cross-section downstream of the throat leading to a sudden increase in pressure accompanied by a drop in velocity to subsonic regimes. The fluid continues to slow down within the remaining section of the divergent.

Note that: 1. The flow through the shock is irreversible, and therefore cannot be considered isentropic.
2: The normal shock moves forward in the direction downstream of the throat following the decrease of the back pressure (P_{back}). It will come nearer to the exit with the back pressure (P_{back}) closing on the exit pressure (P_E).

Case 5: $P_{back} = P_E$ The normal shock is established at the exit section of the nozzle, and the flow is therefore supersonic throughout the entire divergent section. In this case, it can be approximated as isentropic. The velocity decreases to subsonic levels after crossing the normal shock i.e. at the exit of the nozzle section.

Case 6 : $P_{back} < P_E$

$P_{back} > 0$ When the back pressure (P_{back}) is lower than (P_E), the flow is completely supersonic along the divergent section and expanding up to the downstream pressure ($P_{back} = P_F$) without the appearance of a shock.

Case 7: $P_{back} = P_F$ No shock occurs along the divergent or at its exit, and the flow can be assumed (approximately) isentropic.

Case 8: $P_{back} < P_F$ Expansion waves take place downstream of the exit section of the nozzle, constituting shock waves.

2.5.2.3. Shock waves

Knowing that pressure disturbances are usually generated by sound waves that move at the speed of sound, supersonic flows taking place in C-D nozzles can be, under certain back pressure conditions, subjected to shock waves or expansion waves.

A flow moving at a speed greater than that of sound and facing a sudden decrease in the flow area generates shock waves that represent an irreversible process where entropy increases. Through a shock wave, the gas static pressure, temperature, and density increase almost instantly while the total enthalpy and temperature remain constant. However, the total pressure downstream of the shock as well the Mach number and the velocity are always found lower than that upstream. If the shock wave is perpendicular to the direction of the flow, it is said to be normal. In the case the shock wave is found inclined with regard to the flow direction, it is called an oblique shock. In the case of a 'weak shock', that occurs quite often, the flow remains supersonic. However, a 'strong shock' would give rise to subsonic solution.

2.5.2.4. Normal shock waves

The equations relating the flow properties upstream and downstream of a straight shock are developed through the application of the conservation equations of mass, momentum and energy. In the present case, the fluid is considered compressible, and the flow is one-dimensional, stationary and inviscid (Figure 2.7).
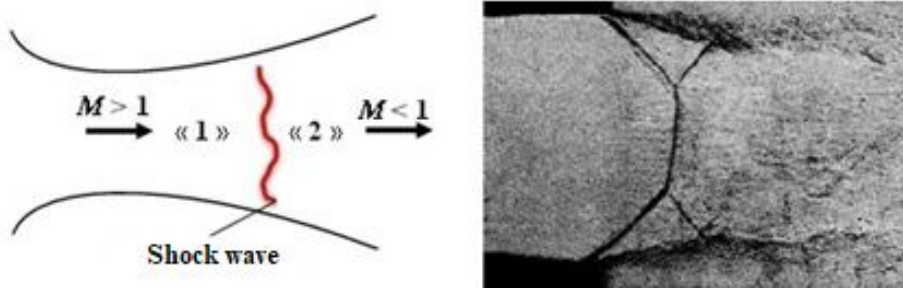
Figure 2.7: Oblique shock wave and its representation

The relationships relating the different properties upstream and downstream of a normal shock for an ideal gas with constant specific heats may be expressed as (Yahya, 2003):

$$\left\{ \frac{P_{t2}}{P_{t1}} = \left[\frac{(\gamma+1)M_1^2}{(\gamma-1)M_1^2+2} \right]^{\frac{\gamma}{\gamma-1}} \left[\frac{(\gamma+1)}{2\gamma M_1^2-(\gamma-1)} \right]^{\frac{1}{\gamma-1}} \quad ; \quad \frac{T_{t2}}{T_{t1}} = 1 \right. \tag{2.105}$$

$$\left\{ \begin{array}{ll} \dfrac{P_2}{P_1} = \dfrac{2\gamma M_1^2-(\gamma-1)}{\gamma+1} & ; \quad \dfrac{T_2}{T_1} = \dfrac{\left[2\gamma M_1^2-(\gamma-1)\right]\left[(\gamma-1)M_1^2+2\right]}{(\gamma+1)^2 M_1^2} \\[3mm] \dfrac{\rho_2}{\rho_1} = \dfrac{(\gamma+1)M_1^2}{(\gamma-1)M_1^2+2} & ; \quad M_2^2 = \dfrac{(\gamma-1)M_1^2+2}{2\gamma M_1^2-(\gamma-1)} \end{array} \right. \tag{2.106}$$

2.5.2.5. Oblique shock waves

Oblique shocks are generally generated either when a body moves at supersonic speeds through a medium, or when the flow is forced to change direction such by the leading edge of the wing and tail of a supersonic aircraft. Both cases are represented in Figure 2.8. They can also occur downstream of a supersonic nozzle if the exit pressure is different from that of the medium into which the flow is discharged.
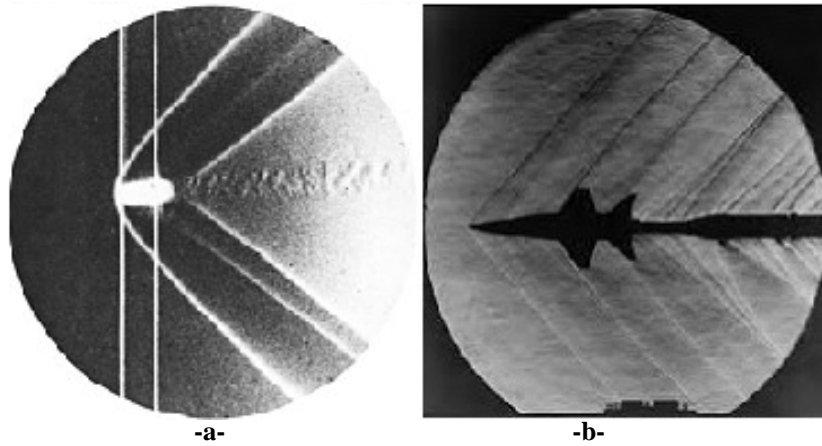
Figure 2.8: Oblique shock waves generated (a) by a bullet moving at a supersonic speed published by E. Mach & P. Salcher in 1887 (b) by a scale model of the American X-15 hypersonic plane published in 1962 by Shutterstock

The equations associating the flow properties upstream and downstream of an oblique shock are the same presented previously for a normal shock i.e. Equations 2.105 and 2.106. Noting the upstream and downstream areas of the wave by (1) and (2) respectively as shown in Figure 2.9, the relationships linking the different properties upstream and downstream of an oblique shock for an ideal gas with constant specific heats may be expressed as (Anderson, 2011):
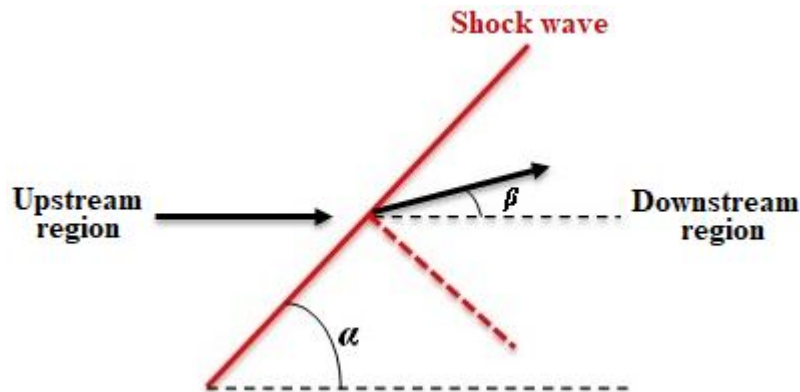
Figure 2.9: Oblique shock wave representation

$$
\begin{cases}
\cot(\beta) = \tan(\alpha) \left\{ \dfrac{(\gamma+1)M_1^2}{2\left[M_1^2 \sin^2(\alpha) - 1 \right]} - 1 \right\} \\[4mm]
\dfrac{P_{t2}}{P_{t1}} = \left[\dfrac{(\gamma+1)M_1^2 \sin^2(\alpha)}{(\gamma-1)M_1^2 \sin^2(\alpha) + 2} \right]^{\frac{\gamma}{\gamma-1}} \left[\dfrac{(\gamma+1)}{2\gamma M_1^2 \sin^2(\alpha) - (\gamma-1)} \right]^{\frac{1}{\gamma-1}}
\end{cases}
\tag{2.107}
$$

$$\begin{cases} \dfrac{P_2}{P_1} = \dfrac{2\gamma M_1^2 \sin^2(\alpha) - (\gamma-1)}{\gamma+1} \\[3mm] \dfrac{T_2}{T_1} = \dfrac{\left[2\gamma M_1^2 \sin^2(\alpha) - (\gamma-1)\right]\left[(\gamma-1) M_1^2 \sin^2(\alpha) + 2\right]}{(\gamma+1)^2 M_1^2 \sin^2(\alpha)} \\[3mm] \dfrac{\rho_2}{\rho_1} = \dfrac{(\gamma+1) M_1^2 \sin^2(\alpha)}{(\gamma-1) M_1^2 \sin^2(\alpha) + 2} \\[3mm] M_2^2 \sin^2(\alpha-\beta) = \dfrac{(\gamma-1) M_1^2 \sin^2(\alpha) + 2}{2\gamma M_1^2 \sin^2(\alpha) - (\gamma-1)} \end{cases} \qquad (2.108)$$

2.5.2.6. Expansion waves

The solution of an oblique shock with an angle (α) that obstructs a supersonic flow and reducing its Mach number and velocity (§ 2.5.2.5) is similar to that of expansion waves with the exception that in the case of expansion waves, the modifications in terms of the flow angle are gradual and expanding. This distinctive characteristic results in a flow growth area and an increase of the Mach number and velocity. As a result, the expansion waves do produce a shock wave but rather a region in continuous expansion-relaxation constituted by a large number of Mach waves commonly known as Prandtl-Meyer expansion waves. These local deflections are so small that the flow can be assumed to be isentropic, allowing the application of the isentropic ideal gas equations represented in equations 2.92, 2.93 and 2.94 for a perfect gas.

Established by Ludwig Prandtl and Theodor Meyer (Liepmann & Roshko, 2001), the Prandtl-Meyer function describes the angle, which can be expressed in degrees or radians, by which an isentropic flow must expand from sonic speed ($M=1$) to a supersonic Mach. For an ideal gas, it is expressed as:

$$\begin{cases} v_1(M_1) = \sqrt{\dfrac{\gamma+1}{\gamma-1}} \tan^{-1}\left(\sqrt{\dfrac{\gamma-1}{\gamma+1}(M_1^2-1)}\right) - \tan^{-1}\left(\sqrt{M_1^2-1}\right) \\[3mm] v_2(M_2) = \sqrt{\dfrac{\gamma+1}{\gamma-1}} \tan^{-1}\left(\sqrt{\dfrac{\gamma-1}{\gamma+1}(M_2^2-1)}\right) - \tan^{-1}\left(\sqrt{M_2^2-1}\right) \end{cases} \qquad (2.109)$$

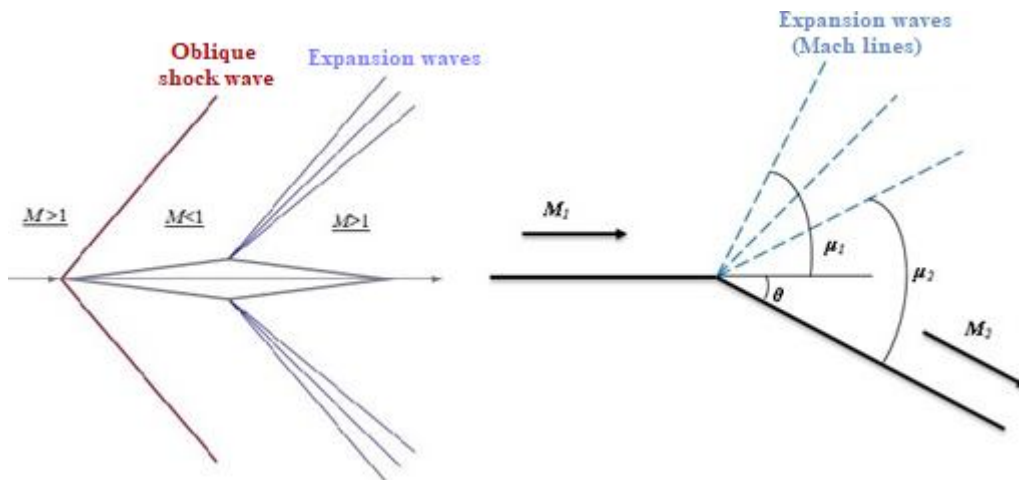**Figure 2.10:** Representation de 3 expansion waves (in fat there is infinity) for a flow deviated by an angle (θ), (μ_1) and (μ_2) representing the Mach angles

2.5.3. Different types of C-D nozzles

Supersonic (or de Laval) nozzles accelerate the combustion gases to speeds higher than that of the sound and to do so, in the case of rockets, they are positioned between the combustion chamber and the exit. The need to achieve a maximum thrust within a minimum length and therefore a minimum weight led to the development of several nozzle configurations including ideal, conical, contour, plug, dual bell, expansion-deflection and multi grid profiles.

The conical nozzle constituted the common shape in early rocket engines development. Its preeminent advantage resides in its ease and flexibility to be manufactured in diverse area ratios as its wall is designed as a straight line with commonly a 15° divergent angle (Figure 2.11). It is however much restrained in terms of weight and performance loss at low altitude (Bani, 2016). This loss of thrust due to divergence is taken into account using a correction factor depending mainly on the angle of divergence (α) and defined as:

$$\lambda = \frac{1 + \cos{(\alpha)}}{2} \qquad\qquad (2.110)$$
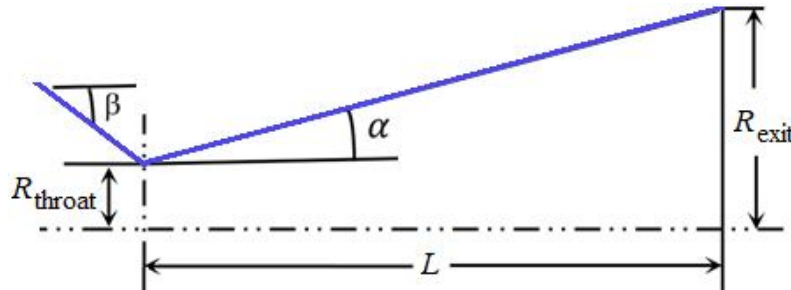
Figure 2.11: Conical nozzle

Conical nozzles are more practical for small propulsion engines. The length of this type of nozzle is small relative to that of the ideal nozzle. This configuration is often used as a basis for comparison in terms of thrust and length. An overview of the design and optimization of conical supersonic nozzles has been provided by (Haque et al., 2021). It covered the various aspects of conical nozzle design, including the effects of nozzle geometry on flow behavior, the use of numerical simulations to optimize nozzle performance, and the impact of nozzle design on engine efficiency and thrust. An analysis of a small-scale rocket propulsion system conical nozzle was performed by (Rizal et al., 2018) while the design of a conical nozzle was accomplished for the purpose of flying rockets at high altitudes (Nalim & Samuelsen, 2018). Oblique shock waves were investigated in terms of design and performance optimization when they occur in conical supersonic nozzles (Bian et al., 2022).
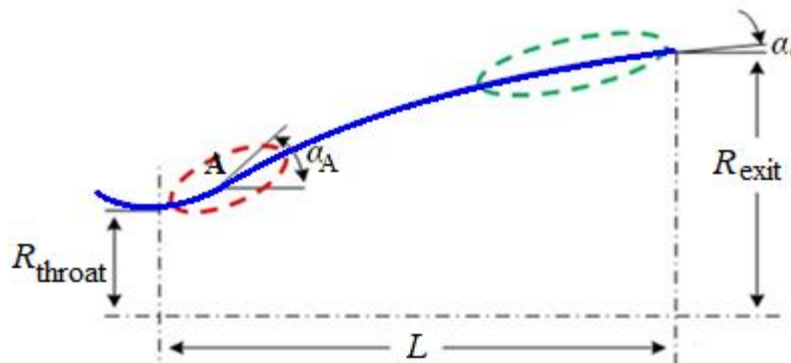
Figure 2.12: Contoured or bell-shaped nozzle

Unlike traditional convergent-divergent nozzles, contoured or bell-type nozzles have a variable shape that can be adjusted based on the operating conditions and are widely used in supersonic engines to increase performance and efficiency (Figure 2.12).

Bell-type nozzles with their high angle of expansion established at 20°-50° right downstream of the throat followed by a gradual reversal of the contour slope to achieve around 5°-10° half angle at the exit lip have been found to be approximately 20% shorter in length and consequently lighter (Sutton & Biblarz, 2016). One of their primary benefits is their ability to reduce shock losses. They have been shown to being able to improve engine performance by up to 5% to 7%. Elnady and Shyy (Elnady & Shyy, 2021) discussed the benefits of contoured nozzles over traditional convergent-divergent nozzles in terms of design, optimization and manufacturing processes. Their application in ramjet engines was introduced (Mishra & Sinha, 2019), and their optimization for use in high-altitude supersonic cruise was investigated (Arora & Kandula, 2020).

Conventional propulsion nozzles having axisymmetric convergent-divergent geometries disadvantages include excessive lengths and poor performance beyond the design point. A number of concepts produced through the insertion of axisymmetric central bodies in conventional nozzles have been considered to overcome these disadvantages, the central body being located upstream, downstream or at the throat of the axisymmetric geometry. Because of the central body, the combustion gases undergo an expansion in the divergent ring constituted by the convergent contour of the central body and the divergent section of the nozzle (Figure 2.13).
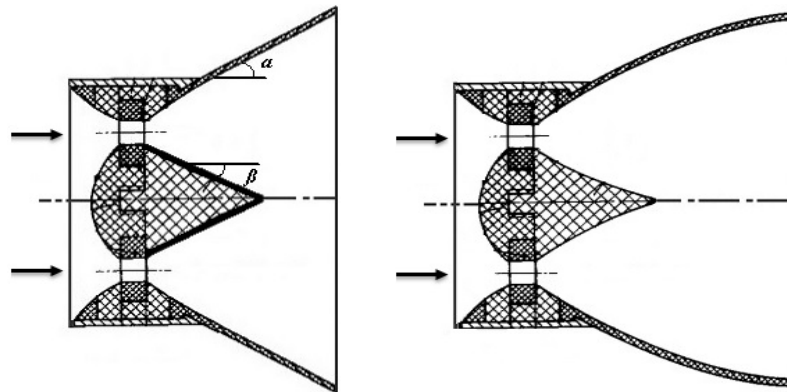
Figure 2.13: Annular nozzles with conical and contoured (or bell-shaped) profiles

If the contour is conical, the thrust is reduced by a factor (λ) which may be expressed as:

$$\lambda = \frac{\frac{1}{2}\left(\sin\alpha + \sin\beta\right)^2}{(\alpha + \beta)\sin\beta + \cos\beta - \cos\alpha} \tag{2.111}$$

where (α) and (β) represent the angles formed by the nozzle axis of symmetry and the outer wall for (α) and the nozzle axis of symmetry and the inner wall of the central body for (β).

Identical to the thrust developed by converging-diverging nozzles is the plug type nozzle. They essentially consist of a central body or 'plug' around which the combustion gases expand from the stagnation pressure prevailing in the combustion chamber to that of the ambient pressure. The throat of such configurations has the shape of a ring located at the outer diameter as shown in Figure 2.14 (Hageman et al., 1998).
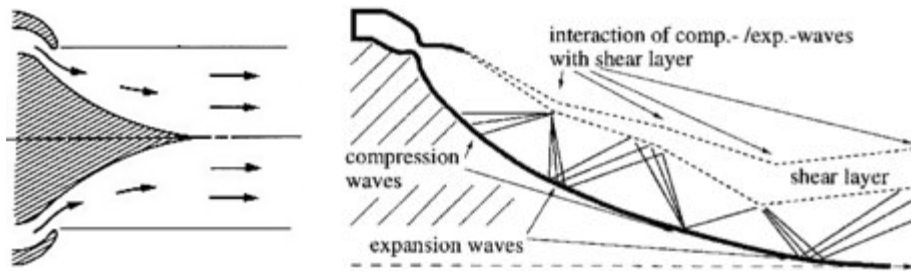
Figure 2.14: Center body and flow phenomena of a plug nozzle with full length (Hageman et al., 1998)

Their applications are multiple extending to airplanes, rockets and many other fluid flow devices. They belong to the class of so-called altitude-compensated nozzles which, unlike traditional conical and contour nozzles, maintain significant efficiency at a wide range of altitudes (O'Leary et al., 1992). They furthermore are able to provide variable thrust and specific impulse. Recent developments in plug-type nozzles in terms of design and optimization along with their ability to improve the performance and efficiency of rocket engines for space exploration and other applications are discussed by (Hsu et al., 2021). A numerical investigation was carried out by Shen et al. (Shen et al., 2019) in order to show the influence of mesh refinement on the performance of plug nozzles, while a numerical optimization was accomplished for a reusable rocket engine (Li et al., 2018). Potential applications concerning plug nozzles have been highlighted over the years by diverse authors (Migdal, 1972; Kim et al., 2009; Lee et al., 2012; Shin & Jeong, 2015).

The Expansion-Deflection (E-D) nozzle resembles to a contoured nozzle except that a central body has been integrated into the throat thus diverting the flow of gases coming from the combustion chamber towards the walls of the diverging section. The fact that these gases expand significantly near the throat before being directed to the outlet section allows for shorter configurations than the standard contoured geometries while maintaining the expected expansion rates (Figure 2.15). They consist of a divergent section, similar to a conventional nozzle, but with a series of ramps or wedges that deflect the flow of exhaust gases to achieve additional thrust that would result in improved performance for supersonic aircraft and spacecraft (Zhao et al., 2022).
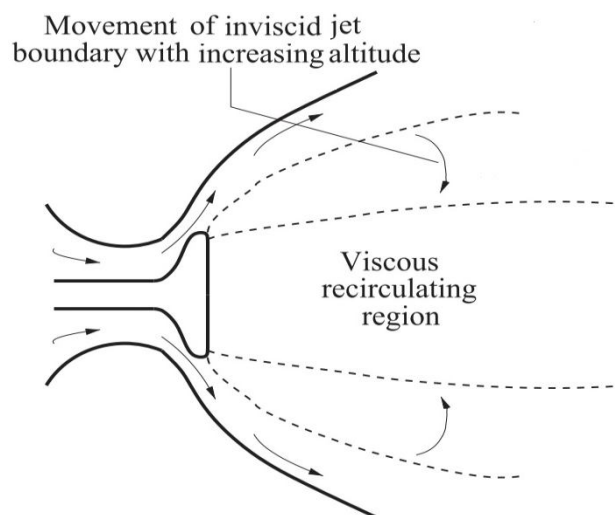
Figure 2.15: E-D type nozzle in open wake mode i.e. at low altitude (Schomberg et al., 2015)

The main advantage of E-D nozzles resides in their ability to provide a significant increase in thrust over a conventional nozzle, without requiring additional fuel or engine power. They use a

combination of shock waves and boundary layer interactions to control the flow of exhaust gases (Figure 2.16).
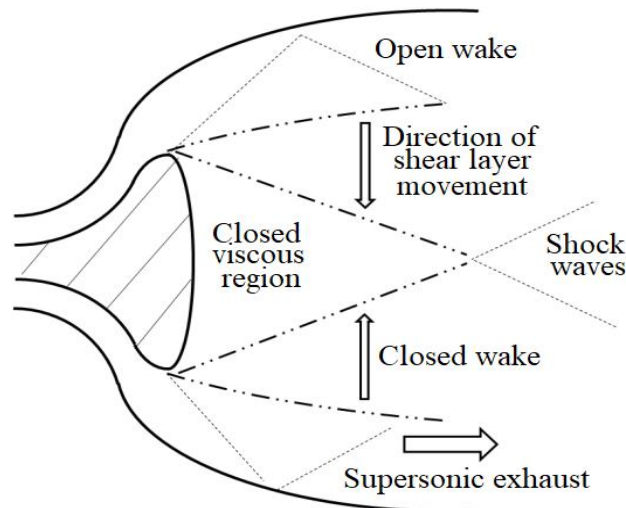
Figure 2.16: E-D type nozzle in closed wake mode i.e. at high altitude (Schomberg et al., 2014)

If the central body is designed to move along its axis of rotation, the throat surface area will vary leading to effective throttling while maintaining chamber pressure (Schorr, 1970). This type of nozzle is suitable for the upper stages of aerospace vehicles where it would be used in low pressure or vacuum environments. In this case, it would offer reductions in weight and length as well as a substantial increase in specific impulse compared to conventional configurations (Goetz et al., 2005). Recent research on E-D nozzles has focused on improving their efficiency and reducing their weight and complexity. This has led to the development of new materials and manufacturing techniques, as well as the use of advanced computational modeling tools to optimize their design (Huang et al., 2021; Choi & Huh, 2022; Lee et al., 2022). Recent research on E-D nozzles focused on improving their efficiency and reducing their weight and complexity. This has led to the development of new materials and manufacturing techniques, as well as the use of advanced computational modeling tools to optimize their design.

A comparison between the diverse nozzles configurations described above shows the difference in terms of length and consequently weight (Figure 2.17).
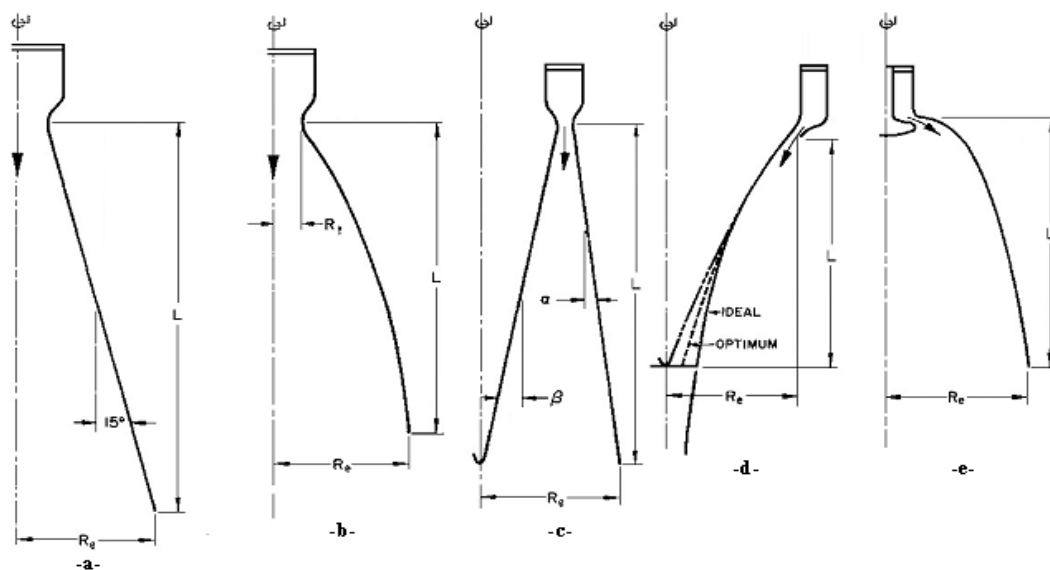
Figure 2.17: Comparison of different types of rocket nozzles (Rao, 1961)
a) Conical, b) Contoured, c) annular, d) plug-type, e) E-D type

The design of large nozzles is generally faced with a significant length of the divergent section that would lead to excessive weight. An optimization of the profile is therefore needed. Two types of optimized profiles have been developed and produced good results (Mahfoudi et al., 2014). These are the Truncated Ideal Contour (TIC) and the Thrust-Optimized Parabolic (TOP) nozzles. The profile of a nozzle with a truncated ideal contour is obtained from that of an ideal reference nozzle designed to generate a parallel flow at the exit. For the sake of optimization, the nozzle divergent is truncated at the cost of a weight gain and a relatively limited loss of thrust (Mahfoudi et al., 2014). The TOC truncated nozzle, proposed by (Rao, 1958) has a typical length that is 75% to 85% inferior to that of the conical configuration having a 15°-divergence angle with the same area ratio (i.e. throat to outlet).

One of the geometries that have gained much interest lately is the concept of dual-bell nozzle whose key benefits include providing high thrust efficiency over a wide range of altitudes, improved fuel efficiency, and increased range. These nozzle classes consist essentially of a converging section that expands the gas to sonic speeds at the throat, and two divergent sections of different NPRs that further expand the gas in supersonic mode thus generating thrust (Figure 2.18).
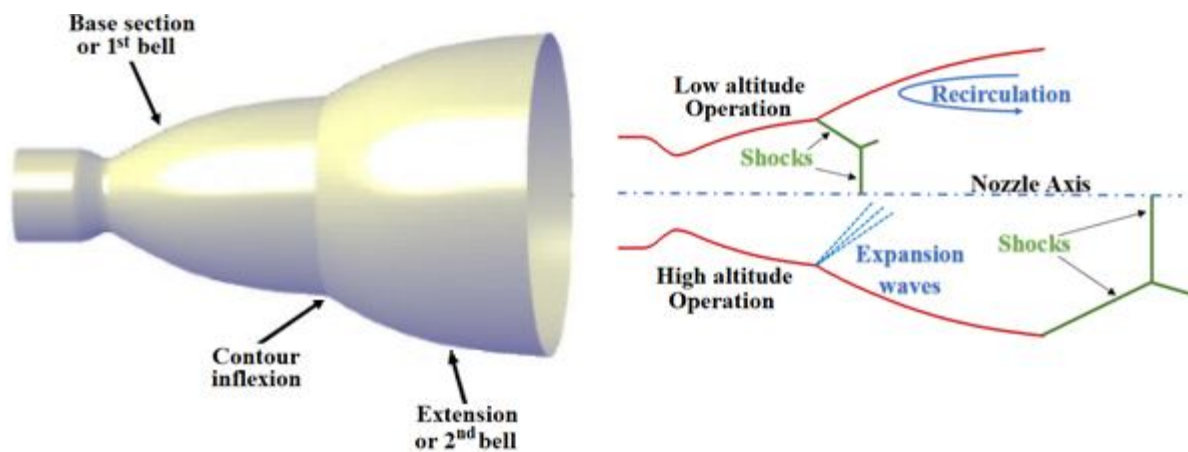
Figure 2.18: Schematic of a dual bell nozzle, and its operating modes (Verma et al., 2000)

Dual bell nozzles are designed to provide high efficiency over a wide range of altitudes. Approaches based on genetic algorithms (Davis & Pappas, 2020) and the method of characteristics (Fernandes et al., 2023) have been applied for the optimization of dual-bell nozzles. Furthermore, both design and optimization of dual-bell nozzles have been carried out in order to integrate them in a reusable rocket engine (Wada et al., 2017). An interesting review paper discussed the recent developments in dual-bell nozzles (Hou & Li, 2021).

Multi-Nozzle Grid (MNG) and Multi-Grid Profiles (MGP) nozzles have been extensively studied in recent years due to their ability to provide efficient expansion of exhaust gases in supersonic and hypersonic applications (Guo et al., 2021). Multi-Nozzle Grid (MNG) nozzles are thin, lightweight and length-short configurations (Figure 2.19).
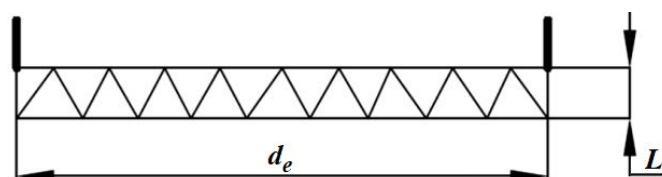
Figure 2.19: Schematic of Multi-Nozzle Grid (MNG) (Khare & Saha, 2021)

Investigations showed the length saving to be in direct proportion to the square root of the number of small nozzles (Chasman et al., 2005; Chasman et al., 2005; Chasman et al., 2012).

While a Multi-Nozzle Grid (MNG) nozzle typically refers to an arrangement of multiple nozzles used in rocket engines or propulsion systems for thrust vectoring, control, and performance optimization, Multi-Grid Profiles (MGP) nozzles refer to a specific type of design that incorporates multiple grids of oblique shock waves to achieve an efficient expansion of exhaust gases in order to improve fluid flow uniformity and reduce turbulence or noise. The oblique shock waves are generated by a series of ramps or wedges arranged in a specific configuration, which can be optimized for different operating conditions (Yang et al., 2020). Recent research has focused on the design and optimization of three-dimensional MGP nozzles, which offer even greater efficiency and thrust compared to two-dimensional designs (Abdelrahman et al., 2021). These nozzles require more complex geometries and manufacturing techniques, but have the potential to significantly improve the performance of solid rocket motors (Choi & Lee, 2020; Du et al., 2021; Sasaki et al., 2017).

The large review proposed above leads us to conclude that each type of propulsion nozzle has its own advantages and disadvantages, and that the choice of the right configuration depends in fact on the specific application and design requirements.

2.5.4. Performance parameters of C-D nozzles

The efficiency of a nozzle depends partially on the ambient (or atmospheric) pressure that depends on altitude (Marty, 1994). The pressure of the jet leaving the nozzle can therefore be lower, equal to or higher than the ambient pressure as represented in Figure 2.6. In most cases, the expansion process within a nozzle is well approximated by the isentropic approach. The main performance parameters may therefore be defined and expressed on the basis of the isentropic expansion process.

2.5.4.1. The thrust, T

The thrust of a propulsion nozzle represents the conversion of thermal energy originating from the combustion chamber into kinetic energy at the exit section. It is therefore expressed as a function of the mass of the gases ejected, their exit velocity and the pressure difference between that of the gases and the ambient (Figure 2.20):

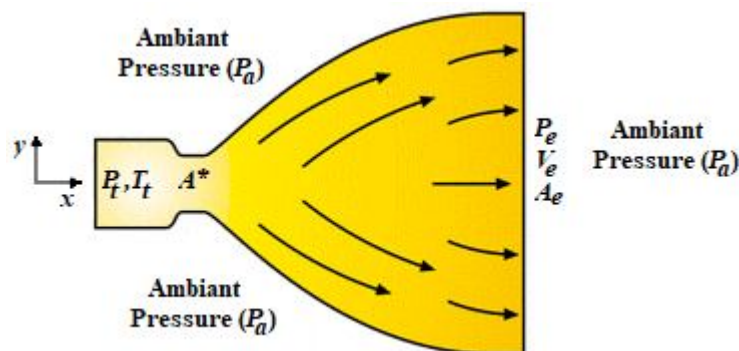$$T = \dot{m}V_e + \left(P_e - P_a\right)A_e \qquad (2.112)$$

Figure 2.20: Schematic of a C-D propulsion nozzle

Since velocity and pressure are generally not constant along the exit section, an application of the momentum conservation equation would express the infinitesimal thrust developed through an annular section of thickness (dy) as:

$$dT = \left[\rho V_e^2 + \left(P_e - P_a \right) \right] 2\pi\, y dy \tag{2.113}$$

The integration of the above equation along the exit section of the nozzle leads to the relationship that expresses the total thrust:

$$T = \pi \sum_i \left[\rho_i V_{si}^2 + \left(P_{si} - P_a \right) \right] \left(y_s^{i+1} - y_s^i \right)^2 \tag{2.114}$$

2.5.4.2. The effective velocity, V_{eff}

An interesting parameter can be expressed by dividing the thrust (what we wish to obtain) by the mass flow rate (what we have to 'pay' as in fact, it expresses the fuel consumption). The effective velocity is therefore expressed as:

$$V_{eff} = \frac{T}{\dot{m}} \tag{2.115}$$

2.5.4.3. The specific impulse, I_{sp}

The 'specific impulse' can be derived from the effective velocity. If the thrust and the mass flow rate are assumed to be independent, it comes:

$$V_{eff} = \frac{T}{\dot{m}} = \frac{\int T \cdot dt}{\int \dot{m} \cdot dt} = \frac{I}{M_{fuel}}$$

The above relationship expresses the total impulse obtained from a unit mass of fuel. This would introduce the specific impulse:

$$I_{sp} = \frac{V_{eff}}{g} = \frac{T}{\dot{m}g} \tag{2.116}$$

Table 2.2: Typical values of (*Isp*) for various propulsion types (Sutton & Biblarz, 2016).

Technology	I_{sp} (s)	Ejection velocity (m/s)
Nuclear fusion	10.000 – 50.000+	98.000 – 490.000+
Electric propulsion	1.000 – 10.000	9800 – 98.000
Nuclear (thermal) fission	600 – 1000	5900 - 9800
Thermal beam (microwave/laser)	600 – 1000	5900 - 9800
Bi-propellant chemical propulsion	200 - 500	2000 - 4900
Mono-propellant chemical propulsion	100 - 250	980 - 2450
Cold gas propulsion	10 – 120	100 - 1150

The specific impulse is expressed in seconds i.e. for an engine with $I_{sp} = 50$ seconds, a unit mass of fuel will generate a thrust capable of supporting its weight (of gravity g) for 50 seconds. This means a unit mass of fuel will support 50 times the weight of the vehicle for 01 second. Commonly referred to as 'gas mileage' relating to an engine, the specific impulse is generally used

to compare the performance of fuels used for propulsion. Table 2.2 presents how the specific impulse differs in various propulsion types.

2.5.4.4. The characteristic velocity, c^*

The characteristic velocity noted (c^*) is defined as the ratio of the product of the total pressure and the section at throat to the mass flow rate, i.e.:

$$c^* = \frac{P_t A^*}{\dot{m}} \tag{2.117}$$

By expressing the mass flow rate at the throat of a choked nozzle (i.e. $M = 1$ at throat) and remembering the isentropic relationships developed above (§ 2.4.3 and 2.4.5), it comes:

$$\dot{m} = \rho^* a^* A^* = \rho_t \left(\frac{\rho^*}{\rho_t}\right) a_t \left(\frac{a^*}{a_t}\right) A^* = \frac{P_t A^*}{\sqrt{\dfrac{R_G T_t}{\gamma}}} \left(\frac{\gamma+1}{2}\right)^{\frac{2(\gamma-1)}{\gamma+1}} \tag{2.118}$$

Equation 2.118 allows expressing the characteristic velocity as a function of the throat section (A^*), the properties of the ideal gases (R_G) and the total or stagnation conditions within the combustion chamber i.e. (P_t) and (T_t):

$$c^* = \frac{P_t A^*}{\dot{m}} = \sqrt{\frac{R_G T_t}{\gamma}} \left(\frac{\gamma+1}{2}\right)^{\frac{\gamma+1}{2(\gamma-1)}} \tag{2.119}$$

The interest in the characteristic velocity lies on the fact that all the parameters expressing it may be easily computed or measured.

2.5.4.5. The thrust coefficient, C_T

A comparison of the last three parameters represented by the effective speed (V_{eff}), the specific impulse (I_{sp}) and the characteristic velocity (c^*) shows that they are closely linked to each other. Indeed, we can write:

$$c^* = \frac{P_t A^*}{\dot{m}} \approx \frac{T}{\dot{m}} = V_{eff} = g\, I_{sp}$$

This relationship is better represented by the dimensionless performance parameter called thrust coefficient and noted (C_T) which can be defined as 'the thrust produced by a nozzle having a total pressure within its combustion chamber (P_t) and a useful fluid section represented by the section at the throat of its choked nozzle (A^*). This leads to:

$$C_T = \frac{T}{P_t A^*} \tag{2.120}$$

The thrust coefficient may be applied to identify how efficiently the nozzle generates thrust from the total pressure of its combustion chamber. It is therefore a characteristic parameter of the gas expansion in the divergent section of the nozzle, and can therefore be considered as particularly

representative of the performance of the contour of the supersonic divergent section. For an isentropic flow, it can be shown that the thrust coefficient may be expressed as:

$$C_T = \frac{\left(\dfrac{\gamma+1}{2}\right)^{\frac{\gamma+1}{-2(\gamma-1)}}}{M_e\sqrt{1+\dfrac{\gamma-1}{2}M_e^2}}\left(\gamma M_e^2 + 1 - \frac{P_a}{P_e}\right) \tag{2.121}$$

2.5.4.5. The Nozzle efficiency: Discharge coefficient (C_d) and efficiency (η)

Mainly due to friction, the 'true' performance of a nozzle is generally 'slightly' different from that determined assuming the expansion to be isentropic. This introduces the discharge coefficient (C_d) defined as the ratio of the real mass flow rate to the isentropic one:

$$C_d = \frac{\dot{m}_{\text{real}}}{\dot{m}_{\text{isentropic}}} \tag{2.122}$$

As far as the motor is concerned, and since the most important losses are generally associated with the combustion process within the combustion chamber, non-ideal performance is measured more easily and directly in terms of the characteristic velocity ($c*$). Therefore, efficiency (η_c*) may be defined as:

$$\eta_{c*} = \frac{c_{\text{measured}}^*}{c_{\text{ideal}}^*} = \frac{P_t\,A^*}{\dot{m}_p\,c_{\text{ideal}}^*} \tag{2.122}$$

with: $$c_{\text{ideal}}^* = \sqrt{\frac{R_G T_t}{\gamma}}\left(\frac{\gamma+1}{2}\right)^{\frac{\gamma+1}{2(\gamma-1)}} \tag{2.123}$$

2.6. The Method of Characteristics (MoC)

2.6.1. General

Numerical simulation is nowadays a powerful tool capable of reaching viable solutions to numerous scientific and technical problems. It plays almost an equal role in certain aspects of both fundamental research and engineering applications. The numerical methods, along with the development of mathematical theories and computer hardware, have been developed to the extent of reaching solutions to various complex issues that analytical approaches failed to achieve. Two numerical methods are applied in the present study. The first method concerns the so-called method of characteristics which is a procedure that applies a finite difference approach (FDM) to design supersonic propulsion nozzles. It solves the partial differential equations of hyperbolic form which describe a supersonic flow-field distinguished by its directions of propagation represented by the Mach lines. The dependent variables, along these characteristic directions, have to satisfy an equation known as the compatibility equation.

The second approach, known as the finite volume method (FVM), is one of the most commonly used in numerical analysis. Originally developed to solve solid mechanics problems, it has since found wide applications in almost all fields of engineering as well as in Computational Fluid Dynamics (CFD). Its basic concept may be described as the division of the computational domain

into small individual volumes (finite volumes), and the search for local solutions that satisfy the differential equations within these volumes. By putting the individual solutions together, an overall solution can be obtained.

2.6.2. The method of characteristics in inviscid flow computation

The method of characteristics has a rich history and has evolved over the years. Its roots may be found in the work of prominent mathematicians like Cauchy (1842) and Kowalevski (1875) in the 19th century who made foundational contributions to the method's development. Initially, the method of characteristics was applied to wave equations in physics and engineering, where it was used to describe the behavior of waves and solve problems related to wave propagation. It was only in the 20th century that it found extensive use in fluid dynamics, especially for solving problems related to compressible flows. It was and is still commonly applied to analyze supersonic and hypersonic flows, including the design of nozzles and shock waves. The central idea of the method is to transform a partial differential equation into a system of ordinary differential equations along curves known as characteristics. These characteristic curves represent the paths along which information propagates in the domain. In a supersonic or hypersonic flow, they are represented by the Mach lines. Nowadays, modern CFD software packages incorporate the method of characteristics as one of the numerical techniques for solving hyperbolic PDEs.

Due to the arduous nature of the solution presented, the issue of rocket nozzles optimum contours was ignored until a reformulation of the problem based on a simplified solution was suggested by Rao (1958). Direct optimization methods have later been developed and shown to achieve contours, specified as second-order polynomials, that lead to maximum thrust nozzle profiles (Allman & Hoffman, 1981) comparable to those of Rao (1958). Under zero pressure gradients, both methods were found to predict basically the same maximum thrust (agreement, in this case, was within 0.2%) sustaining the application of the direct optimization approaches.

2.6.2.1. The governing, characteristic and compatibility equations

The equations governing a 2-D flow, assumed to be isentropic, inviscid and irrotational, that takes place within a supersonic nozzle is expressed as:

$$\left(u^2 - a^2\right)\frac{\partial u}{\partial x} + \left(v^2 - a^2\right)\frac{\partial v}{\partial y} + 2uv\frac{\partial u}{\partial y} - \delta\frac{a^2 v}{y} = 0 \tag{2.124}$$

$$\frac{\partial u}{\partial y} - \frac{\partial v}{\partial x} = 0 \tag{2.125}$$

$$a = a(u, v) \tag{2.126}$$

The characteristic equation is initially obtained by multiplying equations 2.124 and 2.125 by the two unknowns (σ_1) and (σ_2), and summing. This leads to:

$$\sigma_1\left(a^2 - u^2\right)\left[\frac{\partial u}{\partial x} + \frac{\sigma_1(-2uv) - \sigma_2}{\sigma_1\left(a^2 - u^2\right)}\frac{\partial u}{\partial y}\right] + \sigma_2\left[\frac{\partial v}{\partial x} + \frac{\sigma_1\left(a^2 - v^2\right)}{\sigma_2}\frac{\partial v}{\partial y}\right] + \sigma_1\frac{\delta a v^2}{y} = 0 \tag{2.127}$$

The Assumption that the components of the velocity vector $u(x, y)$ and $v(x, y)$ are continuous functions allows writing:

$$\frac{du}{dx} = \frac{\partial u}{\partial x} + \lambda \frac{\partial u}{\partial y} \quad ; \quad \frac{dv}{dx} = \frac{\partial v}{\partial x} + \lambda \frac{\partial v}{\partial y} \tag{2.128}$$

where: $\lambda = dy/dx$ represents the slope of the characteristic curves.

Using equations 2.127 and 2.128 leads to expressing (λ) as:

$$\lambda = \frac{\sigma_1(2uv) + \sigma_2}{(u^2 - a^2)\sigma_1} \quad ; \quad \lambda = \frac{\sigma_1(v^2 - a^2)}{-\sigma_2} \tag{2.129}$$

that can be rewritten as:

$$\begin{cases} \sigma_1\{(u^2 - a^2)\lambda - 2uv\} + \sigma_2(-1) = 0 \\ \sigma_1(v^2 - a^2) + \sigma_2 \lambda = 0 \end{cases} \tag{2.130}$$

For this system to have a solution other than the trivial one, the determinant of the matrix formed by the coefficients must vanish. It comes:

$$\begin{vmatrix} (u^2 - a^2)\lambda - 2\,uv & -1 \\ v^2 - a^2 & \lambda \end{vmatrix} = 0 = (u^2 - a^2)\lambda^2 - 2\,uv\,\lambda + (v^2 - a^2) = 0 \tag{2.131}$$

leading to the solution:

$$\lambda_\pm = \left.\frac{\partial y}{\partial x}\right|_\pm = \frac{uv \pm a^2\sqrt{M^2 - 1}}{u^2 - a^2} \tag{2.132}$$

Equation 2.132 defines two curves in the (x, y) plane. They are known as the characteristics. They are real if the flow is supersonic (i.e. $M \succ 1$). Another form of this equation that is easier to apply may be derived through involving such parameters as the Mach number, the velocity magnitude $\left(V = \sqrt{u^2 + v^2}\right)$, the angle representing the direction of the flow (θ) and the Mach angle (α). Figure 2.21 represents these parameters.

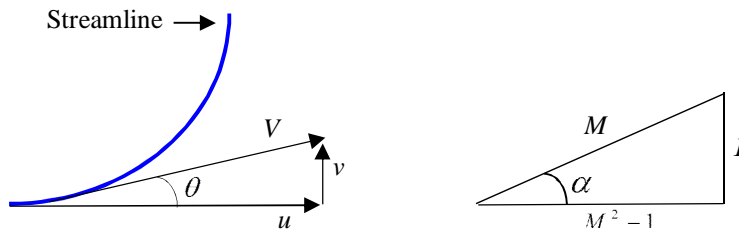**Figure 2.21:** representation of the flow direction and Mach angle

On the basis of Figure 2.21, one may write:

$$u = V \cos(\theta) \quad ; \quad v = V \sin(\theta) \quad ; \quad \theta = tg^{-1}\left(\frac{v}{u}\right) \tag{2.133}$$

$$\alpha = \frac{1}{\sin\left(\frac{1}{M}\right)} \quad ; \quad M = \frac{V}{a} = \frac{1}{\sin(\alpha)} \quad ; \quad \sqrt{M^2 - 1} = \cot g(\alpha) \tag{2.134}$$

Substituting equations 2.133 and 2.134 into equation 2.132 leads to the final expression of the characteristic equation:

$$\lambda_{\pm} = \left.\frac{dy}{dx}\right|_{\pm} = tg(\theta \pm \alpha) \tag{2.135}$$

Equation 2.135 is illustrated in Figure 2.22 where the right-running and left-running characteristics are represented by (C_+) and (C_-) respectively.
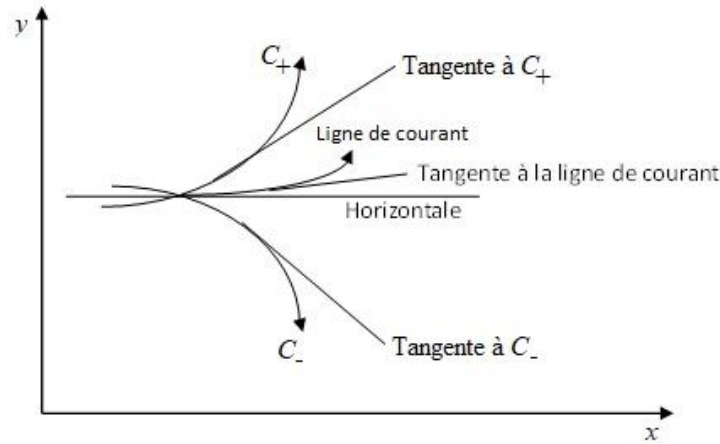
Figure 2.22: Right-running and left-running characteristics in a steady, 2-D irrotational flow

The compatibility equation may be obtained by first substituting equations 2.128 and 2.129 into equation 2.127, then multiplying by (dx). This leads to:

$$\sigma_1\left(u^2 - a^2\right)du - \sigma_2 \, dv - \sigma_1 \frac{\delta \, a^2 v}{y} dx = 0 \tag{2.136}$$

Equation 2.136 represents the compatibility equation for the system of equations 2.124 and 2.125. This equation is only valid if (λ) is expressed by equation 2.135. It therefore remains to determine the unknowns (σ_1) and (σ_2), and this is performed through solving the system of equations 2.130. The compatibility equation is finally obtained:

$$\left(u^2 - a^2\right)du_{\pm} + \left[-\left(u^2 - a^2\right)\lambda_{\pm} + 2uv\right]dv_{\pm} - \left(\delta\frac{a^2 v}{y}\right)dx_{\pm} = 0 \tag{2.137}$$

The compatibility equation 2.137 provides two differential equations (one through the right-running characteristic C_+ and the other through the left-running characteristic C_-). It relates the velocity components (u) and (v), and is only valid along the characteristics defined by the characteristic equation 2.135.

2.6.2.2. Application of the FDM to the solution of characteristic and compatibility equations

The application of the method of characteristics led to replacing the partial differential equations describing the supersonic flow (i.e. equations 2.124 and 2.125) by two total differential equations (i.e. the characteristic equation 2.135 and the compatibility equation 2.137). The solution of such a system of equations is carried out through the application of the well-known finite difference method (Zucrow & Hoffman, 1977).

The nodes constituting the mesh represent the points where the right-running characteristics cross their corresponding left-running ones (Figure 2.23). The finite difference equations corresponding to equations (2.135) and (2.137) are obtained by 'replacing' the differentials by finite differences Δx, Δy, Δu and Δv. Therefore:

$$
\begin{cases}
(a) & \Delta y_{\pm} = \lambda_{\pm}\Delta x_{\pm} \\
(b) & Q_{\pm}\Delta u_{\pm} + R_{\pm}\Delta v_{\pm} - S_{\pm}\Delta x_{\pm} = 0 \\
(c) & \lambda_{\pm} = tg(\theta \pm \alpha) \\
(d) & Q = u^2 - a^2 \\
(e) & R = 2uv - \left(u^2 - a^2\right)\lambda \\
(f) & S = \delta \dfrac{a^2 v}{y}
\end{cases}
\tag{2.138}
$$
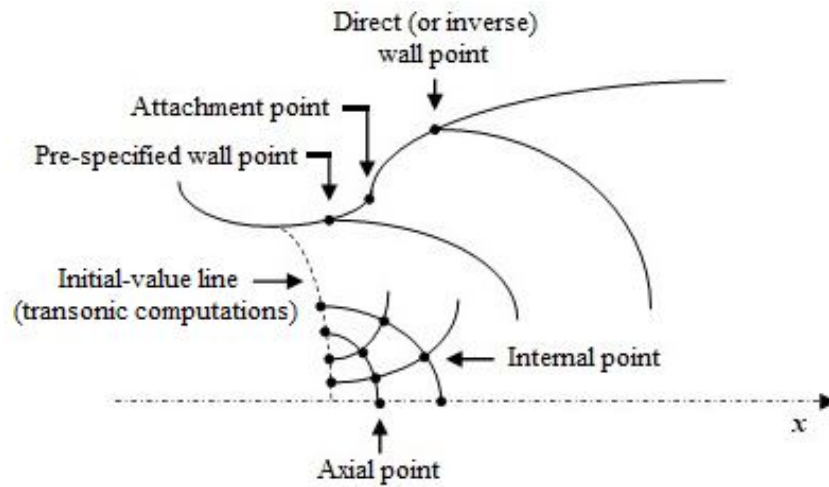
Figure 2.23: Diverse nodes constituting the mesh in the MoC

The mesh is essentially constituted by three types of nodes: (1) the internal nodes located inside the flow, (2) the axial nodes located on the axis of symmetry, and (3) the wall nodes that may be divided into two categories: those located downstream on the throat and before the attachment point (these are pre-specified points obeying to the fact that the supersonic expansion is higher in this region) and those located on the portion downstream of the attachment point.

The implementation of the MoC differs depending on the particular type of node. The solution applies a modified Euler predictor-corrector algorithm based on the average property method (Haddad, 1988).

2.7. Asymmetric nozzle concept

2.7.1. General

Asymmetric propulsion nozzles are a type of engine nozzle design used in aerospace applications where the geometry of the nozzle is intentionally altered in a non-uniform or asymmetric manner. Unlike traditional symmetric nozzles, which have uniform shapes, asymmetric nozzles feature variations in their geometry that can lead to improved performance, maneuverability, or other specific characteristics. The asymmetry in these nozzles can take various forms, such as variations in the throat area, divergent section shape, or the introduction of additional features like ramps, wedges, or secondary flow paths. The primary purpose of these modifications is to tailor the flow expansion and pressure distribution to achieve specific aerodynamic effects or performance benefits.

Reaching profiles where the installed system did not generate too much thrust loss or drag constituted the central concern in designing jet engine exhaust nozzles during the 60's and early 70's. The axisymmetric configurations exhibit high internal performances but with thrust penalties and low drag. They, however, show low thrust-minus-drag efficiency when integrated to complex propulsion engines having non-symmetric area constraints that increasingly require careful airframe/propulsion system integration (Laughrey et al., 1981). The advent of hypersonic air-breathing propulsion systems which operate at speeds greater than Mach 5 and provides specific impulses superior to that made available by rocket engines drove the interest for the design of asymmetric nozzles (Yunpeng & Zonglin, 2021; Gu & Li, 2020; Du et al., 2021). Furthermore, non-axisymmetric supersonic nozzles are becoming an important part of air-breathing hypersonic vehicles as they provide excellent integrated aerodynamic performances (Zhu et al., 2018). Moreover, they appear to be much better integrated to propulsion engines having non-symmetric area constraints leading to an enhancement of their performance.

The problems associated with the design of asymmetric plane nozzles optimum contours have been considered (Rylov, 1976; Rylov, 1977). In this case, i.e. for short lengths, the problem was solved using the so-called controlled contour method. It has been shown that the substitution of the centered wave by a compression wave of very moderate intensity significantly reduces the thrust of the nozzle. Yang et al. (2021) investigated the effect of nozzle asymmetry on the aerodynamic heating of a hypersonic vehicle while Thangaraj & Kaushik (2023) examined the impact of two non-circular nozzle exit shapes (elliptic and square) on the mixing augmenting efficacy at subsonic and sonic flow conditions. It was found that the elliptic nozzle was superior in terms of shortening the potential core length. It achieved a maximum core length reduction of 18.75% with quick jet decay.

Due to the applications of hypersonic vehicles, nozzles must be designed to fly at a lower altitude than conventional nozzles. This implies that both the size and form of the nozzle need to be adjusted to accommodate these conditions. (Vianna Moizes et al. 2023) examined various nozzle designs with the objective of increasing thrust while minimizing surface area and, consequently, nozzle production cost. Maneuverability and efficiency of supersonic and hypersonic aircrafts have also led to an interest in asymmetric nozzle configurations. Casper (2019) conducted a study on the design of an asymmetric supersonic nozzle for enhanced thrust vectoring. It was found that the asymmetric design would lead to a 20% increase in nozzle performance compared to a symmetric

design. A numerical investigation carried out on asymmetric nozzles designed for scramjet propulsion by Matveev & Semenov (2021) revealed the asymmetric configurations providing a significant increase in thrust compared to a symmetric design while also reducing the size and weight of the nozzle. Pal & Chattopadhyay (2018) conducted a design optimization study on an asymmetric supersonic nozzle. They found out that the optimized asymmetric design provided better thrust and pressure recovery compared to a symmetric nozzle. Overall, asymmetric nozzles are becoming an important part of air-breathing hypersonic vehicles as they provide excellent integrated aerodynamic performances particularly in terms of thrust and fuel efficiency (Zhu et al., 2018).

2.7.2. Elliptic nozzle

Elliptical propulsion nozzles are valuable components in aerospace engineering. They play a critical role in the performance and functionality of various aerospace vehicles, and moreover offer various advantages in terms of precise control and maneuverability (Bajpai & Rathakrishnan, 2018). They, for example, can provide higher levels of thrust vectoring efficiency compared to some other designs mainly by altering the flow of exhaust gases through the elliptical shape. They can also help manage shock waves generated by supersonic or hypersonic flows more effectively resulting in reduced flow separation and losses. In terms of supersonic combustion, elliptical nozzles can enhance its efficiency by maintaining a stable and efficient supersonic combustion and providing better expansion of combustion gases needed in air-breathing engines like scramjets. Finally, the elliptical nozzle shape can be tailored to specific flight conditions leading to efficient performance across a range of mission requirements. Figure 2.24 shows an elliptical C-D nozzle with an aspect ratio of 2:1 (Kumar & Rathakrishnan, 2016).

-a-   -b-
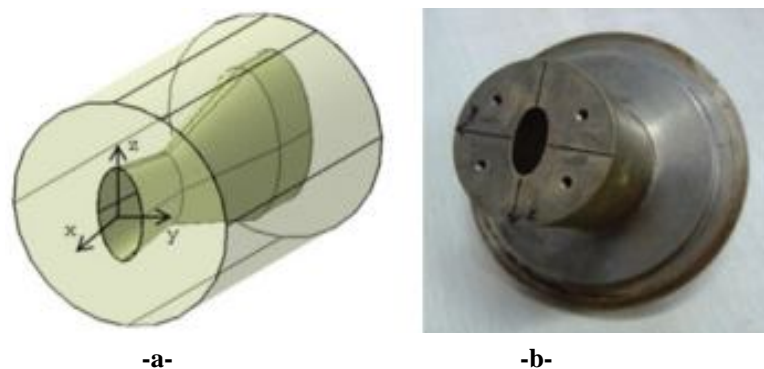
Figure 2.24: Elliptical C-D nozzle (Kumar & Rathakrishnan, 2016)
a) A view of the exit cross-section (AR=2:1), b) A photographic view of the exit cross-section

The applications of elliptical propulsion nozzles are diverse and extend to various types of vehicles operating at different speed regimes and altitudes. Scramjet engines, operating at high speeds in the atmosphere, can benefit from the optimized expansion characteristics of elliptical nozzles that would lead to improving their combustion efficiency and thrust. The thrust vectoring capability of elliptical nozzles may be found in diverse drones designed for agile maneuvers, reconnaissance, and surveillance. Stealth Aircraft that need reduced radar cross-section can benefit from elliptical nozzles that are capable of minimizing their detectability by radar systems.

2.7.3. Corrugated lobed nozzle

Several unconventional nozzle designs have been shown to have significant acoustic advantages. Nozzles erected for a specified Mach number at exit produce less jet noise than axisymmetric (circular) nozzles with a supersonic rectangular or elliptic cross section (Gilinsky et al., 2004). The importance of corrugated nozzles lies in their potential to address various challenges in propulsion systems, such as noise reduction and flow control. However, the design and implementation of such nozzles can be complex as they feature a wavy or corrugated geometry along their length, requiring a thorough understanding of fluid dynamics, thermodynamics, and propulsion principles. Despite the existence of several strong and mild shock waves, the experimental study carried out by Ahuja (1993) and Krothapalli et al. (1993) demonstrated the effectiveness of such configurations in lowering jet noise (including screech tones).

Figure 2.25 shows a known as "coanda exhaust" that has been designed and manufactured in the 1950s and 1960s, with the idea of using the coanda effect (a phenomenon where a fluid flow tends to stay attached to a curved surface to help improve the overall efficiency of the engine by directing the exhaust gases in a specific way. Due to some shortcomings, this design was later replaced by more traditional exhaust nozzle designs.

Figure 2.25: Rolls Royce Conway Mk508 (1959) used in Boeing 707-420

Three corrugated lobed nozzles are represented in Figure 2.26. The study carried out by Roy et al., (2022) aims at investigating the influence of both lobe number and length of corrugated lobed nozzles on diverse characteristics of subsonic jets.

Figure 2.26: Corrugated lobed nozzles with 10mm, 15mm and 20mm lobe lengths (Roy et al., 2022)

The ability of corrugated nozzles to enhance thrust efficiency, pressure recovery, and flow characteristics makes their applications span over a wide range of aerospace systems. In rocket engines, they may contribute to better overall propulsion performance through improving thrust efficiency and increasing pressure recovery while in scramjet engines, corrugated nozzles can enhance the combustion efficiency and thrust generation by promoting better mixing of air and fuel. In jet engines, corrugated nozzles can reduce noise levels.

2.7.4. Design approach for asymmetric nozzles

In terms of design approach development, early procedures used graphical characteristic designs as the basis for drafting asymmetric nozzles. These approaches lacked the necessary precision required for getting the flow uniformity needed in wind tunnels. A design procedure for the design of asymmetric nozzles that was based on an iterative process and able to support both a wide range of Mach numbers and flow uniformities was later proposed by Liepman (1953). The procedure was solely applicable for perfect flows thus neglecting the boundary later effects. Indeed and at the time of this report, the aerospace community was convinced that for Mach numbers below 3 nozzle profiles did no need boundary layer corrections. The problem with the above-mentioned method is that it is tedious with no guarantee of reaching noteworthy results i.e. a nozzle profile ensuring exit flow uniformity and able to operate at the desired Mach numbers. By looking at the minimal design requirements needed for an asymmetric nozzle and then satisfying them in terms of form, angle, and length parameters, Winarto & Stalker (1984) developed a method for choosing nozzle profiles for a given nozzle criteria in a "sliding block" asymmetric wind tunnel. They applied the MoC and assumed the flow to be inviscid.

Mo et al. (2014) presented a method for optimizing the shape of an asymmetric scramjet nozzle that incorporates a transition from a circular throat to a square cross-section shape at the exit. The objective was to improve airframe integration. The streamline tracing technique was applied along with the MoC to generate the needed geometry. The obtained CFD results on flow static pressures on the upper and lower walls of the asymmetric nozzle were validated against the measurement data leading the authors to conclude that the proposed method is convenient and accurate for the design of circular to rectangular shape transition scramjet nozzles. The same technique i.e., streamline tracing has been applied and shown to produce good results (Haddad & Moss, 1990).

Chapitre3:

APPLICATION OF THE METHOD OF CHARACTERISTICS TO THE DESIGN OF THE INITIAL AXISYMMETRIC NOZZLES

3.1. General

The present section will focus on the design procedure of two axisymmetric C-D nozzles. The first one is calculated in order to be transformed into a Truncated Ideal Contour (TIC) nozzle, while the second is computed in detail in order to be transformed into (1) an asymmetric nozzle of elliptical cross-section and (2) a corrugated lobbed nozzle using the procedure described in section 5. The axisymmetric-to-be-truncated nozzle will have its divergent section computed using the method of characteristics, its convergent section being designed using the Rao method (Uyeki, 2018). The axisymmetric-for-elliptic section has its divergent section computed using the method of characteristics. An elliptic supersonic propulsion nozzle having been manufactured, submitted to experimental testing and the results being available, the model must evidently fit the available design (Haddad & Moss, 1990). The results obtained are compared to the available experimental results.

3.2. The Ideal Contour axisymmetric-to-be-truncated nozzle design (IC nozzle)

The ideal axisymmetric-to-be-truncated configuration is a contoured nozzle (Figure 3.1). Its design is carried out by the method of characteristics (c.f. section 2.6) that has been integrated into an in-house developed program using the Fortran language (Haddad, 2000). The ideal nozzle is truncated and the flow-field within the TIC configuration generated is simulated under the Ansys-Fluent platform (Ansys, 2022). The profile and the results achieved are compared to the profile and performance parameters obtained by a similar application (Hamitouche & Djebbar, 2015).
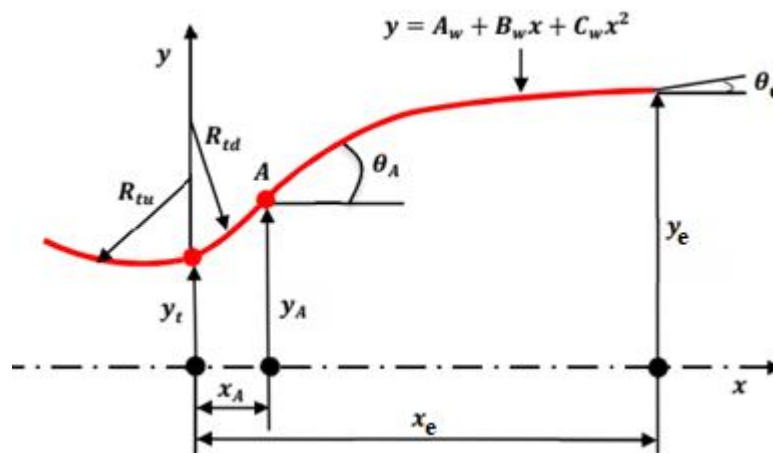

Figure 3.1: Supersonic section of the contoured nozzle

3.2.1. The ideal contour (IC) nozzle profile

The input thermodynamic and geometric data necessary to launching the computations using the MoC are essentially represented by the parameters representing the total or stagnation state of the flow i.e. P_t and T_t in the combustion chamber located upstream of the converging section, and those describing the profile of the nozzle i.e. the radii of curvature upstream of the throat R_{tu} and downstream of the throat R_{td}, the throat radius y_t, the length of the divergent x_e, and the deflection angles at both the attachment and exit-lip points θ_A and θ_e (cf. Figure 3.1 and Table 3.1).

Table 3.1: Input thermodynamic and geometric properties for MoC computations (Hamitouche & Djebbar, 2015)

Thermodynamic properties	Geometric properties
P_a = 1.013 *bars*	y_t = 0.01 *m*
P_t = 30 *bars*	R_{tu} = 0.03 *m*
T_t = 330 *K*	R_{td} = 0.03 *m*
γ = 1.4	θ_A = 15°
R_G = 280 *J/Kg.K*	θ_A = 0°
	x_e= 0.109341 *m*

The application of the MoC to the contoured configuration shown in Figure 3.1 generated the nozzle profile and its defining parameters represented by the exit radius (y_t), the position of the attachment point (x_A,y_A) and wall contour polynomial coefficients (A_w, B_w and C_w). Table 3.2 presents the results obtained along with their comparison to those carried out on a similar nozzle (Hamitouche & Djebbar, 2015).

Table 3.2: Comparison in terms of profiles generated

Actual profile parameters	Profile parameters (Hamitouche & Djebbar, 2015)
x_A=0.00776 *m*	x_A=0.007764 *m*
y_A=0.01102 *m*	y_A=0.011022 *m*
A_w=0.00886	A_w=0.00885
B_w=0.28843	B_w=0.29115
C_w= -1.31895	C_w= -1.5646
y_e=0.02463 *m*	y_e=0.022919 *m*

The nozzle supersonic section profile obtained through the application of the MoC is represented in Figure 3.2 along with the one obtained by Hamitouche & Djebbar (2015). The two profiles are found to be similar immediately downstream of the throat. Halfway of the divergent section i.e. at approximatively $x = 0.05$ m, they start 'taking off' from each other until the exit. The present profile seems to be more contoured, and this is mainly due to the difference in the coefficients describing the 2nd-order polynomial defining the bell-shaped nozzle.
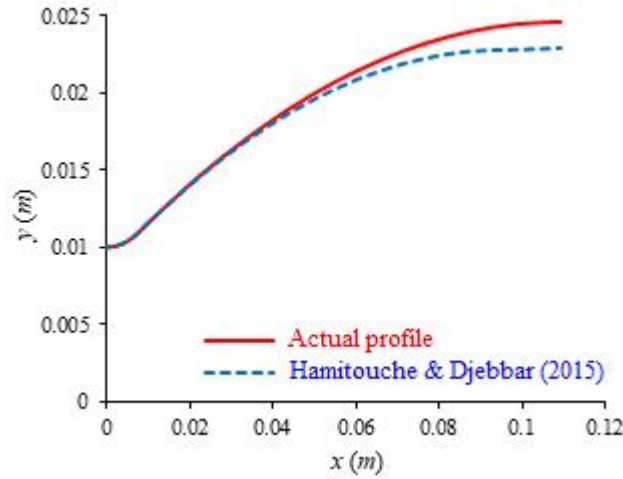
Figure 3.2: Ideal contour nozzle divergent sections

3.3. The ideal contour axisymmetric-for-elliptic-and-corrugated nozzle design

3.3.1. Axisymmetric design input parameters

For nozzles intended to equip wind tunnels, achieving a high level of exit flow uniformity is crucial and represents a primary design requirement. In the present case, the conditions are not as stringent, and while desirable, achieving perfect exit flow uniformity is not a critical factor. It is reasonable to assume that the circular-arc contours defining the throat will generate a sufficiently uniform flow. Moreover, the bell-shaped wall downstream of the attachment point will further align the flow resulting in acceptable conditions at the exit. However, Any attempt to design a contoured axisymmetric nozzle and hence analyze its flow-field using the MoC necessitates the establishment of specific initial parameters. However and given the intention, in order to validate the approach proposed, to compare the results obtained with the experimental results available in the specialized literature (Haddad & Moss, 1990), the stagnation pressure and temperature were taken equal to 14.8 atm. and 403K respectively. The objective of achieving a Mach number of 2.4 through a complete and isentropic flow expansion to ambient atmospheric pressure made possible by the pressure ratio of 14.8 led to the determination of the area ratio that has been found equal to 2.32 (Yahya, 2006).

In order to reach a supersonic flow in the nozzle's divergent section, the Mach number at the throat has to achieve unity and in this case, the choked mass flow rate can be accessed through applying the provided Equation 3.1. A this point and for the given mass flow set by the test facility's compressors when a specified pressure is required along with the stagnation pressure and temperature, the throat's radius (y_t) can be determined. A complete expansion will define the required area ratio and this in turn will lead to calculate the exit radius.

$$\dot{m} = \sqrt{\frac{\gamma}{R_G}\left(\frac{2}{\gamma+1}\right)^{\frac{\gamma+}{\gamma-1}}} \frac{P_t \pi y_t^2}{T_t^2} \tag{3.1}$$

A critical parameter that governs the isentropic flow characteristics within the transonic section of a C-D nozzle featuring a circular-arc throat is represented by the ratio R_{tu}/y_t. When this parameter significantly exceeds unity, signifying a gradual throat contour, the flow behaves primarily in a 1-D manner. However, as this ratio diminishes, 2-D flow effects start to become

significant. In cases where this parameter remains at or above approximately 2, the available 2-D flow theories effectively predict the transonic flow field (Cuffel et al., 1969; Haddad & Kbab, 2013). However, these theories do not hold for nozzles with tighter throats (where the parameter is less than 1), such as those encountered in certain rocket engines. It is on this basis that the values of 2 and 0.5 were adopted for the factors R_{tu}/y_t and R_{td}/y_t respectively.

As far as the maximum angle of divergence representing the contour angle at the attachment point (Figure 3.1) where the downstream circular-arc connects with the quadratic wall, a high value for this angle may lead to flow separation. A smaller angle however may not allow for the complete expansion of gases within the desired length, resulting in a longer nozzle and consequently a greater weight. In the present case and as a compromise, a contour angle of 15° was selected.

An overview of the input data for the axisymmetric configuration, which served as the basis for the subsequent development of the elliptic and corrugated nozzle designs, is displayed in Table 3.3.

Table 3.3: Input thermodynamic and geometric properties for axisymmetric-to-elliptic and axisymmetric to-corrugated nozzle configurations

Thermodynamic properties	Geometric properties
$P_a = 1.013.10^5$ Pa	$y_t = 0.020\ m$
$P_t = 15.10^5$ Pa	$R_{tu} = 0.040\ m$
$T_t = 403$ K	$R_{td} = 0.010\ m$
$\gamma = 1.4$	$\theta_A = 15°$
$R_G = 280\ J/Kg.K$	$\theta_A = 5°$
	$x_e = 0.060\ m$

3.3.2. Axisymmetric results

The input parameters (Table 3.3) were used to carry out the computations using the MoC that have been integrated into a home-developed program. The axisymmetric nozzle profile such as that represented in Figure 3.1, represented essentially by the attachment point coordinates (x_A, y_A), the coefficients of the 2nd-order polynomial contour (A_w, B_w, C_w) and the exit radius (y_e), was achieved through the application of application of the following relationships:

$$x_A = R_{td} \sin(\theta_A) \tag{3.2}$$

$$y_A = y_t + R_{td}\left[1 - \cos(\theta_A)\right] \tag{3.3}$$

$$y(x_A) = y_A = A_w + B_w x_A + C_w x_A^2 \tag{3.4}$$

$$\left(\frac{\partial y}{\partial x}\right)_{x_A} = tg(\theta_A) = B_w + 2C_w x_A \tag{3.5}$$

$$\left(\frac{\partial y}{\partial x}\right)_e = tg(\theta_e) = B_w + 2C_w x_e \tag{3.6}$$

The supersonic computations within the divergent section were carried out for a steady and inviscid flow-field. A starting line where the Mach number exceeds unity is necessary. Therefore, a transonic calculation approach was employed (Kliegel & Levine 1969).

The application of the MoC to the contoured axisymmetric-to-elliptic and axisymmetric to-corrugated nozzle configuration generated the nozzle profile and its defining parameters. Table 3.4 presents the results obtained in terms of the attachment point coordinates and the defining constants of the polynomial.

Table 3.4: Profile generated parameters

Profile parameters
$x_A = 0.00259\ m$
$y_A = 0.02034\ m$
$A_w = 0.01964$
$B_w = 0.27608$
$C_w = -1.57163$
$y_e = 0.03054\ m$

The Method of Characteristics (MoC) solution of the axisymmetric nozzle configuration is displayed in Figure 3.3. An abrupt expansion of the flow may be noticed near the throat corresponding to a sharp rise of the Mach number. Further downstream, a gradual straightening of both the pressure and Mach takes place and persists ultimately reaching a Mach number of 2.36 at the exit. At the attachment point, noted 'A' in Figure 3.3, a minor discontinuity is discerned, representing the connection between the downstream ac-of-circle and the wall simulated as a 2nd-order polynomial.
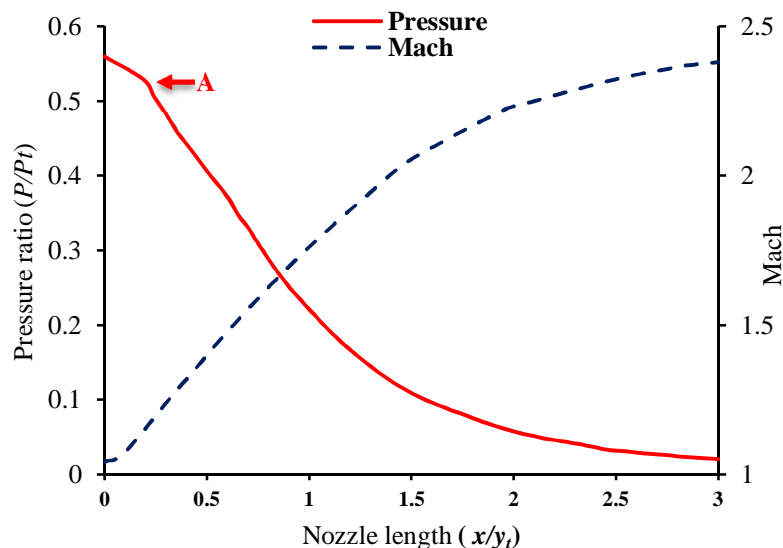

Figure 3.3: Static pressure and Mach distributions along centerline (MoC-Axisymmetric)

The pronounced expansion and the corresponding increase in the first portion of the divergent section are distinctive characteristics of bell-shaped profile nozzles. Within these configurations, the great majority of the expansion occurs right after the throat, the remaining

portion guiding the flow toward the axial direction and resulting in a shorter divergent section and an optimum thrust in that specific direction.

Table 3.5 displays the performance parameters of the axisymmetric nozzle designed by application of the MoC and intended to be transformed into an asymmetric configuration using the procedure developed.

Table 3.5: MoC-axisymmetric performance parameters (§2.5.4)

Performance parameters	
Thrust, T (N)	2470
Mass flow rate, $\dot{m}$ (kg/s)	2.8
I_{sp} (s)	89.9
V_{eff} (m/s)	882
Thrust coefficient, C_T (-)	1.31
M_{exit} (-)	2.36

The thrust coefficient essentially characterizes the performance of the supersonic contour in expanding the combustion gases and therefore producing thrust. It may be seen that the results obtained (in Table 3.4) shows a great control of the expansion process within the profile designed. The other factors shown will be used later to compare the present configuration with the symmetric one (cf. section 6).

3.3.4. Boundary layer correction

Considering the fact that the computations have been carried out for an inviscid flow, it would be more accurate to account for the viscosity. Therefore, the development of the boundary layer on the nozzle wall was computed in terms of the displacement thickness (Herring & Mellor, 1972). The outer flow conditions required for the viscous boundary layer were taken as the boundary conditions of the inviscid flow-field determined earlier using the MoC.
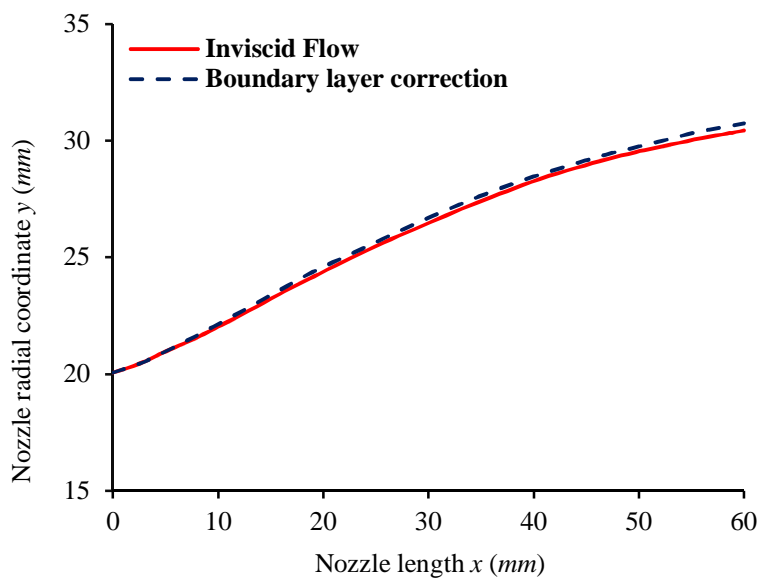

Figure 3.4: Boundary layer development (Axisymmetric nozzle)

Figure 3.4 displays the 'build-up' resulting from taking into account the boundary layer in terms of the displacement thickness expressed as the ratio of the displacement thickness (δ^*). The influence of the viscosity in terms of the normalized displacement thickness (i.e. δ^*/y) was found equal to 0.3%. Moreover, the blockage coefficient which represents the ratio of the inviscid flow area to the total viscous flow area reached a value of 0.99. These results led to consider appropriate to neglect the viscous effects on the axisymmetric designed configuration.

_____

Chapter 4:

THE TRUNCATED IDEAL CONTOUR (TIC) NOZZLE: PROCEDURE AND 2D CFD SIMULATION

4.1. General

The present section integrates the approaches applied to proceed with the truncation of the nozzle whose original profile has been designed in section 3.3. A CFD simulation of the flow-field is carried out within the Truncated Ideal Contour (TIC) nozzle, and the results obtained will be compared to those achieved through the application of the method of characteristics on the same TIC configuration.

4.2. The Truncated Ideal Contour (TIC) nozzle

The weight of the designed Ideal Contour (IC) configuration is too large to expect an interesting specific impulse from the motor this nozzle would integrate. A truncation is therefore necessary that would reduce the nozzle weight but at the same time does not alter too much its thrust. The flow divergence at the exit cross-section of the TIC nozzle will irremediably lead to a loss in the exit velocity in the axial direction that would be associated with a loss in thrust. Fortunately, though, the weight gain from the truncation would make up for the loss in thrust. The best compromise between weight and thrust losses has been found to correspond to a 20% truncation (Hamitouche & Djebbar, 2015).
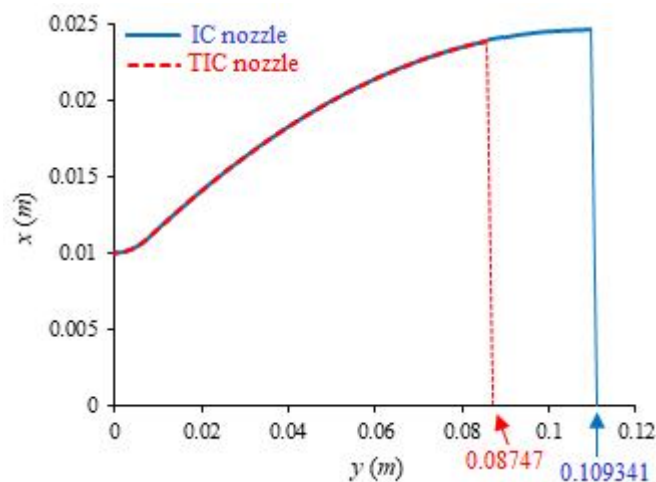

Figure 4.1: IC and TIC nozzles divergent sections

Maintaining the same geometrical and thermodynamic input parameters and applying the required truncation, as illustrated in Figure 4.1, the nozzle length will inevitably be reduced, and the exit angle of divergence will increase. Table 4.1 presents the shifting parameters of the two configurations.

Table 4.1: IC and TIC exit length and divergence angle

Nozzle configuration	x_e (m)	θ_e (°)	y_e (m)
IC nozzle	0.109341	0	0.02463
TIC nozzle	0.08747	3.3	0.02400

4.3. The TIC nozzle subsonic convergent section design

The subsonic convergent section main mission is to make the flow achieve a transonic velocity at the throat leading to a supersonic expansion in the divergent section. The subsonic section has been generated through the application of the so-called Rao technique (Uyeki, 2018). Attached to the upstream arc-of-circle of radius (R_{tu}), it constitutes the entire nozzle profile. The Rao's approach is the culmination of multiple experimental investigations. Based essentially on the throat radius (y_t), it enables a successful design of converging section profiles. The profile is generated through:

$$\begin{cases} x = 1,5 \ y_{col} \ \cos(\theta) \\ y = 1,5 \ y_{col} \ \sin(\theta) + 2,5 \ y_{col} \end{cases} \tag{4.1}$$

where: $-130° \leq \theta \leq -90°$

Table 4.2: Subsonic converging section profile

θ (°)	x (m)	y (m)
-90	0.	0.01
-95	-0.0013073361	0.0100570795
-100	-0.0026047227	0.0102278837
-105	-0.0038822857	0.0105111126
-110	-0.0051303021	0.0109046107
-115	-0.0063392739	0.0114053832
-120	-0.0075	0.0120096189
-125	-0.0086036465	0.0127127193
-130	-0.0096418141	0.0135093334

The authors' computations resulted in the design of the convergent section profile whose defining coordinates are depicted in Table 4.2. Figure 4.2 shows the resulting converging section.
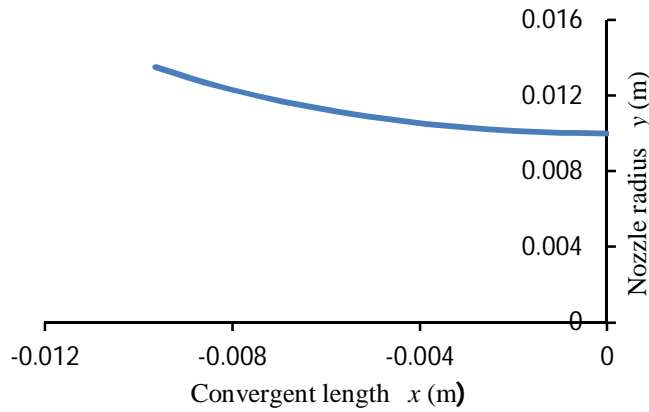
Figure 4.2: Profile of subsonic convergent section

4.4. The TIC nozzle CFD simulation

The compressible expansion within the TIC nozzle was simulated using a CFD solver based on the finite volume approach. A mesh comprising 12,500 elements, 250 in the axial direction (x) and 50 in the radial direction (y), was generated under 'Gambit 2.4.6'. In the vicinity of the throat, where property gradients are anticipated to be larger, as well as along the solid wall, where viscosity effects are noticeable, a more finely resolved mesh was used (Figure 4.3). The Ansys-Fluent platform was used to perform the computations until the ideal design conditions were met.
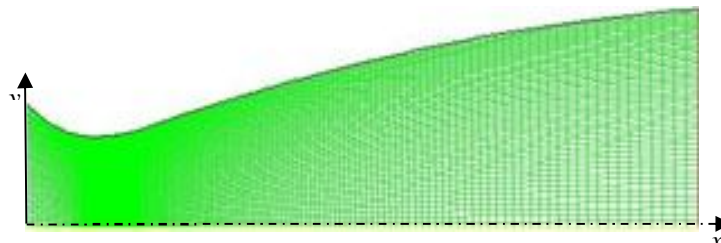

Figure 4.3: TIC nozzle grid topology

The governing equations include the physical laws pertaining to conservation of mass, momentum, and energy. The (k-ω) model was selected as the turbulence model. Table 5 summarizes the computational parameters applied in the simulation that led to obtaining the results shown in the tables and figures below. The equations representing the conservation of mass, momentum, and energy (section 2.2.2) are used as the governing equations for such a turbulent viscous flow-field. The closure of the system of equations is performed through the application of the k-ω model (section 2.3.5). The computational parameters applied for the simulation are outlined in Table 4.3.

Table 4.3: TIC nozzle simulation settings

	Applied features
Model	3D, Elliptic, stationary, viscous with compressibility effects
Solver	Density based
Turbulence model	k-ω
Fluid	air, ideal gas
Inlet Boundary Conditions	30.10^5 Pa / 330 K
Outlet Boundary Conditions	$1.013.10^5$ Pa
Residual	10^{-6}

4.5. Results and discussions

4.5.1. The Ideal Contour (IC) nozzle

The performance parameters of the ideal contour nozzle are determined using the relationships derived in Section 2.5.4. The results obtained are compared to those gathered by (Hamitouche & Djebbar, 2015) and displayed in Table 4.4. The results are found to be very close and the discrepancies are essentially due to the difference in profiles noticed in Figure 3.2.

In terms of the thrust coefficient, which measures the effectiveness of the expansion within the diverging supersonic section, the results are found to be close within 6%. The results achieved show the reliability and strength of the designed profile along with its efficiency in expanding the gases.

Table 4.4: IC nozzle performance comparison

Performance parameters	Present profile	Profile (Hamitouche & Djebbar, 2015)	Error (%)
Thrust, T (N)	1513.01	1433.39	5.2
Mass flow rate, $\dot{m}$ (kg/s)	2.013	2.013	0.0
Thrust coefficient, C_T (-)	1.61	1.52	5.5
Effective velocity, V_{eff} (m/s)	751.62	670.12	10.8
Mach at exit, M (-)	3.24	3.37	3.8
Specific impulse, I_s (s)	71.26	68.32	4.1

The static pressure and Mach number distributions along both the centerline and the wall are shown in Figures 4.4 and 4.5 respectively. In the vicinity and immediately downstream of the throat, an abrupt and large expansion may be observed that leads to a severe fall in pressure (Figure 4.4). This is accompanied by an immediate increase in Mach that may be noticed in Figure 4.5. This phenomenon is the result of the high attachment angle (θ_A) that may be seen in Figure 3.1. A straightening of the pressure profile follows that directs the accelerating gases towards the symmetry axis. The expansion becomes steadier therefore leading to a greater thrust in the axial direction.
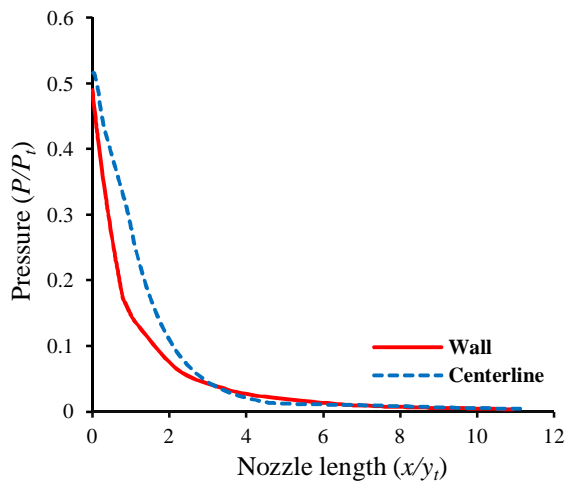

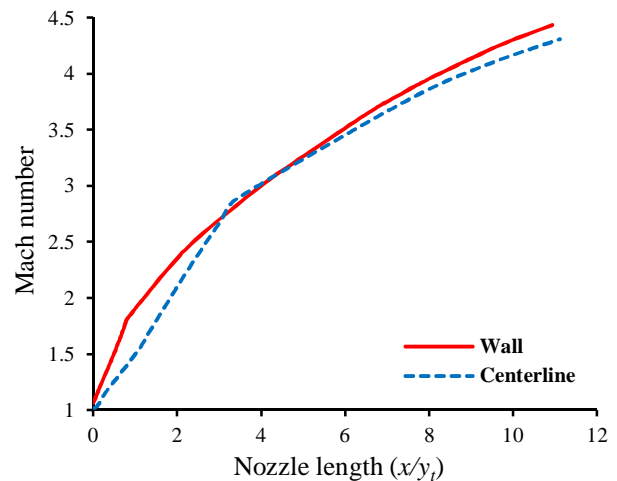**Figure 4.4:** IC nozzle-Divergent pressure distribution

Figure 4.5: IC nozzle-Divergent Mach distribution

4.5.2. The Truncated Ideal Contour (TIC) nozzle

4.5.2.1. TIC nozzle - MoC computations

The IC configuration being too long hence too heavy has been truncated (Figure 4.1), a 20% truncation has been found to be the best compromise weight and thrust losses (section 4.2). The MoC procedure is re-applied to simulate the supersonic flow-field within the TIC divergent section. The results obtained are illustrated in terms of the pressure distribution along the centerline and the wall (Figure 4.6).
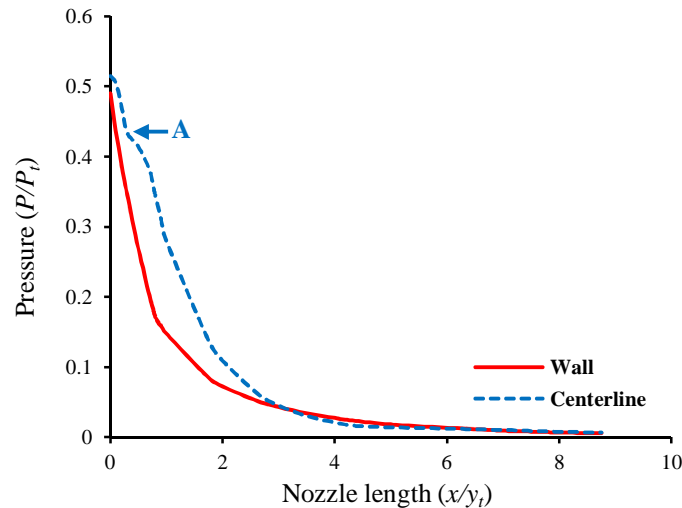

Figure 4.6: TIC nozzle-Pressure distribution

The above Figure 4.6 displays the pressure distribution along the divergent section of the TIC nozzle. This section may be divided into two parts: the immediate downstream vicinity of the throat i.e. before the attachment point A (cf. Figure 3.1) that has been simulated as an arc-of-circle of radius (R_{td}), and the contoured profile simulated as a quadratic polynomial wall. This division explains the expansion process that takes place in a contoured nozzle where it is sharper within the first section leading to a great acceleration of the gases, and slower but directed towards the axial direction within the second section. This is a central characteristic of the contoured nozzle that should result in a shorter configuration that develops the much needed higher thrust in the axial direction.

The expansion process along the centerline shows a discrepancy noted 'A' in Figure 4.6. It shows the true character of the simulation carried out by the MoC. Such a method carries out the computations along the characteristics which are, in the case of a supersonic expansion, represented by the Mach lines. This peculiarity does not appear within the pressure distribution along the wall as, within this position; the characteristics are usually mixed thus missing the discontinuity representation.

A comparison between the performance parameters of the two configurations (IC and TIC) has been carried out. The results are shown in Table 4.5 and demonstrate the closeness of the performance developed. It is obvious that the TIC configuration performs slightly less well than the IC one, but this is largely compensated by the reduction in mass of the TIC nozzle.

Table 4.5: IC and TIC nozzle performance comparison

Performance parameters	IC nozzle	TIC nozzle	Error (%)
Thrust, T (N)	1513.01	1333.2	11.8
Mass flow rate, $\dot{m}$ (kg/s)	2.013	2.013	0.0
Thrust coefficient, C_T (-)	1.61	1.41	5.9
Specific impulse, I_s (s)	71.267	62.44	4.3

4.5.2.2. TIC nozzle - CFD computations – Pressure and Mach contours

A CFD simulation was performed in order to visualize the flow behavior in the nozzle. The results obtained in terms of the static pressure and Mach number are shown in Figures 4.7 and 4.8. The pressure is found to be dropping uniformly from its stagnation value of 30 bars at the entry of the convergent to an average of 0.5 bars at the exit. This reduction in pressure may be seen to be greater immediately downstream of the throat, and stabilizing afterwards i.e. downstream of the attachment point within the divergent section. The discharge is found to be almost axial i.e. in the axial direction parallel to the centerline, thus producing a maximum thrust in that direction.
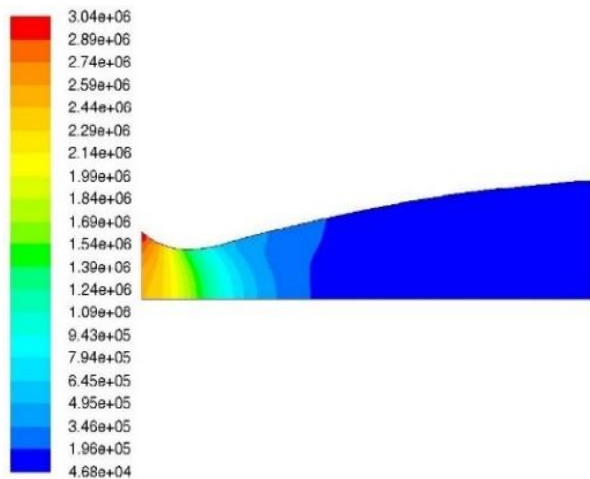
Figure 4.7: TIC nozzle – Pressure contour
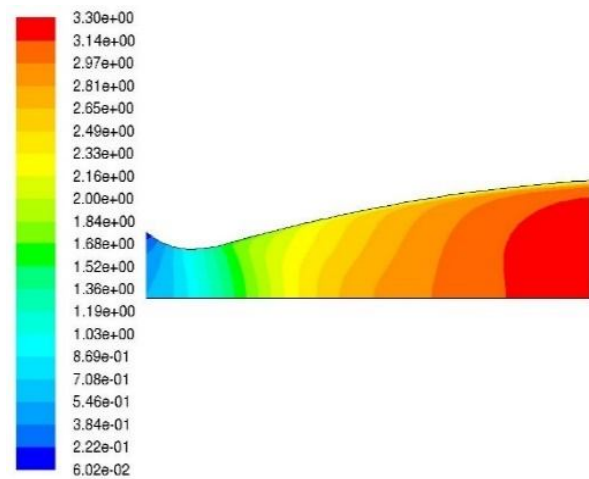
Figure 4.8: TIC nozzle – Mach contour

The Mach number contours along the various cross-sections of the TIC profile are shown in Figure 4.8. From the convergent entry to the exit section, the flow may be seen to be accelerating. The Mach number of unity at the throat led to a supersonic expansion within the diverging section. It may be seen that the Mach magnitude increases from $M = 0.08$ at the entry i.e. coming from the combustion chamber to an average $M = 3.3$ at the exit cross-section.

4.5.2.3. TIC nozzle - CFD computations – Pressure and Mach distributions

The results obtained from the MoC and FVM approaches are compared, and the outcome shown in Figure 4.9 for the pressure distribution along the centerline and Figure 4.10 for the pressure distribution along the wall. A good agreement between the two methods is observed. However and concerning the pressure distributions along the centerline (Figure 4.9), a slight difference may be observed in terms of the starting pressures (approximatively 0.6 and 0.5 in terms of P/P_t for the FVM and MoC computations respectively). This slight discrepancy is mainly due to

the fact that the MoC may solely handle supersonic flows (cf. section 2.6 and Appendix A) thus needing a starting sonic curve generally approached by a parabola at the throat whereas in the case of the FVM approach, the computations have been performed along the whole nozzle hence including the convergent, throat, and divergent sections.
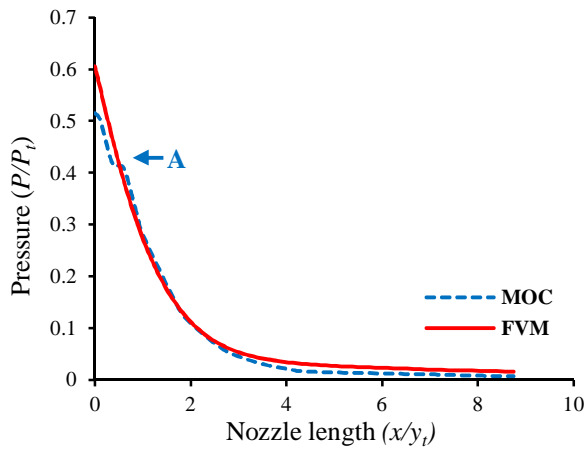

Figure 4.9: TIC nozzle - Pressure distribution along centerline
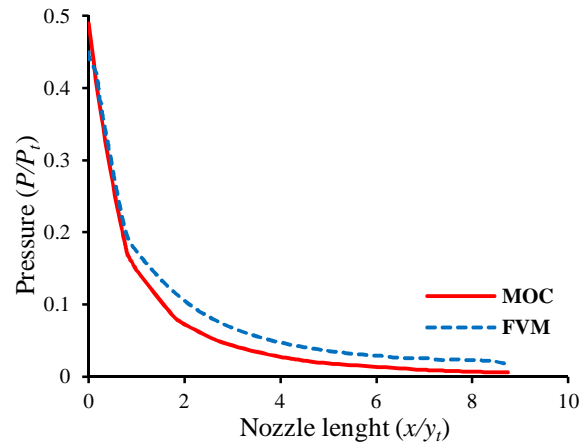

Figure 4.10: TIC nozzle – Pressure distribution along wall

As displayed in Figure 2.6, a point of discontinuity along the curve representing the distribution of in the pressure along the centerline computed using the MoC does also appear in Figure 4.9. It is designated 'A' and is solely shown in the MoC computations because these latter's are carried out along the characteristics (Mach lines in the present case of supersonic expansion) therefore showing the true character of the expansion. In the case of the FVM, it does not show up as the latter's procedure because of the smoothing out of its results by the interpolations performed throughout those computations.

In the case of the expansion along the wall represented in Figure 4.10, the pressure shows a sharp decrease especially in the first portion of the divergent (between the throat at $x/y_t = 0$ and approximately $x/y_t = 2$). This corresponds to the portion of wall simulated by an arc-of-circle of radius (R_{td}) where the expansion angle reaches its maximum ($\theta_A=15°$). The remaining divergent wall (i.e. downstream of the attachment point) simulated by a 2nd-order polynomial has its angle decreasing reaching at the exit, for the TIC configuration, a value of $\theta_e=3.3°$.

Chapitre5:

ASYMMETRIC NOZZLE DESIGN: PROCEDURE

5.1. General

The method developed and proposed herein is essentially based on one of the fundamental distinguishing feature of an inviscid axisymmetric flow. The streamlines in such flow-fields lie in planes directed towards the stream wise axis. The stream-sheets established by such streamlines constitute surfaces across which there is no flow, therefore may be adopted as solid boundaries. A geometrical procedure has been developed to design simply and accurately complex three-dimensional profiles. Two nozzle configurations, one of elliptical cross-section and a corrugated one, have been designed using this method. Both configurations may be viewed as typical of the type of nozzles having application in integral rocket-ramjet or scramjet power plants.

5.2. The elliptical profile nozzle

The methodology described above has been employed in the design of a supersonic nozzle with an elliptical cross-section. This configuration is versatile and can be employed as a scramjet, ramjet, or rocket nozzle. It provides a soft transition from an axisymmetric shape to an asymmetric one and is relatively simple to manufacture and test.

Once the design of the axisymmetric nozzle with the desired length and exit Mach number is completed (§3.3), the surrogate asymmetric elliptical profile is selected at the exit cross-section through applying the needed ratio of the major axis to the minor one i.e. b/a=1.5 in the present case (Figure 5.1). By maintaining the same ratio of b/a=1.5, the elliptical shape is replicated at various cross-sections along the longitudinal direction back to the throat. The positions of these cross-sectional profile characteristics are then calculated (Table 5.1), and their collective periphery plane will form the walls of the necessary elliptical nozzle as illustrated in Figure 5.2.
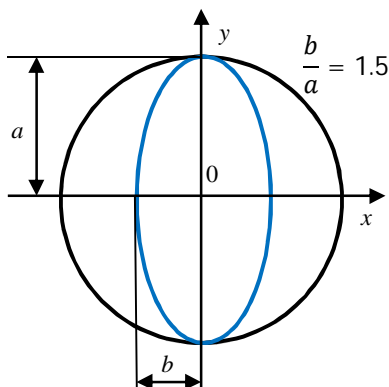

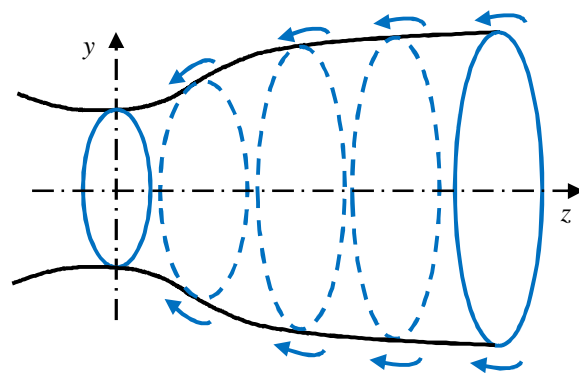**Figure 5.1:** Exit cross-sectional shapes (initial axisymmetric and required elliptic)

Figure 5.2: 3-D elliptical design procedure showing elliptical shapes along the longitudinal z-direction

Table 5.1: Elliptic nozzle constituting cross-sections profile

z (m)	y (m)	x (m)	z (m)	y (m)	x (m)	z (m)	y (m)	x (m)	z (m)	y (m)	x (m)
	0.	0.0203		0.	0.0196		0.	0.0187		0.	0.0176
	0.0030	0.0202		0.0029	0.0195		0.0028	0.0186		0.0026	0.0175
	0.0061	0.0199		0.0059	0.0192		0.0056	0.0184		0.0053	0.0173
	0.0091	0.0194		0.0088	0.0187		0.0084	0.0179		0.0079	0.0168
	0.0122	0.0186		0.0118	0.0180		0.0112	0.0172		0.0106	0.0161
0.06	0.0152	0.0176	**0.05**	0.0147	0.0170	**0.04**	0.0140	0.0162	**0.03**	0.0132	0.0152
	0.0183	0.0162		0.0177	0.0157		0.0169	0.0150		0.0159	0.0141
	0.0213	0.0145		0.0206	0.0140		0.0197	0.0134		0.0185	0.0126
	0.0244	0.0122		0.0236	0.0118		0.0225	0.0112		0.0212	0.0106
	0.0274	0.0088		0.0265	0.0085		0.0253	0.0081		0.0238	0.0077
	0.0305	0.		0.0295	0.		0.0281	0.		0.0265	0.

z (m)	y (m)	x (m)	z (m)	y (m)	x (m)	z (m)	y (m)	x (m)	z (m)	y (m)	x (m)
	0.	0.0163		0.	0.0148		0.	0.0135		0.	0.0133
	0.0024	0.0162		0.0022	0.0147		0.0020	0.0134		0.0020	0.0132
	0.0049	0.0160		0.0044	0.0145		0.0040	0.0132		0.0040	0.0130
	0.0073	0.0156		0.0066	0.0141		0.0061	0.0129		0.0060	0.0127
	0.0098	0.0149		0.0088	0.0135		0.0081	0.0124		0.0080	0.0122
0.02	0.0122	0.0141	**0.01**	0.0111	0.0128	**0.0025**	0.0101	0.0117	**0.**	0.0100	0.0115
	0.0147	0.0130		0.0133	0.0118		0.0122	0.0108		0.0120	0.0106
	0.0171	0.0116		0.0155	0.0105		0.0142	0.0096		0.0140	0.0095
	0.0196	0.0098		0.0177	0.0088		0.0162	0.0081		0.0160	0.0080
	0.0220	0.0071		0.0200	0.0064		0.0183	0.0059		0.0180	0.0058
	0.0245	0.		0.0222	0.		0.0203	0.		0.0200	0.

Figure 5.3 displays the diverse cross-sections defined above through the application of ellipse equation and its major to minor axes represented by Equation 5.1 and Equation 5.2 respectively:

$$\frac{x^2}{a^2} + \frac{y^2}{b^2} = 1 \tag{5.1}$$

$$\frac{b}{a} = 1.5 \tag{5.2}$$

The supersonic section of the elliptic nozzle is represented in Figure 5.4. It shows the diverse cross-sections that are refined near the throat as the property gradients at this position are usually higher in the contoured configurations.
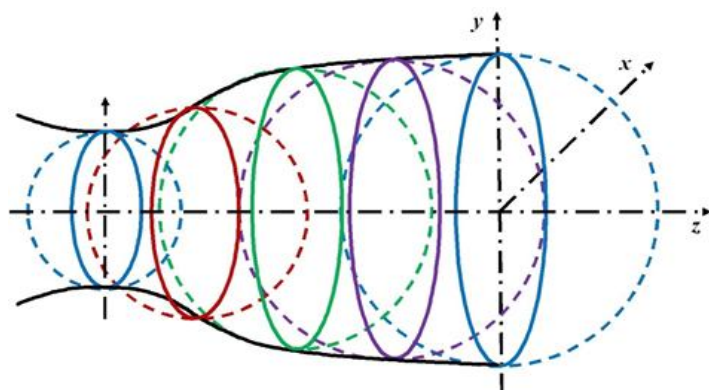

Figure 5.3: Diverse cross-sectional shapes (initial axisymmetric and required elliptic)
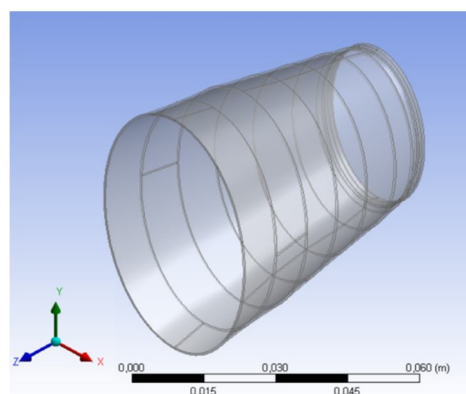

Figure 5.4: Elliptical nozzle supersonic section

5.3. The corrugated profile nozzle

Another asymmetric configuration has been designed using the same methodology described above. The corrugated lobed nozzle has been shown to have significant acoustic advantages. In its supersonic part, it produces less jet noise than its corresponding axisymmetric configuration, therefore making it valuable for applications where noise reduction is crucial such as in airports or urban areas.

The designed corrugated nozzle uses the same initial axisymmetric profile employed for the construction of the elliptical configuration (§3.3 and 5.2). The four petals of the corrugated configuration are constituted by the intersection of two ellipses having the same major axis to the minor axis ration (i.e. b/a=3) as shown in Figure 5.5.

By maintaining the same ratio of b/a=1.5, the elliptical shape is replicated at various cross-sections along the longitudinal direction back to the throat. The positions of these cross-sectional profile characteristics are then calculated (Table 5.2), and their collective periphery plane will form the walls of the necessary elliptical nozzle.

Table 5.2: 4-lobes corrugated nozzle constituting cross-sections profile

z (m)	y (m)	x (m)	z (m)	y (m)	x (m)	z (m)	y (m)	x (m)	z (m)	y (m)	x (m)
	0.0096	0.0096		0.0093	0.0093		0.0089	0.0089		0.0084	0.0084
	0.0092	0.0132		0.0088	0.0128		0.0084	0.0122		0.0079	0.0115
	0.0084	0.0174		0.0081	0.0168		0.0077	0.0160		0.0072	0.0151
	0.0073	0.0214		0.0070	0.0206		0.0067	0.0197		0.0063	0.0185
	0.0057	0.0253		0.0054	0.0245		0.0052	0.0234		0.0049	0.0220
0.06	0.	0.0305	**0.05**	0.	0.0295	**0.04**	0.	0.0282	**0.03**	0.	0.0265
	0.0124	0.0093		0.0119	0.0090		0.0114	0.0086		0.0107	0.0081
	0.0163	0.0086		0.0158	0.0083		0.0151	0.0079		0.0142	0.0075
	0.0203	0.0076		0.0196	0.0073		0.0187	0.0070		0.0176	0.0066
	0.0249	0.0059		0.0240	0.0057		0.0229	0.0054		0.0216	0.0051
	0.0305	0.		0.0295	0.		0.0282	0.		0.0265	0.

z (m)	y (m)	x (m)	z (m)	y (m)	x (m)	z (m)	y (m)	x (m)	z (m)	y (m)	x (m)
	0.0077	0.0077		0.0070	0.0070		0.0065	0.0065		0.0064	0.0064
	0.0074	0.0107		0.0067	0.0097		0.0062	0.0090		0.0061	0.0088
	0.0067	0.0140		0.0061	0.0127		0.0057	0.0118		0.0056	0.0115
	0.0058	0.0172		0.0053	0.0156		0.0049	0.0145		0.0048	0.0141
	0.0046	0.0203		0.0041	0.0184		0.0038	0.0172		0.0038	0.0168
0.02	0.	0.0245	**0.01**	0.	0.0222	**0.004**	0.	0.0207	**0.00259**	0.	0.0203
	0.0099	0.0075		0.0090	0.0068		0.0084	0.0063		0.0082	0.0061
	0.0131	0.0070		0.0119	0.0063		0.0111	0.0058		0.0109	0.0057
	0.0163	0.0061		0.0148	0.0055		0.0138	0.0051		0.0135	0.0050
	0.0200	0.0047		0.0181	0.0043		0.0169	0.0040		0.0166	0.0039
	0.0245	0.		0.0222	0.		0.0207	0.		0.0203	0.

z (m)	y (m)	x (m)	z (m)	y (m)	x (m)	z (m)	y (m)	x (m)
	0.0064	0.0064		0.0063	0.0063		0.0063	0.0063
	0.0061	0.0088		0.0060	0.0087		0.0060	0.0087
	0.0055	0.0115		0.0055	0.014		0.0055	0.0114
	0.0048	0.0141		0.0048	0.0140		0.0048	0.0140
	0.0037	0.0168		0.0037	0.0166		0.0037	0.0166
0.002	0.	0.0202	**0.001**	0.	0.0200	**0.**	0.	0.0200
	0.0082	0.0061		0.0081	0.0061		0.0081	0.0061
	0.0108	0.0057		0.0107	0.0056		0.0107	0.0056
	0.0134	0.0050		0.0133	0.0050		0.0133	0.0050
	0.0165	0.0039		0.0163	0.0039		0.0163	0.0039
	0.0202	0.		0.0200	0.		0.0200	0.
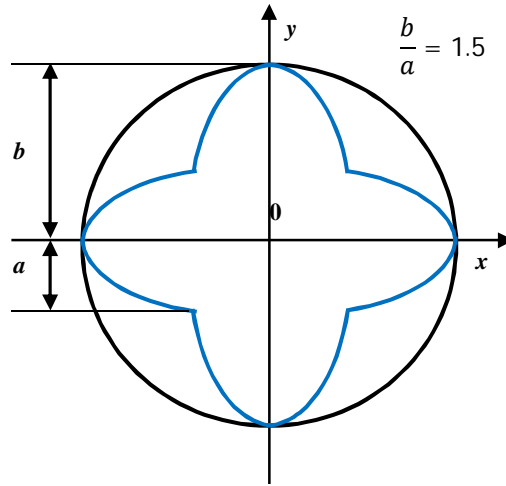
Figure 5.5: Exit cross-sectional shapes (initial axisymmetric and required 4-lobes corrugated)

Figure 5.6 displays the diverse cross-sections defined above through the application of ellipse equation and its major to minor axes represented by Equation 5.3 and Equation 5.4 respectively:

$$\frac{x^2}{a^2} + \frac{y^2}{b^2} = 1 \quad \text{and} \quad \frac{x^2}{b^2} + \frac{y^2}{a^2} = 1 \tag{5.3}$$

$$\frac{b}{a} = 3 \tag{5.4}$$
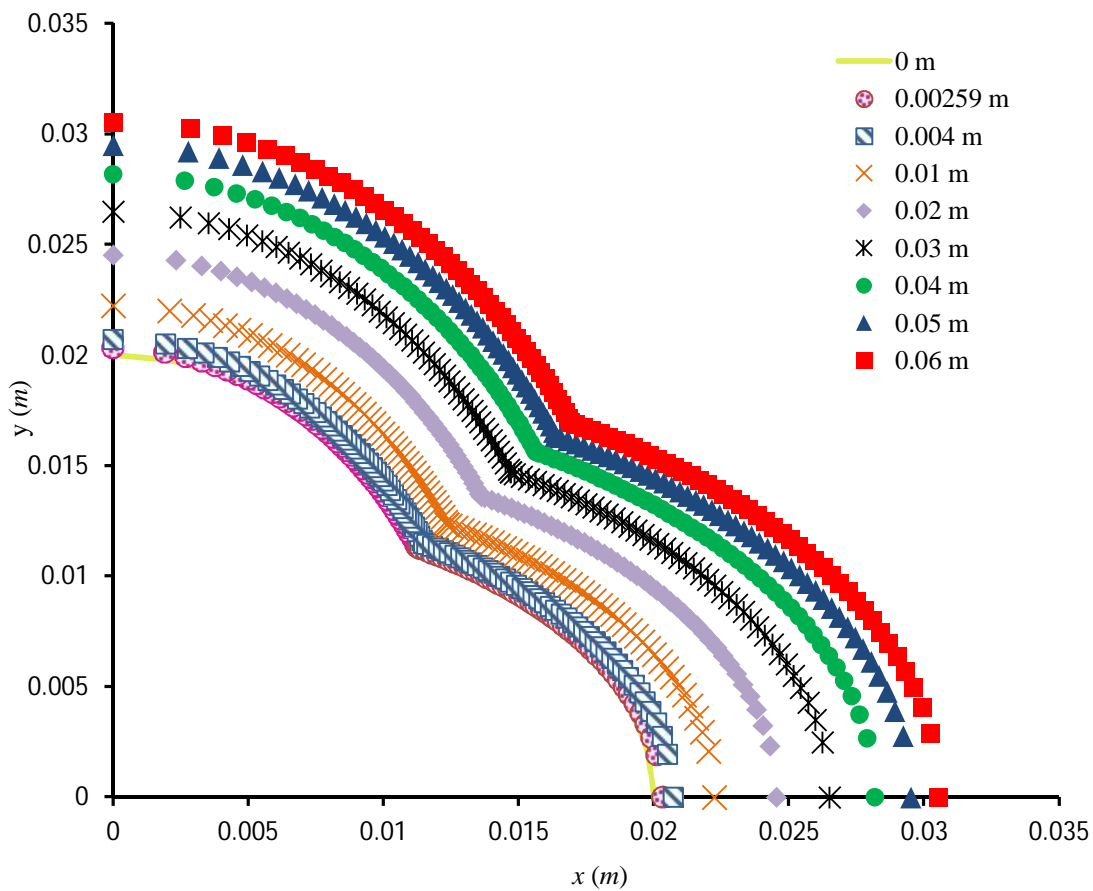
Figure 5.6: Diverse cross-sectional shapes along the 4-lobes corrugated nozzle length

Similarly to the case of the elliptic configuration, the cross-section computed (shown in Table 5.2 and Figure 5.6) are closer near the throat as the property gradients immediately downstream of that position are greater, and this is a characteristic of contoured nozzles that result in shorter lengths and axis-directed jets.

The supersonic section of the 4-lobe corrugated nozzle is represented in Figure 5.7. It shows the diverse cross-sections that have been used to define the profile. The refinement immediately downstream of the throat where the property gradients are larger may be observed.

Figure 5.7: Corrugated nozzle supersonic section

RESULTS AND DISCUSSIONS

6.1. General

At the present time, there seems to be no available exact solution for a fully 3-D viscous turbulent flow-field like the one taking place in a supersonic propulsion nozzle. Therefore, there is no possibilit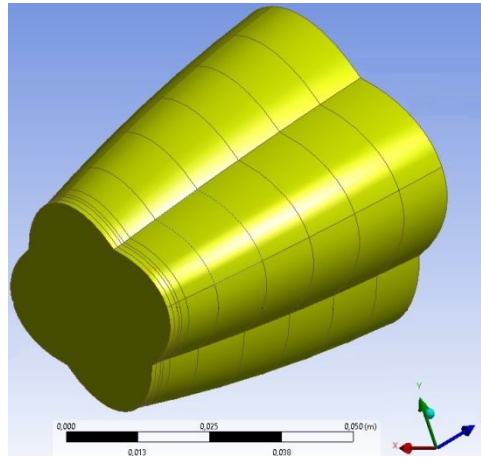y of comparing the results obtained, in order to validate the approach developed and applied, to available results. However and in order to showcase the general capabilities of the present preliminary design approach discussed earlier, 3-D simulations of the flow-field within the two asymmetric configurations were conducted using the Ansys-Fluent CFD environment. Moreover, the results obtained pertaining to the elliptical configurations were compared to the experimental results obtained from a similar configuration that has been tested with air.

All the results from these aspects of the investigations i.e. MoC, CFD and experiments are detailed in the present section.

6.2. The elliptical profile nozzle

The elliptic configuration was selected because of (1) its smooth transition from axisymmetric to asymmetric profile and (2) the availability of the experimental results achieved on such configuration.

6.2.1. CFD computations

The Ansys-Fluent platform was used to perform the 3-D computations taking both the stagnation pressure and temperature equal to those used in the experiments i.e. 15.10^5 Pa and 403K respectively. The ambient atmospheric pressure was set at $1.013.10^5$ Pa.

The governing equations involve the fundamental principles of mass, momentum, and energy conservation. To assess the iterative solution's convergence, the scaled residual that indicates the local imbalance of a conserved variable in each control volume is used. It usually serves as a suitable indicator in most CFD problems. A level of (10^{-6}) has been chosen for the scaled residual, signifying a stringent convergence criterion.

Figure 6.1 illustrates the structured mesh of the divergent section in the elliptic nozzle geometry created in the Ansys-ICEM environment. This multi-bloc structured mesh facilitates cell adaptation without increasing the overall mesh size. It enables mesh refinement in areas with high gradients such as the throat section and wall region where the number of elements was significantly increased. Despite this, the total number of elements was maintained at a reasonable value of 729,120 quadrilateral cells, ensuring satisfactory mesh quality.
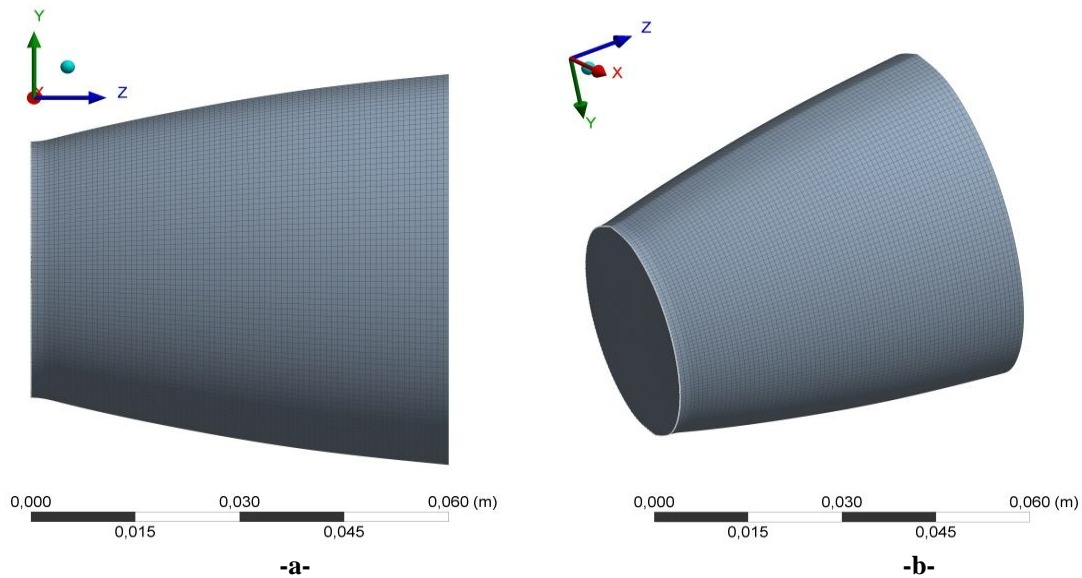
Figure 6.1: Supersonic section structured mesh grid topology of the elliptic nozzle: a) plane; b) isometric

The accuracy of predicting high Mach number flows greatly depends on the chosen numerical approach and turbulence model. The *k-ω* SST turbulence model (cf. §2.3.5) has demonstrated its effectiveness in numerous studies related to supersonic flow fields, showing results closest to experimental findings (Hunter, 1998; Perrot, 2006). In this analysis, the k-ω SST model was therefore chosen as the turbulent model, and Table 6.1 provides an overview of the key settings applied.

Table 6.1: Elliptic nozzle 3-D simulation settings

	Features applied
Model	3D, Elliptic, stationary
Solver	viscous with compressibility effects
	Density based
Turbulence model	*k-ω* SST
Fluid	air, ideal gas
Inlet Boundary Conditions	$P_t = 15.10^5$ Nm^{-2} ; $T_t = 403$ K
Residuals	10^{-6}

6.2.2. Experimental basic setup

In order to perform a proof-of-concept of the procedure developed, the results achieved through the 3-D simulation were compared to those experimental that used cold compressed air testing on such geometry, and available in the literature (Haddad, 1988).
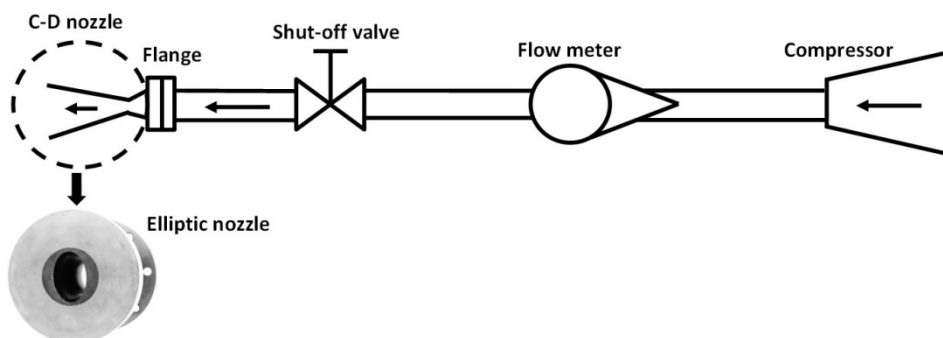

Figure 6.2: Schematic layout of experimental apparatus (Haddad 1988)

Figure 6.2 basically shows a schematic layout of the experimental equipment setup. The static pressures were measured at different equally spaced locations along the centerline, the exit section major axis and along the exit section minor axis of the elliptic nozzle. Appendix B and Appendix C display the details of the experimental apparatus and subsonic section design procedure respectively.

6.2.3   Numerical results

The static pressure and Mach distribution contours resulting from the CFD simulation are shown in Figure 6.3 and Figure 6.4 respectively. Both plane and isometric contours are displayed.
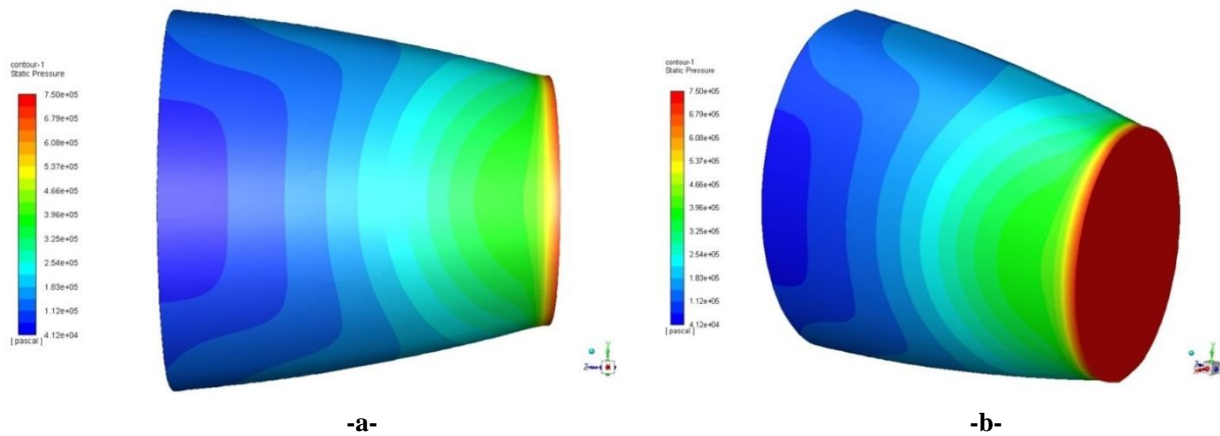

-a-   -b-

Figure 6.3: 3D pressure contours: a) plane; b) isometric

The isometric pressure contour shows the supersonic expansion occurring within the elliptical nozzle's supersonic section. It starts at a pressure of 7.5 bars at the throat (Figure 6.3). This pressure corresponds to a sonic Mach value. It is followed by a supersonic expansion within the divergent section, culminating at the exit with an average Mach value of 2.5 (cf. Figure 6.4). It may be observed that the pressure contour representing the supersonic expansion commences in a symmetric way (represented by parabolas as isobars) at the throat before deviating from its symmetrical pattern due to the nozzle's asymmetry and the influence of the boundary layer. A similar behavior can be observed when displaying the Mach number contour (Figure 6.4). With the increase in the nominal Mach number, a similar increase in computed flow non-uniformity caused by the presence of the boundary layer may be observed that indicates the significant impact of viscosity. Nonetheless, the flow accelerates in a smooth and continuous way until it reaches the exit cross-section.
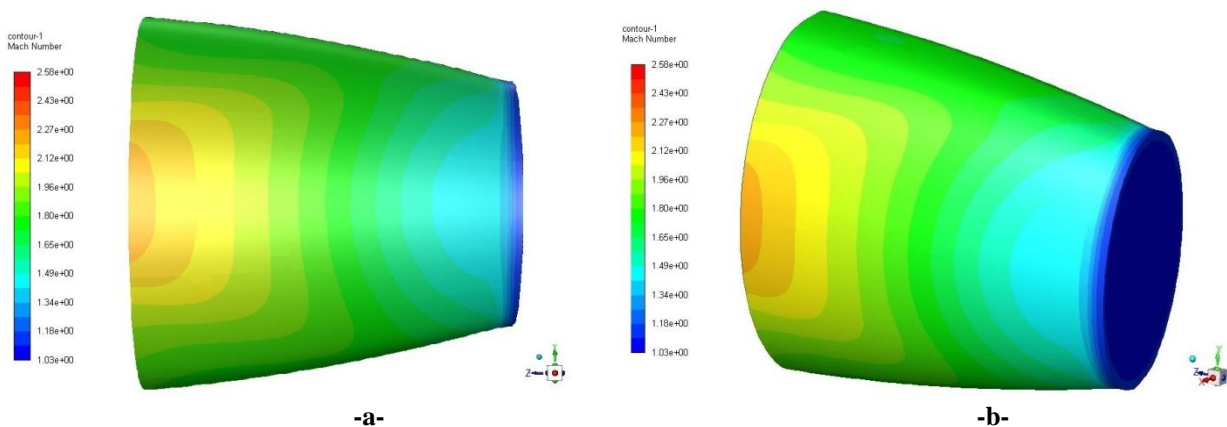

-a-   -b-

Figure 6.4: 3D Mach number contours: a) plane; b) isometric

The pressure and Mach distributions along the central plane are displayed below. Near the throat, the distributions exhibit the well-known arc representing the isobars (Figure 6.5) and isoMach (Figure 6.6) but move away from this distribution downstream under the effect of the asymmetry of the elliptical geometry. The central body is more pronounced in terms of Mach, reflecting the significant depression in the central body compared to that near the walls.
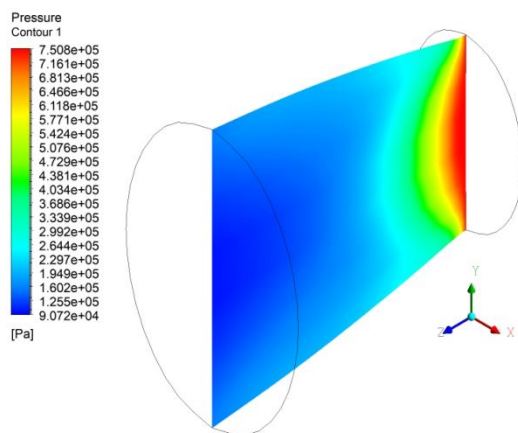
Figure 6.5: 3D pressure contour along center plane   **Figure 6.6:** 3D Mach contour along center plane
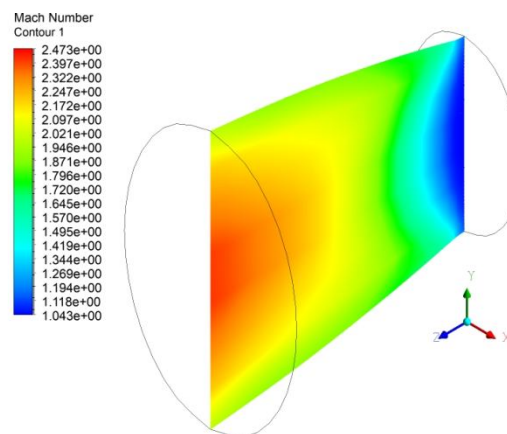
The velocity vectors resulting from the flow-field computation were drawn and represented in Figure 6.7. They show the smooth acceleration of the flow along the walls demonstrating an adequate convergence of the procedure that demonstrate a satisfactory expansion of the flow without shock waves.

-a-   -b-
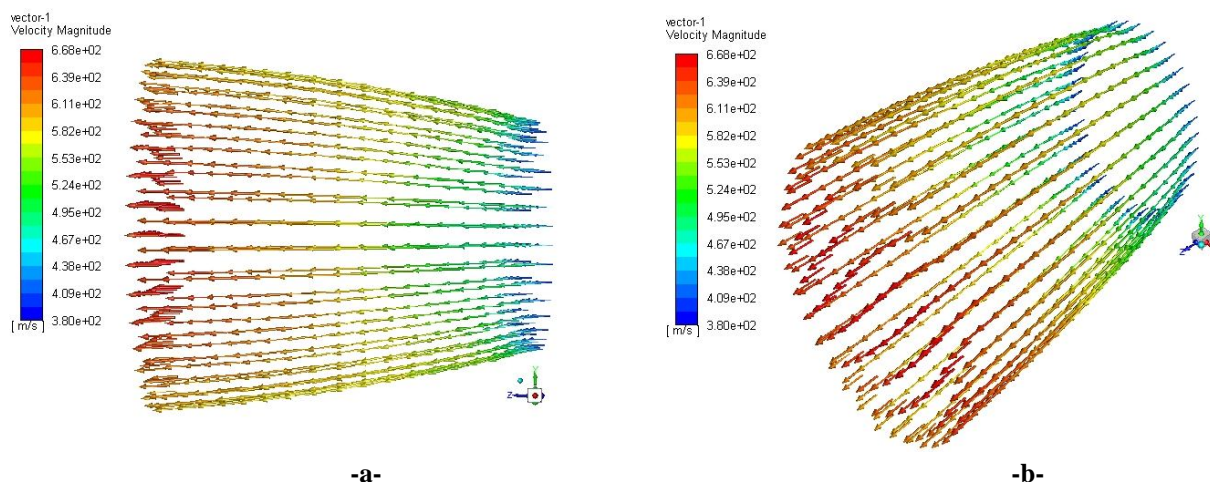
Figure 6.7: Velocity distribution along the walls of the elliptical nozzle: a) plane; b) isometric

The gradual acceleration of the flow at some specified cross-sections is shown in Figure 6.8. It may be seen that a significant portion of this acceleration occurs right downstream of the throat. An approximate 50% of the acceleration may be seen to take place in the initial 30% of the nozzle's divergent section which is comprised between z=0mm and z=20mm. This pattern is typical feature of bell-shaped nozzles. Within the remaining portion of the divergent section (approximatively between z=20mm and z=60mm that represents the exit section), the flow continues to accelerate and is directed towards the axial direction to maximize thrust while minimizing the required nozzle length.
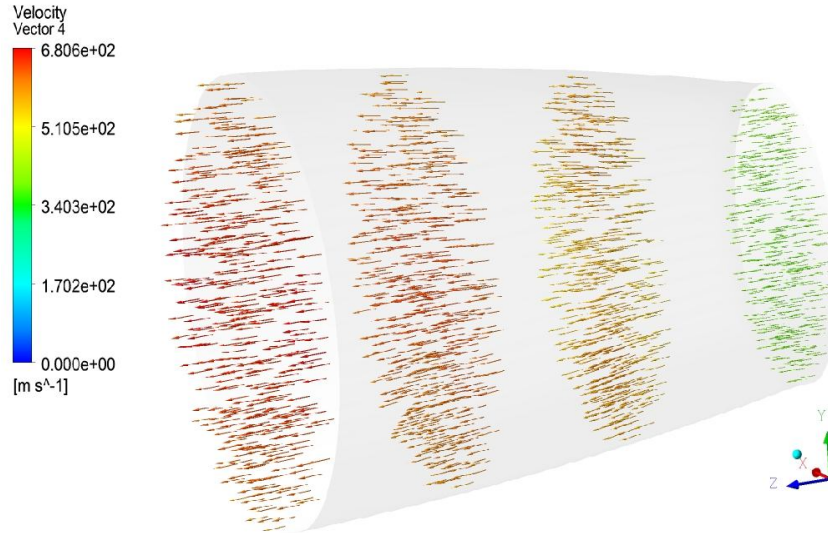
Figure 6.8: Velocity distribution along four cross-sections of the elliptic nozzle divergent
(z=0mm ; z=20mm ; z=40mm; z=60mm)

Figure 6.9 exhibits the pressure distribution across four cross-sections along the flow path that extends from the throat to the nozzle exit. It illustrates the variations in pressure gradients between the minor and major axes of the elliptical configuration, and the original axisymmetric profile used to generate it. Immediately downstream of the throat i.e. at $z = 4.07$ mm, pressure gradient between wall and centerline is found equal to almost 25% and 15% of the stagnation pressure for the minor and major axes respectively. In the case of the original axisymmetric nozzle, from which the elliptical design was generated, this gradient reaches 35%. As we move toward the exit section i.e. at $z = 20.69$ mm, $z = 42.14$ mm, and ultimately at $z = 60$ mm, these discrepancies tend to decrease and the pressure curves for the three configurations become more closely aligned.

The light disparity between the CFD asymmetric solution carried out by 'Fluent' for the elliptical nozzle and the axisymmetric MoC solution for the original axisymmetric configuration can be attributed to the computational procedures used to analyze the flow-field in each approach. While the MoC calculations are performed along the Mach lines, therefore providing a representation of the real nature of the solution, the CFD computations heavily rely on the grid topology structure that represents the elliptical geometry. The comparison between the elliptical and the original axisymmetric profiles from which it was generated is essentially used as an evaluation of the effectiveness of the developed procedure.
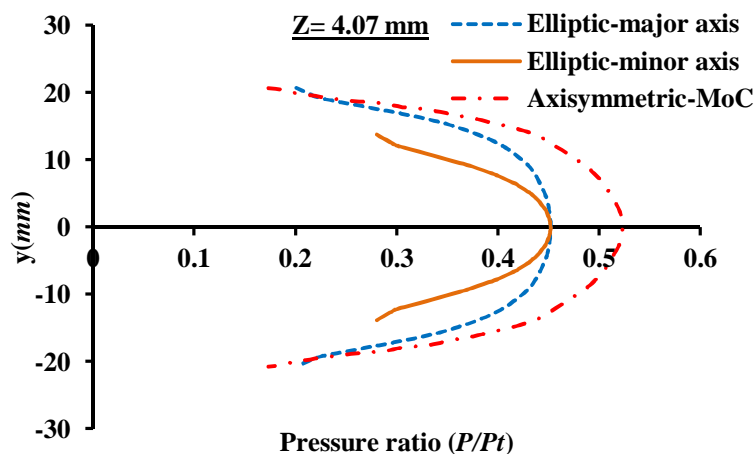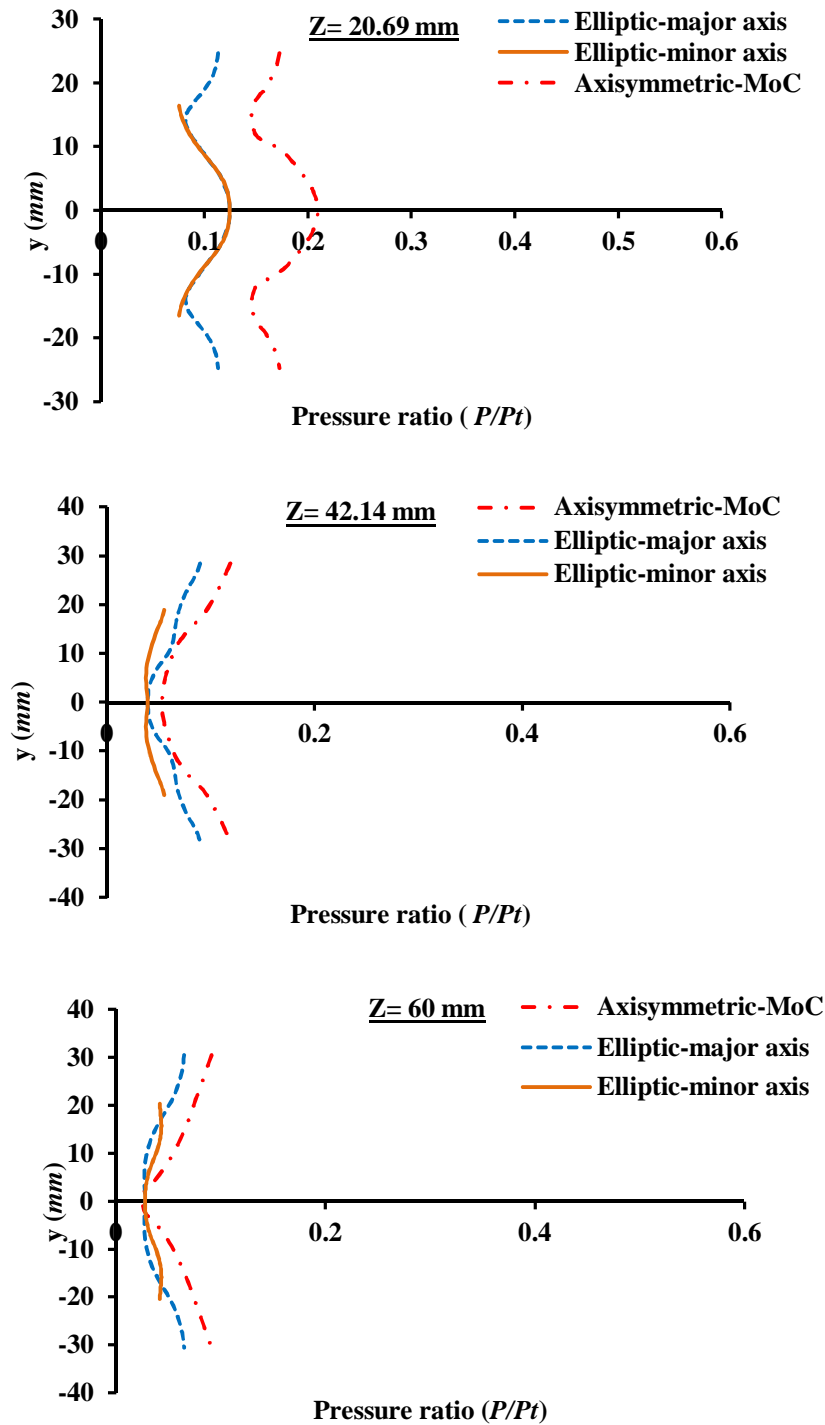
Figure 6.9: Pressure distribution along cross sections of the elliptic and axisymmetric nozzle configurations

The pressure distributions at four cross-sections along both the major and minor axes of the divergent section of the elliptical configuration are displayed in Figure 6.10. The gradual 'straightening up' of the pressure that tends to become more uniform as we approach the exit section demonstrates efficiency of the control achieved by the elliptical supersonic geometry in the expansion process.

This showcases the elliptical nozzle's capacity to regulate and improve the quality of the expansion process.

-a-

-b-
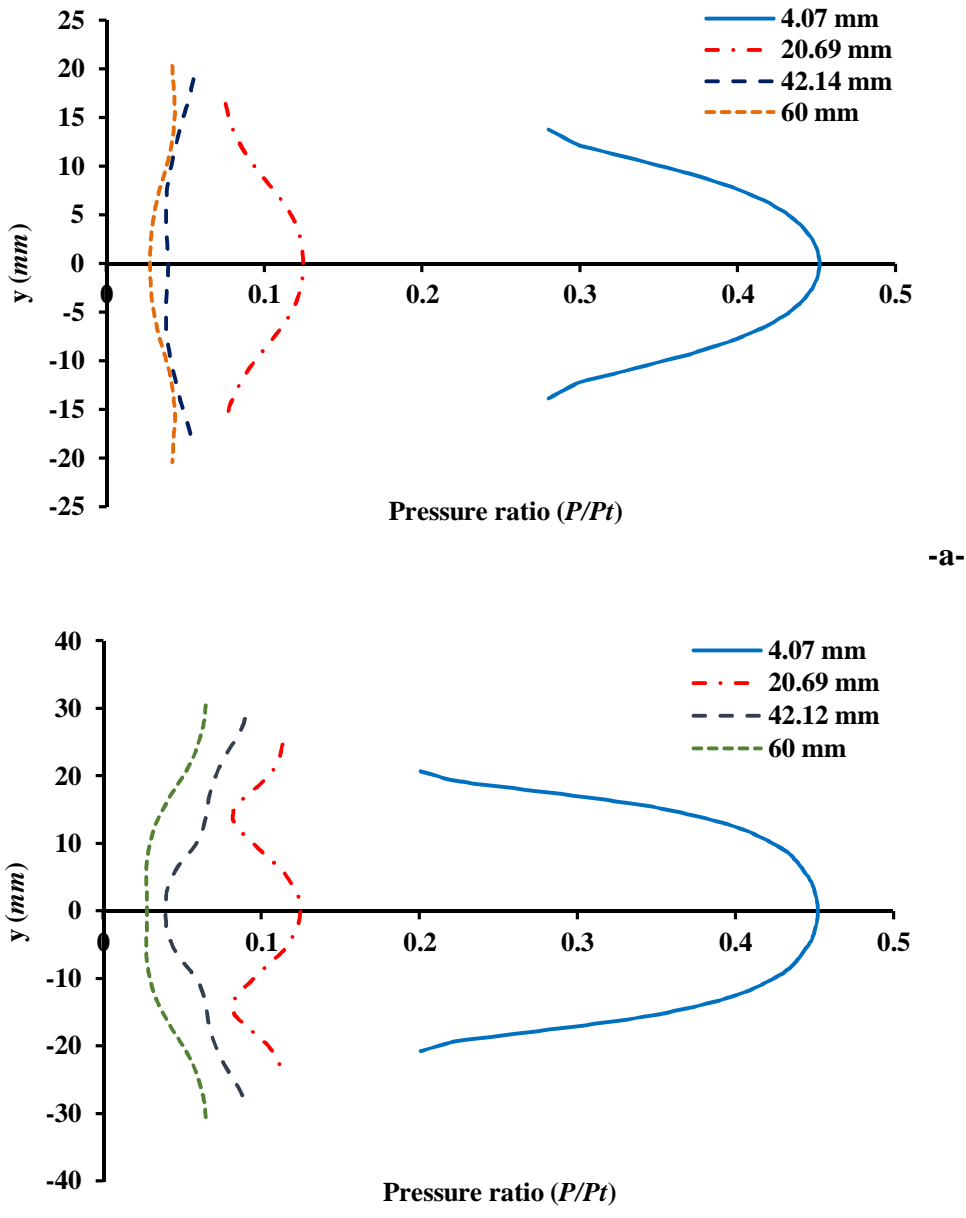
Figure 6.10: Pressure distribution along cross sections of the elliptic nozzle configuration:
a) minor axis; b) major axis

This effectiveness is further illustrated by the performance parameters displayed in Table 6.2 which comprises essentially the thrust, the mass flow rate, the thrust coefficient, and the exit Mach number. The main objective is to compare the performances of the elliptical configuration in terms of the control of the expansion process along with the delivery of a viable thrust to those that resulted from the axisymmetric nozzle from which the asymmetric elliptic nozzle has been generated using the procedure developed.

Table 6.2: Performance characteristics of the elliptical (CFD) and
axisymmetric configurations (MoC)

	Thrust (N)	$\dot{m}$ (kg/s)	$T/\dot{m}$ (m/s)	C_T	M_{exit}
Axisymmetric configuration	2470	2.8	882	1.31	2.36
Elliptic configuration	1627	2.5	650	1.23	2.41

The results shown in Table 6.2 reveal that the axisymmetric configuration exhibits a higher mass flow rate and greater thrust. These results are primarily due to the larger cross-sectional area of the axisymmetric configuration which is 34% greater than that of the elliptical design. To discard the influence of the mass flow rate on the thrust, a comparison in terms of specific thrust is performed. In this context, the axisymmetric configuration demonstrates a 25% advantage over its elliptical counterpart, showing the significant internal performance achieved with axisymmetric geometries which allowed them to be preferred and used for many decades as propulsion elements.

In terms of the thrust coefficient (C_T) that identifies the efficiency of the expansion process within the divergent section of a C-D propulsion nozzle, the axisymmetric configuration once again demonstrates a 6% advantage over its elliptical counterpart, highlighting once more its great ability to control the supersonic expansion of the combustion gases.
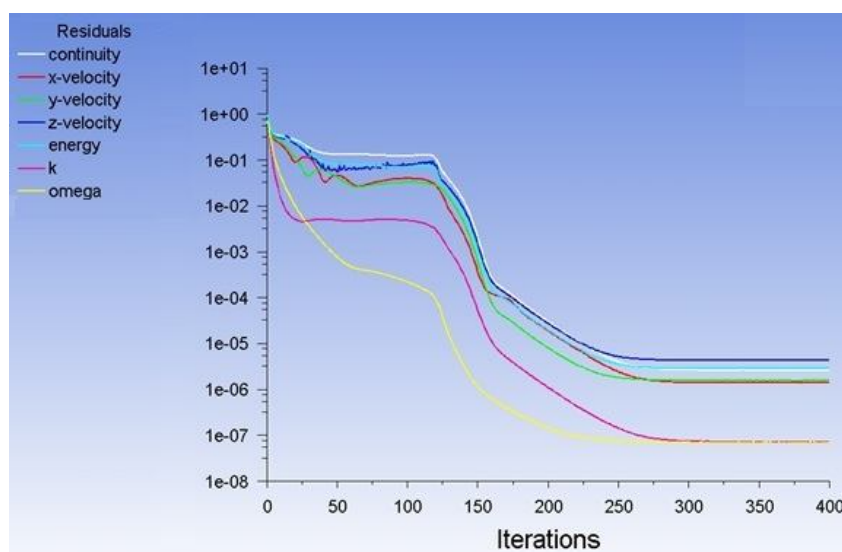
Figure 6.11: Scaled residuals of the elliptical flow-field computations using *k-ω* sst turbulence model

Figure 6.11 shows the iterations needed for the convergence of the computations. The residual, in the present case and as shown in Table 6.1, has been set to (10^{-6}) which is a stringent condition. Around 300 iterations were necessary to reach the needed solution represented in the present case of the RANS equations by the difference between the left and the right side of the equations that are scaled for the purpose of making it more interpretable and independent of the problem magnitude (Ansys, 2022).

6.2.4   Comparison to experimental results

Figure 6.12 displays the static pressure development along the centerline resulting from the CFD simulation performed on the elliptical nozzle, and that impending to the MoC computations carried out on the original axisymmetric configuration. These results are compared to the experimental data gathered from the testing carried out on a similar elliptical nozzle (Haddad, 1988) and presented in Appendix C. The agreement between the results of the experimental investigation and the CFD solution is found to be favorable as both predict the flow discontinuity occurring at the point of rate of change in the flow property labeled 'A' (Figure 6.12). It may moreover be observed that the supersonic expansion proceeds in a smooth and satisfactorily way along the centerline of the elliptical nozzle without any signs of shock waves or separation.

The MoC computations that are known to always follow the characteristics (the Mach lines in the present case) provide the true nature of the solution. As represented in Figure 6.12, The CFD results, while not as precise as the MoC solution, still manage to preserve the genuine characteristics of the expansion process thus demonstrating the validity of the proposed approach.
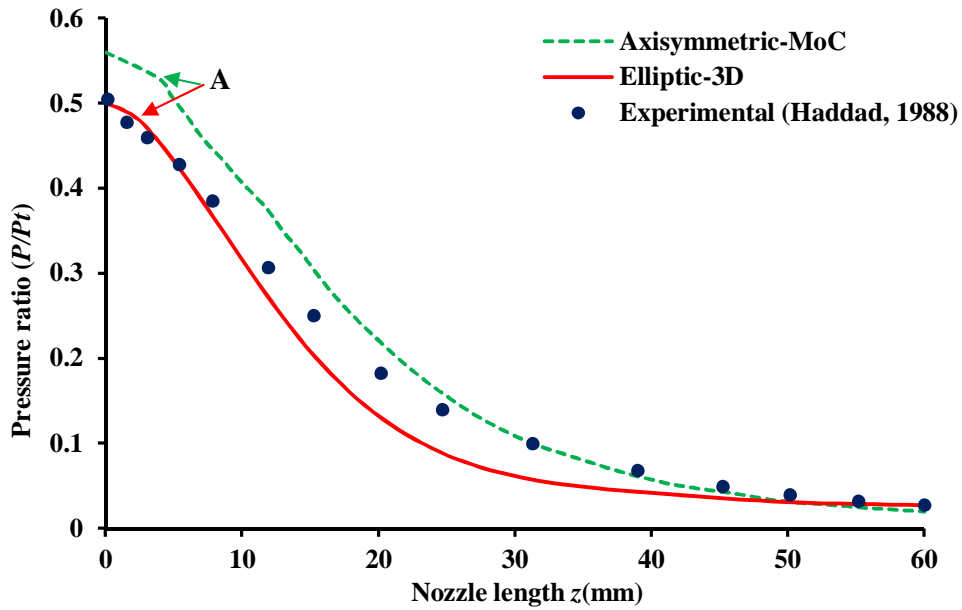
Figure 6.12: Pressure distribution along centerline

In Figure 6.13, a comparison is performed between the results derived from the experimental pressure measurements along the major axis of the elliptical nozzle exit cross-section, the CFD solution, and the MoC results conducted on the axisymmetric original configuration. The CFD pressure along the major axis is found to be well-predicted, with its gradient between the centerline and the wall approximately representing 3.5% of the total pressure, closely matching that of the experimental value of 4.5% of the total pressure.
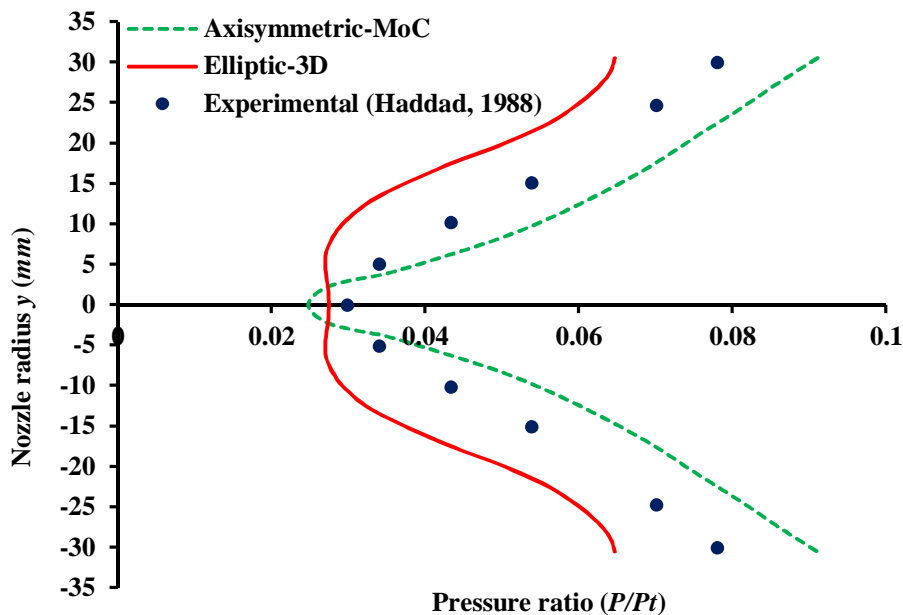
Figure 6.13: Pressure evolution along the exit cross-section major axis

6.3. The corrugated profile nozzle

A corrugated propulsion nozzle is an innovative type of nozzles mostly used in aerospace engineering systems such as rocket and jet propulsion engines. It features a distinctive geometric design with corrugations along its interior surface that disrupt the flow of exhaust gases as they pass through this particular profile. The ongoing research and development the corrugated propulsion nozzles are subject to nowadays involves exploring various corrugation patterns and geometries to optimize performance depending on their use that include high-performance aircraft, where their unique design can enhance thrust efficiency, thermal management, and overall propulsion system performance.

6.3.1. CFD computations

The Ansys-Fluent platform was again applied to carry out the asymmetric 3-D computations pertaining to the corrugated four-petal supersonic section propulsion nozzle. The totale pressure and temperature were taken equal 15.105 Pa and 403K respectively. The ambient atmospheric pressure was set at 1.013.105 Pa.

The governing equations involve the fundamental principles of mass, momentum, and energy conservation. The iterative solution's convergence was again assessed through the scaled residual at a chosen level of (10^{-6}) which is a stringent value for this parameter in the present conditions.

Figure 6.14 illustrates the structured mesh of the divergent section in the corrugated nozzle geometry created in the Ansys-ICEM environment. A mesh refinement in areas with high gradients, the throat section and wall region in this case, was applied. In both the plane representation of Figure 6.14, the petal structure is clearly defined while its isometric description shows the four petals representing the corrugated configuration. The total number of elements was maintained at a reasonable value of 94,645 quadrilateral cells, ensuring a satisfactory mesh quality.
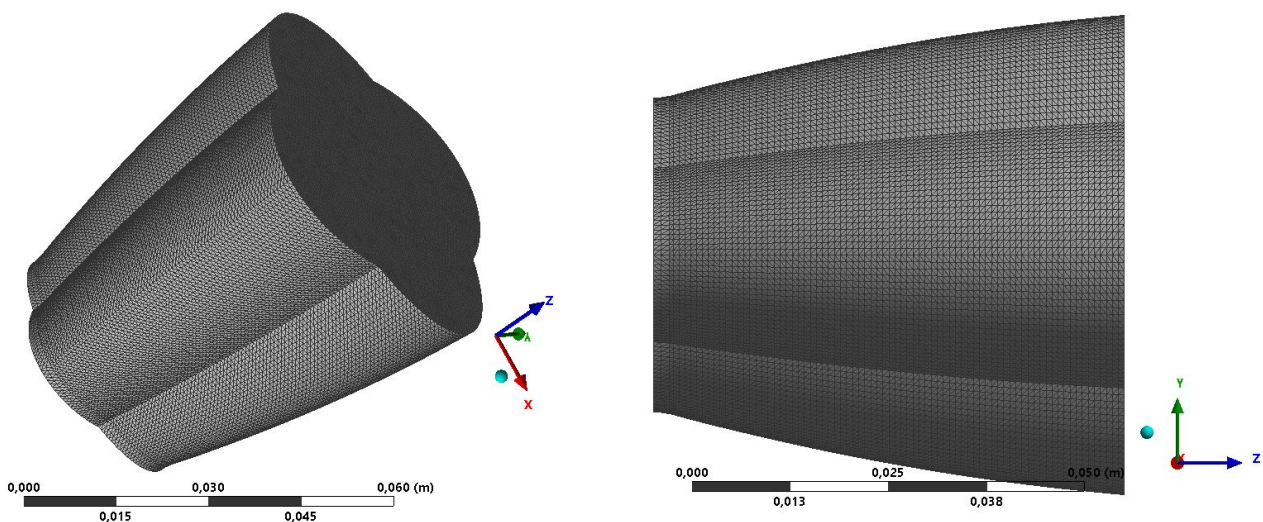
Figure 6.14: Supersonic section structured mesh grid topology of the corrugated nozzle: a) plane; b) isometric

The *k-ω* SST model (cf. §2.3.5) was again the turbulence model applied for the system closure. Hunter (1998) and Perrot (2006) have shown its effectiveness in modelling the turbulence

within high Mach number flows. Table 6.3 provides an overview of the key settings applied that are similar to a great extent to those displayed in Table 6.1.

Table 6.3: Corrugated nozzle 3-D simulation settings

	Features applied
Model	3D, Corrugated, stationary
Solver	viscous with compressibility effects
	Density based
Turbulence model	$k\text{-}\omega$ SST
Fluid	air, ideal gas
Inlet Boundary Conditions	$P_t = 15.10^5 \, \text{Nm}^{-2}$; $T_t = 403 \, \text{K}$
Residuals	10^{-6}

6.3.2   Numerical results

The solution in terms of the static pressure along the divergent section centerline and wall are shown in Figure 6.15. Because of the relatively significant attachment angle (situated at the attachment point noted 'A' in Figure 6.15), a substantial sharp expansion is exhibited in the vicinity of the throat before straightening near the outlet. This sharp expansion is a distinguishing feature of the contoured or bell-shaped nozzles, where most of the expansion process takes place immediately downstream of the throat while the remaining length directs the flow towards the axial direction. This would lead to a shorter divergent section and a maximum thrust in the axial direction.
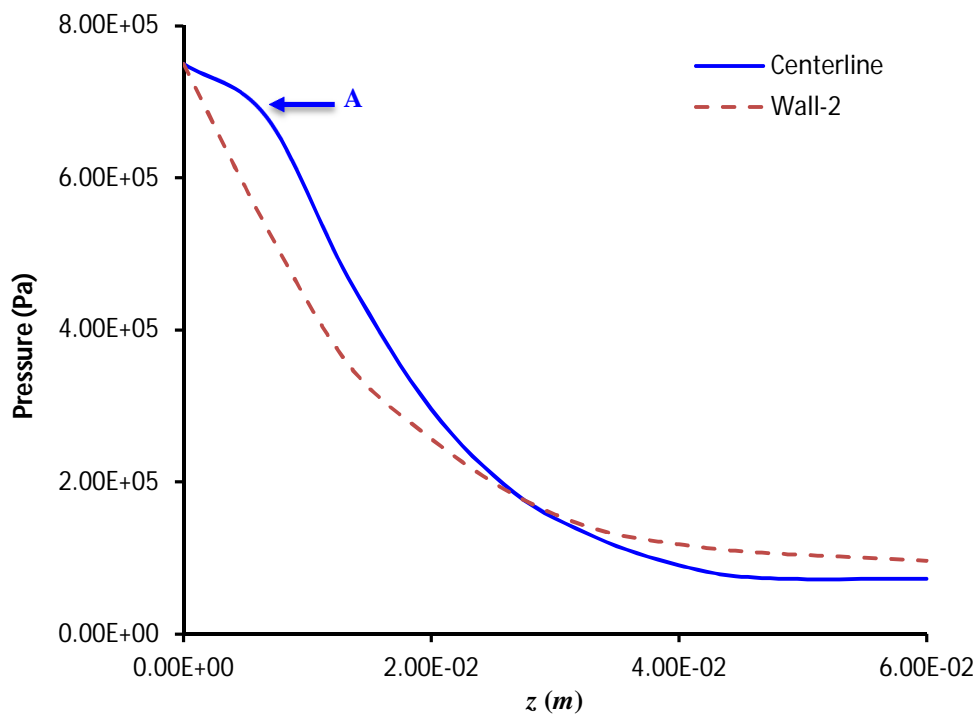
Figure 6.15: Pressure distribution along centerline and wall

The static pressure distribution contours resulting from the CFD simulation s shown in Figure 6.16. Both plane and isometric contours are displayed.
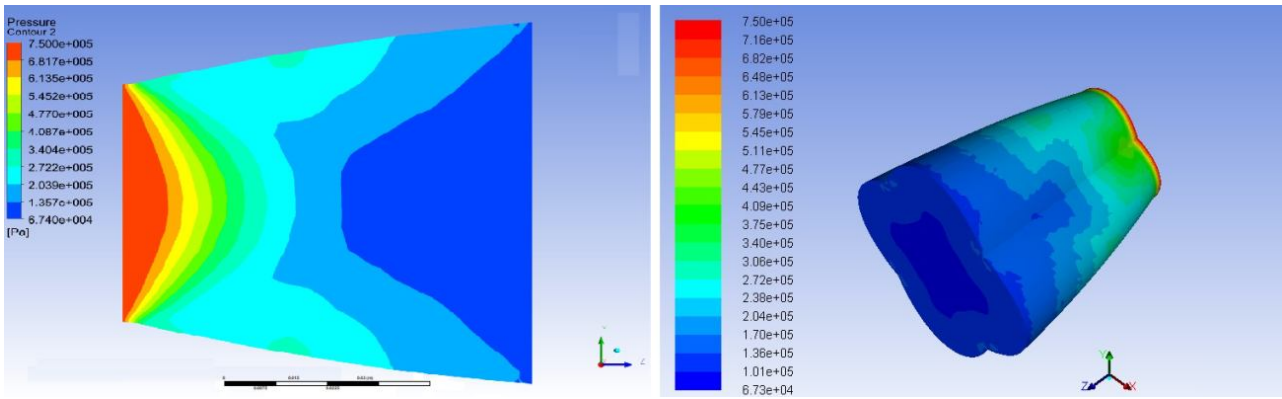
Figure 6.16: 3D pressure contours: a) plane; b) isometric

The pressure tarts at 7.5 bars at the throat that corresponds to a sonic Mach value (It is the same starting pressure as for the elliptical nozzle since the convergent are identical to both configurations). It is followed by a smooth supersonic expansion culminating at the exit with an average Mach value of 2.35 (cf. Figure 6.17).

The isobars are represented by parabolas immediately downstream of the throat. They however deviate from this geometry further downstream as a result of the corrugated geometry that influences the boundary layer.

A similar trend may be observed in the case of the Mach number contours represented in Figure 6.17. Indeed, the increase in the Mach number leads to an increase of the dissymmetry of the flow-field. However, the flow may be seen as accelerating in a smooth and continuous from throat to exit.
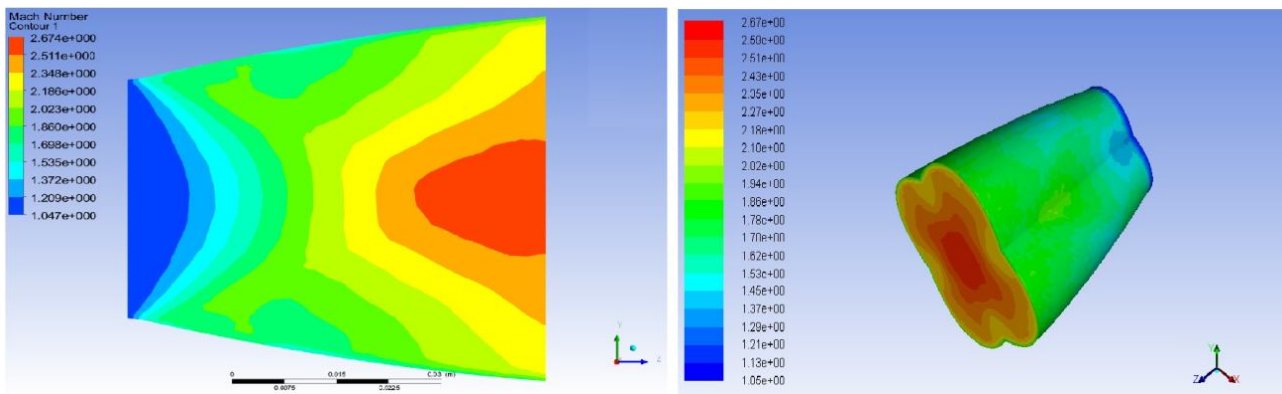
Figure 6.17: 3D Mach number contours: a) plane; b) isometric

The pressure and Mach distributions along the central plane are displayed in Figure 6.18 and Figure 6.19 respectively.

The well-known arcs representing the isobars and isoMach in Figure 6.18 and Figure 6.19 respectively may be clearly observed downstream of the throat. This symmetry is gradually lost, under the asymmetry of the walls, as we progress further downstream.

The central region exhibits a more noticeable Mach effect, indicating a substantial decrease in pressure in the central region in contrast to the region near the walls.
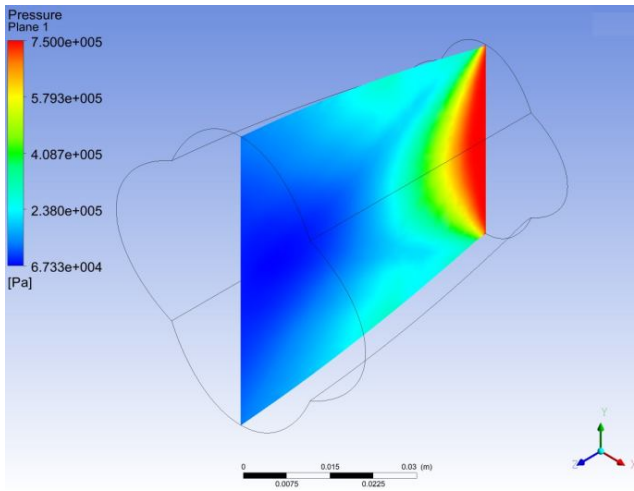
Figure 6.18: 3D pressure contour along center plane
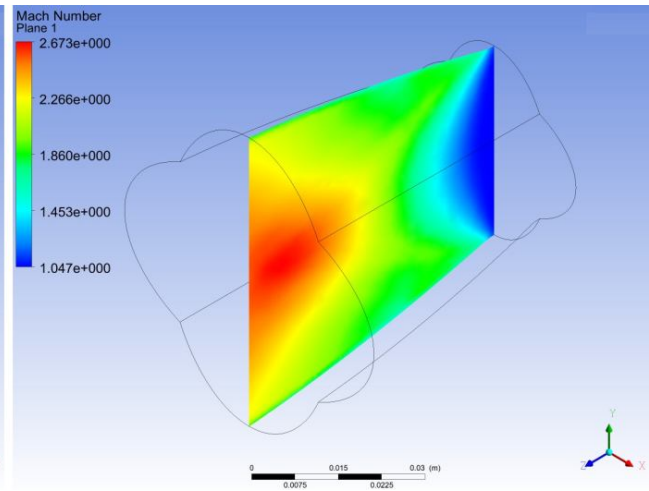
Figure 6.19: 3D Mach contour along center plane

The velocity vectors resulting from the flow-field computation are represented in Figure 6.20 and Figure 6.21. They exhibit the gradual increase in flow velocity along the center plane (Figure 6.20) and within the corrugated divergent section (Figure 6.21), signifying a satisfactory convergence of the process that ensures a smooth, and effective free from shock waves expansion of the flow.

It may be seen that the acceleration is more pronounced within the center core of the corrugated configuration away from the four petals where the velocity is lower. This may be the result of the influence of the boundary layer that seems to be more pronounced in the round petals.
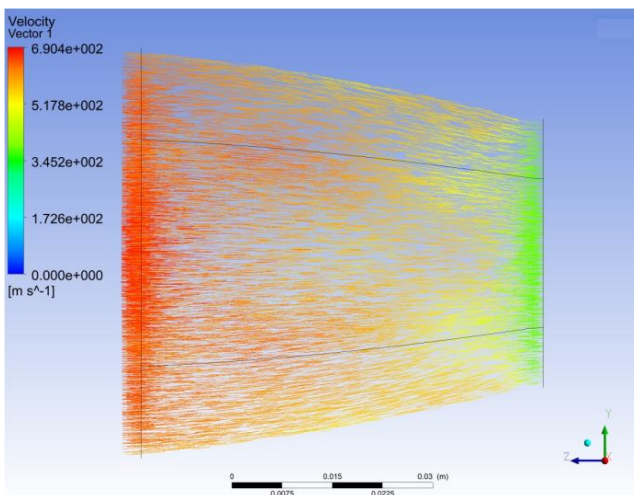
Figure 6.20: Velocity distribution along the center plane
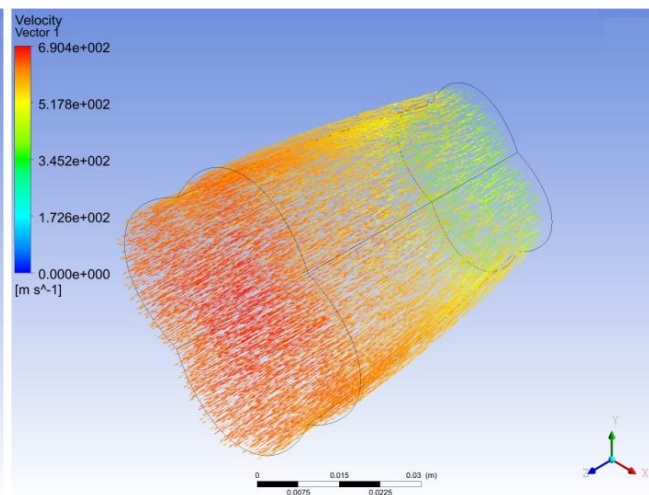
Figure 6.21: Velocity distribution within the corrugated nozzle

The monitoring scaled residuals during an iterative solution process assesse the convergence of the solution. The RANS equations used are a set of equations that describe the time-averaged behavior of the expansion, modeling the turbulent flow and reaching a convergence within the residual chosen. Figure 6.22 illustrates the iterations required to achieve computational convergence. The residual, as indicated in Table 6.3 and which is associated with the universal conservation equations along with the turbulent kinetic energy (k) and dissipation rate (ω), has been

set to a stringent value of (10^{-6}). It took approximately 250 iterations to attain the required solution, showing an appropriate grid refined in regions of high gradients and near walls.
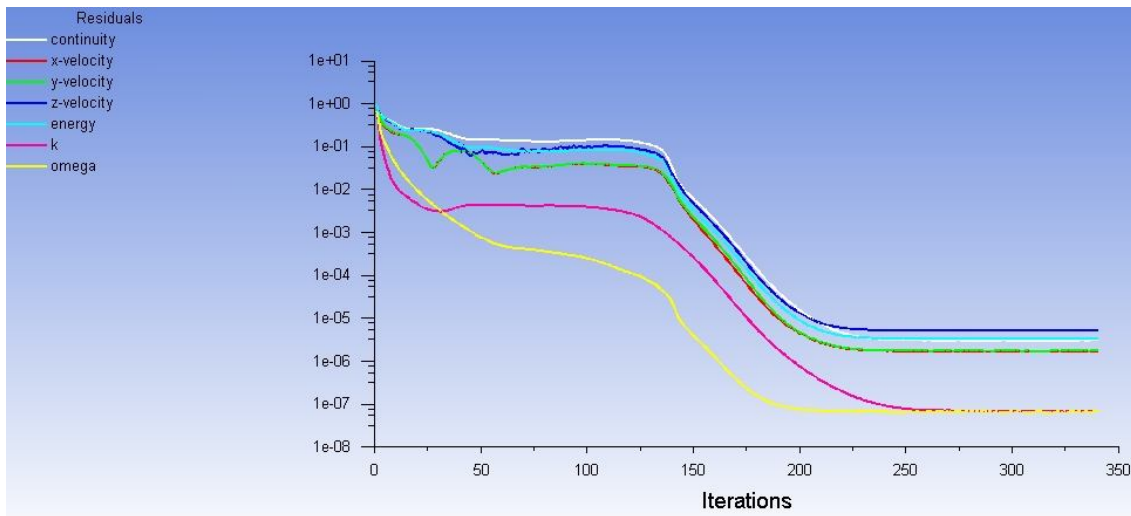
Figure 6.22: Scaled residuals of the corrugated flow-field computations using *k-ω* sst turbulence model

_____

CONCLUSIONS AND RECOMMENDATIONS FOR FURTHER WORK

7.1. Conclusions

The high internal performances achieved by axisymmetric nozzles led them to be employed in both traditional and modern aircrafts, the primary concern being the design of jet engine exhaust nozzles configurations where the installed system did not result in too much drag or thrust loss. The relatively new air-breathing hypersonic systems need greater nozzle integration with the aft-body constituting parts in order to produce higher thrust-minus-drag performances.

7.1.1. The truncated ideal contour (TIC) nozzle

The process concerning the design of a de-Laval contoured single-bell TIC nozzle has been carried out with the aim of producing a performant short configuration. The truncation was performed at 20% of the total length showed as the station that strikes a balance between minimizing thrust loss and limiting weight gain. Flow-field simulations were conducted for the supersonic section of both configurations using the MoC along with a CFD analysis of the flow within the TIC configuration.

The comparison of the IC configuration and its TIC counterpart led to the following conclusions:

1. In both IC configurations, the profiles were found to be similar downstream of the throat up to approximately halfway through i.e. at around $x \approx 0.05$m. Downstream of that position, the the contours start to diverge slightly. This similarity near the throat is primarily due to the influence of the circular-arc throat contour (R_{td}) on the supersonic expansion process. Further downstream, the expansion is controlled by the 2nd-order quadratic polynomial, and this seems to be the reason of the slight discrepancies in the profiles as the two configurations as the polynomials show different constants A_w, B_w, and C_w.

2. In terms of performances, the IC nozzle demonstrated a thrust coefficient and specific impulse close to those of the configuration found in the literature and to which it has been compared. The errors were within 5.9% and 4.3%, respectively.

3. The static pressure distribution along both the centerline and wall revealed a sharp expansion immediately after the throat until the attachment point that shows a maximum divergence angle. Further downstream, the expansion becomes steadier mainly because of the influence of the 2nd-order quadratic polynomial wall with its divergence angle reaching $\theta_E = 0°$ at the exit. The Mach number are found to increase accordingly with the decrease of the pressure. They reach a maximum of $M = 4.3$ at the exit cross-section.

4. The TIC configuration resulting from the truncation of its IC counterpart was designed through the application of the both the Rao and MoC procedures for the convergent and divergent sections respectively. The pressure and Mach contours showed a smooth expansion without shock waves. A significant pressure decrease and corresponding Mach increase occurred immediately after the throat, stabilizing downstream with a decrease in the divergence angle.

5. Pressure profiles generated by both methods were found to be very similar. The MoC-based expansion along the centerline displayed a point of discontinuity representing the transition from the throat downstream arc-of-circle to the polynomial profile. It reflects the real nature of the expansion along Mach lines. This discrepancy did not appear in the expansion curve along the wall, where Mach lines merged at the attachment point.

7.1.2. The elliptical profile nozzle

The approach developed that leads to asymmetric nozzles of arbitrary profiles has been applied to design a supersonic contoured nozzle with an elliptical cross-section shape. CFD analysis of the flow-field within this asymmetric elliptical configuration was performed using the FVM in the 'Ansys-Fluent' environment. The obtained results were compared to available experimental data. The results demonstrated a seamless transition from the throat to the nozzle exit cross-section, leading to a steady expansion and a continuous supersonic flow from the throat to the exit, without any signs of shock or separation. The analysis and comparison of the different aspects of the study led to the following conclusions:

1. The results obtained when computing the boundary layer development in the divergent section of the axisymmetric nozzle reflected the generally adopted assumption that the corrections required in order to take into consideration the viscosity effects are negligible. In the case of the CFD computations, the mesh has been heavily refined both downstream of the throat where the gradients are very high and along the walls in order to allow the calculations to be carried out inside the boundary layer.

2. In terms of performances represented essentially by the thrust coefficient as it characterizes the efficiency of the expansion process control by the configuration generated, the axisymmetric configuration performed better than its elliptic counterpart as expected. However and when selecting a final nozzle design, this performance alone cannot be the final determinant. Other requirements, such as the degree of integration mainly represented by the thrust-minus-drag, have to be taken into account. An asymmetric supersonic nozzle design provides excellent integrated aerodynamic performances particularly in the case of air-breathing hypersonic vehicles.

3. Regarding performance, primarily characterized by the thrust coefficient, the axisymmetric configuration outperformed its elliptical counterpart, as expected. However, when finalizing a nozzle design, performance alone cannot be the sole determinant. Other factors, such as integration level, especially represented by thrust-minus-drag, must also be considered. Asymmetric supersonic nozzle designs offer excellent integrated aerodynamic performance, particularly for air-breathing hypersonic vehicles.

7.1.3. The corrugated profile nozzle

The simple and efficient design method developed in the present research investigation has also been applied to the design of a further complex shape. The same original axisymmetric profile

was used to design a corrugated four-petal supersonic single-bell propulsion configuration. Such corrugated nozzles find applications in a wide range of aerospace systems. Moreover and during the development phase of new aerospace vehicles, such configurations are often used in prototypes and experimental vehicles. This allows them to gather data on real-world performance and make necessary adjustments before finalizing the design for production.

The MoC was applied for the design of the original axisymmetric configuration (the same as in the case of the elliptic profile) from which the four-petal nozzle wad subsequently constructed. CFD simulation of the 3-D flow-field was performed, and the obtained results analyzed. The outcomes revealed a seamless shift from the throat to the nozzle exit, generating a consistent expansion and ensuring continuous supersonic flow from the throat to the exit, without any signs of separation

1. In terms of pressure distribution, a sharp expansion is exhibited immediately downstream of the throat before straightening up further downstream leading to directing the flow-field towards the axis of symmetry. In terms of contours, the expansion may be seen behaving in arc-shaped isobars near the throat before deviating further downstream mainly as the result of the asymmetry. The same behavior may be noticed in the case of the Mach contours representation.

2. The acceleration of the flow has been found to be more pronounced in the center core of the corrugated configuration. Within the petals, the expansion may be seen as taking place more slowly. This seems to be the result of the boundary layer that has more influence within the petals than in the center core of the nozzle. Nevertheless, the gradual and constant increase in the flow velocity ensures a smooth expansion to the exit cross-section.

3. The residual set to a stringent value of (10^{-6}) and associated with the universal conservation equation along with the kinetic energy and the dissipation rate of energy led to a convergence within 250 iterations less than that of the elliptic configuration that took 300 iterations.

Finally, the comparison of the results obtained on the developed asymmetric design to the experimental data available leads to conclude the method to suitably achieve arbitrary complex shapes that not only secure the length requirement but also meet the demand of thrust force along with the production of a supersonic section flow conditions that are devoid of shocks and other irregularities.

7.2. Recommendations for further work

The attained results highlight the simplicity of the design, even for intricate shapes, affirming the credibility of the proposed approach for preliminary design of asymmetric nozzles. However, further research and development are essential to fully comprehend the potential benefits and limitations of asymmetric nozzles in enhancing hypersonic engine performance. Further work is necessary to explore their capabilities and refine their applications in hypersonic systems. A variety of interesting arbitrary cross sectional shapes may be generated. Their detailed internal flow analyses would lend further credibility to the procedure outlined.

REFERENCES

Abdelrahman, M., Lee, S., Lee, S., & Kim, Y. J. (2021). Recent progress in design and optimization of multi-grid profile nozzles for supersonic and hypersonic applications: A review. *Aerospace Science and Technology*, *119*, 106358.

Ahuja, K. (1993). Supersonic jet noise reduction by tabs and ejectors. In 15th Aeroacoustics Conference (p. 4347). Published Online: 22 Aug 2012. https://doi.org/10.2514/6.1993-4347

Allman, J. G., & Hoffman, J. D. (1981). Design of maximum thrust nozzle contours by direct optimization methods. *AIAA journal*, *19*(6), 750-751. Published Online: 17 May 2012. https://doi.org/10.2514/3.50999

Anderson, J. D., Tannehill, J. C., Pletcher, R. H., Munipalli, R., & Shankar, V. (2020). *Computational fluid mechanics and heat transfer*. CRC press. https://doi.org/10.1201/9781351124027

Anderson, J. D. (2011). *Fundamentals of Aerodynamics. New Age Science*. McGraw Hill, 6th Ed. ISBN 978-1-259-12991-9

ANSYS, Inc. (2022). Fluent, Release 21.2, ANSYS, Inc.

Arora, S., & Kandula, M. (2020). Contoured nozzle optimization for high-altitude supersonic cruise. *Aerospace Science and Technology, 97*, 105659.

Bajpai, A., & Rathakrishnan, E. (2018). Control of a supersonic elliptical jet. *The Aeronautical Journal*, *122*(1247), 131-147. https://doi.org/10.1017/aer.2017.114

Bani, A. A. (2016). Design and analysis of an axisymmetric aerospike supersonic micro-nozzle for a refrigerant-based cold-gas propulsion system for small satellites. [Master's thesis, University of Missouri]. https://scholarsmine.mst.edu/masters_theses/7591

Benhamouda, R. (2009). Notions de mécanique des fluides, Centre de Publication Universitaire, Tunisie, 203 pages. ISBN : 978-9973-37-494-3

Bian, H., Liu, X., Zhang, L., 2022, Design and performance optimization of a conical supersonic nozzle with an oblique shock wave, *Aerospace Science and Technology*, 124, 106575.

Boussinesq, J. (1877). *Essai sur la théorie des eaux courantes*. Impr. nationale.

Casper, J. L. (2019). Asymmetric supersonic nozzle design for enhanced thrust vectoring, *Journal of Propulsion and Power*, *35*(1), 94-101.

Cauchy, A. L. (1842). Mémoire sur les systèmes d'équations aux dérivées partielles d'ordres quelconques, et sur leur réduction à des systèmes d'équations linéaires du premier ordre. *Comptes Rendus Acad. Sci, 40*, 131– 138.

Chasman, D., Birch, M., Haight, S. & Graffam, R. (2005). A multi-disciplinary optimization method for multi nozzle grid (MNG) design. *In 43rd AIAA Aerospace Sciences Meeting and Exhibit*, 706.

Chasman, D., Haight, S. & Facciano, A. (2005). Excessive nozzle erosion in a multi nozzle grid (MNG) test. *In 41ˢᵗ AIAA/ASME/SAE/ASEE Joint Propulsion Conference & Exhibit*, 4495.

Chasman, D., Haight, S. & Loehr, R. (2012). Viscous losses of MNG in hybrid motor tests. In *48th AIAA/ASME/SAE/ ASEE Joint Propulsion Conference & Exhibit*, 4266.

Choi, J., & Huh, H. (2022). Performance analysis of an expansion-deflection (ED) nozzle based on pintle inflection angle. *Journal of Mechanical Science and Technology*, *36*(12), 6065-6072. https://doi.org/10.1007/s12206-022-1121-7

Choi, J., & Lee, H. (2020). Development of multi-grid nozzle profiles for a solid rocket motor using a genetic algorithm. *Aerospace Science and Technology, 104*, 105981.

Clausius, R. (1865). *The mechanical theory of heat with its applications to the steam engine and to physical properties of bodies*, London: John van Voorst, 1 Paternoster Row.

Cuffel, R. F., Back, L. H., & Massier, P. F. (1969). Transonic flowfield in a supersonic nozzle with small throat radius of curvature. *AIAA Journal*, *7*(7), 1364-1366. Published Online: 17 May 2012. https://doi.org/10.2514/3.5349

Davidson, L. (2003). *An introduction to turbulence models*, Department of thermo and Fluid Dynamics. Chalmer University of Technology, Publication, 97(2), 1-8.

Davis, C.A., & Pappas, M. (2020). Dual-bell rocket nozzle optimization using genetic algorithm with surrogate modelling. *Journal of Spacecraft and Rockets*, *57*(6), 1238-1250.

Du, J., Qian, C., & Zhou, J. (2021). Design and optimization of multi-grid nozzle profiles for a solid rocket motor using surrogate models. *Journal of Aerospace Engineering, 34*(1), 040205.

Du, S., Liu, Y. & Zhang, Z. (2021). Performance evaluation of hypersonic vehicle with asymmetric nozzle under different working conditions, *Aerospace Science and Technology*, 117, 106149.

Dup, D. C., & Rosenbaum, H. (1968). Calculation of the turbulent shear flows through closure of the Reynolds equations by invariant modeling (No. 127). ARAP Report.

Durbin, P. (2017). *Turbulence closure models for computational fluid dynamics*. Aerospace Engineering Publications, Iowa state university. https://lib.dr.iastate.edu/aere_pubs/136

Elger, D. F., Williams, B. C., & Crowe, C. T. (2022). *Engineering Fluid Mechanics*. John Wiley & Sons. ISBN: 978-1-119-82073-4

Elnady, T., & Shyy, W. (2021) Recent advances in contoured supersonic nozzle design and optimization. *Progress in Aerospace Sciences*, *119*, 100668.

Fernandes, T., Souza, A., & Afonso, F. (2023). A shape design optimization methodology based on the method of characteristics for rocket nozzles. *CEAS Space Journal*, 1-13. https://doi.org/10.1007/s12567-023-00511-1

Gabbey, W. A. (1976). Isaac Newton's philosophiae naturalis principia mathematica: The Third Edition (1726) with variant readings. Assembled and edited by Alexandre Koyré and I. Bernard Cohen, with the assistance of Anne Whitman. Cambridge, Mass.(Harvard University Press) and Cambridge (Cambridge University Press). 1972. 916 pp. Historia Mathematica, 3(2), 237-243.

Gilinsky, M., Blankson, I., Gromov, V., & Sakharov, V. (2004, January). Corrugated and composite nozzle-inlets for thrust and noise benefits. In *10th AIAA/NAL-NASDA-ISAS International Space Planes and Hypersonic Systems and Technologies Conference* (p. 1893). Published Online: 22 Aug 2012. https://doi.org/10.2514/6.2001-1893

Goetz, A., Hagemann, G., Kretschmer, J., & Schwane, R. (2005). Advanced upper stage propulsion concept-the expansion-deflection upper stage. In *41st AIAA/ASME/SAE/ASEE Joint Propulsion Conference & Exhibit* (p. 3752). Published Online: 23 May 2012. https://doi.org/10.2514/3.30051

Gu, J. & Li, J. (2020). Aerodynamic performance analysis of a hypersonic vehicle with asymmetric nozzle under different altitudes, *Aerospace Science and Technology*, 104, 105919.

Guo, B., Zhang, M., & Li, X. (2021). Multi-grid profiles nozzle: a review of its research progress and future development. *International Journal of Aerospace Engineering*, 6623657.

Haddad, A. (1988). *Supersonic nozzle design of arbitrary cross-section* [Doctoral thesis, Cranfield Institute of Technology]. http://hdl.handle.net/1826/3512

Haddad, A. (2000). *Aérodynamique interne des prises d'air et tuyères supersoniques.* Intitut d'Aéronautique et des Etudes Spatiales-IAES, Université Blida-1, Algeria.

Haddad, A. & Kbab, H. (2013). Application of de-laval nozzle transonic flow field computation approaches. *International J. of Mechanical, Aerospace, Industrial, Mechatronic and Manufacturing Engineering*, *7*(2), 1093-1098.

Haddad, A. & Moss, J. B. (1990). Aerodynamic design for supersonic nozzles of arbitrary cross section, *Journal of Propulsion*, *6*(6), 740-746. Published Online: 23 May 2012. https://doi.org/10.2514/3.23280

Hagemann, G., Immich, H., Van Nguyen, T., & Dumnov, G. E. (1998). Advanced rocket nozzles. *Journal of Propulsion and Power, 14*(5), 620-634. Published Online: 23 May 2012. https://doi.org/10.2514/2.5354

Hamitouche, T., & Djebbar, O. (2015). Développement d'une méthode de conception de profil de tuyère double galbe (dual-bell nozzles). In *2nd International Conference on Aeronautics Sciences. ICAS-02. November 2015*.

Haque, M.R., Asrar, W. & Gupta, S. (2021). A review of conical supersonic nozzle design and optimization, *Aerospace Science and Technology*, *115*, 106267.

Herring, H. J., & Mellor, G. L. (1972). *Computer program for calculating laminar and turbulent boundary layer development in compressible flow* (No. NASA-CR-2068). NASA.

Hirschfelder, J. O., Curtiss, C. F., & Bird, R. B. (1964). *Molecular theory of gases and liquids.* Molecular theory of gases and liquids. 1964mtgl.book.....H

Hou, X., & Li, R. (2021). Recent development in dual-bell nozzle research: A review, *Aerospace Science and Technology*, *118*, 106272.

Huang, Y., Li, S., & Fan, C. (2021). Design optimization of expansion-deflection nozzle for hypersonic vehicle. *Aerospace Science and Technology*, *111*, 106541.

Khare, S. & Saha, U. K. (2021). Rocket nozzles: 5 years of research and development. *Sådhanå, 46*(76). https://doi.org/10.1007/s12046-021-01584-6

Kim, Y. W., Kim, D. H., & Choi J. H. (2009). Development of the high performance plug nozzle for liquid rocket engine, *Journal of Mechanical Science and Technology*, *23*(12), 3341-3349.

Kliegel, J. R., & Levine, J. N. (1969). Transonic flow in small throat radius of curvature nozzles. *AIAA Journal*, *7*(7), 1375-1378. Published Online: 17 May 2012. https://doi.org/10.2514/3.5355

Kowalevski, S. (1875). Zur Theorie der partiellen Differentialgleichungen. *J. Reine Angew. Math., 80*, 1–32.

Kronecker, L. (1968). [Werke]; *Leopold Kronecker's Werke*. 5. Chelsea Publications.

Krothapalli, A., King, C., & Strykowski, P. (1993). The role of streamwise vortices on the sound generation of supersonic jets. In 15th Aeroacoustics Conference (p. 4320). Published Online: 22 Aug 2012. https://doi.org/10.2514/6.1993-4320

Kumar, S. A., & Rathakrishnan, E. (2016). Characteristics of a supersonic elliptic jet. *The Aeronautical Journal*, *120*(1225), 495-519. https://doi.org/10.1017/aer.2016.7

Kunze, J., Smart, M. K., & Gollan, R. (2022). Design Method for Three-Dimensional Scramjet Nozzles with Shape Transition. *Journal of Propulsion and Power, 1*(38), 3-17. https://doi.org/10.2514/1.B38293

Hsu, Y. G., Hsieh, J. C., & Liao, Y. H. (2021). Plug-type nozzles for rocket engines: A review, *Aerospace Science and Technology*, 115, 106246.

Hunter, C. A. (1998). Experimental, theoretical, and computational investigation of separated nozzle flows. AIAA Paper 98-3107.

Laughrey, J. A., Drape, D. J., & Hiley, P. E. (1981). Performance evaluation of an air vehicle utilizing nonaxisymrnetric nozzles. *Journal of Aircraft*, *18*(2), 89-95. Published Online: 22 May 2012. https://doi.org/10.2514/3.57470

Lee, J., Choi, J., & Huh, H. (2022). Thrust Analysis by Length Reduction of an ED Nozzle with Fixed Expansion Ratio. In *9th European conference for aeronautics and space sciences (EUCASS)* (pp. 1-11). https://doi.org/10.13009/EUCASS2022-7458

Lee, J. H., Choi, Y. H.,. Lee, C. H, & Kim Y. W. (2012). Design optimization of a plug nozzle for a solid rocket motor, *Journal of Propulsion and Power, 28*(5), 918-924.

Li, H., Li, X., & Li, Y. (2018). Numerical simulation and optimization of plug nozzle for reusable rocket engine, *Journal of Aerospace Engineering, 31*(1), 04017062.

Liepman, H. P. (1953). *An analytic design method for a two-dimensional asymmetric curved nozzle.* Project M-951, USAF. https://www.lib.umich.edu/collections/deep-blue-repositories

Liepmann, H. W., & Roshko, A. (2001). *Elements of Gasdynamics*. Courier Corporation. ISBN: 0-486-41963-0

Mahfoudi, E. A., Gahmousse, A., & Talbi, K. (2014). *Contribution à l'étude des profils de tuyères en écoulements supersoniques visqueux par la méthode des volumes finis* (Doctoral dissertation, Université Frères Mentouri-Constantine 1). http://depot.umc.edu.dz/handle/123456789/6458

Marty, D. (1994). *Systèmes spatiaux: conception et technologie*. Masson. ISBN 2-225-84460-7

Matsson, J. E. (2023). An Introduction to Ansys Fluent 2023. Sdc Publications. ISBN-13: 978-1-63057-648-6

Matveev, K. I. & Semenov, V. V. (2021). Numerical study of asymmetric nozzles for scramjet propulsion, *Aerospace Science and Technology*, *116*, 106229.

McDonough, J. M. (2007). Introductory lectures on turbulence: physics, mathematics and modeling. Mech. Engg Textbook Gallery. https://uknowledge.uky.edu/me_textbooks/2

Menter, F. R. (1994). Two-equation eddy-viscosity turbulence models for engineering applications, *AIAA Journal, 32*(8), 1598-1605. Published Online:17 May 2012. https://doi.org/10.2514/3.12149

Migdal, D. (1972). Supersonic annular nozzles. *Journal of spacecraft, 9*(1), 3-6. Published Online: 23 May 2012. https://doi.org/10.2514/3.61623

Mishra, D., & Sinha, A. (2019). Design and optimization of a supersonic contoured nozzle for a ramjet engine. *Aerospace Science and Technology*, *86*, 208-217.

Mo, J., Xu, J., Gu, R., & Fan, Z. (2014). Design of an asymmetric scramjet nozzle with circular to rectangular shape transition. *Journal of Propulsion and Power*, *30*(3), 812-819. https://doi.org/10.2514/1.B34949

Moran, M. J., Shapiro, H. N., Boettner, D. D., & Bailey, M. B. (2014). Fundamentals of Engineering Thermodynamics. Wiley. ISBN 978-1-118-41293-0

Nalim, R., Samuelsen, G.S., 2018, Conical nozzle design for high-altitude rocket flights, *Aerospace Science and Technology*, *80*, 253-260.

Navier, C. L. (1821). Annales de Chimie et de Physique, XIX, 244.

Navier, C. L. (1827). Mémoires de L'Académie Royale des Sciences de L'Institut de France, VI, 389.

Newton, I. (1687). Philosophiae naturalis principia mathematica, (Newton's personally annotated 1st Edition), Londini, Jussu Societatis Regiæ ac Typis Josephi Streater. Prostat apud plures Bibliopolas. https://doi.org/10.4171/RLM/686

O'Leary, R. A., & Beck, J. E. (1992). Nozzle design. Threshold, (8), 34-43.

Pal, S. & Chattopadhyay, H. (2018). Design optimization of asymmetric supersonic nozzle for supersonic combustion ramjet engine, *Aerospace Science and Technology*, *78*, 29-41.

Perrot, Y. (2006). *Etude, mise au point et validation de modèles de turbulence compressible* (Doctoral dissertation, INSA de Rouen).

Prandtl, L. (1926, September). Ueber die ausgebildete Turbulenz. *In Proceedings of the 2nd international congress for applied mechanics*, Zurich, Sep (Vol. 1217, p. 6274).

Preller, D. (2018). Multidisciplinary design and optimisation of a pitch trimmed hypersonic airbreathing accelerating vehicle. [PhD thesis, University of Queensland, Brisbane]. https://doi.org/10.14264/uql.2018.437

Rao, G. V. R. (1958). Exhaust nozzle contour for optimum thrust. *Journal of Jet Propulsion*, *28*(6), 377-382. Published Online: 7 Jun 2012. https://doi.org/10.2514/8.7324

Rao, G. V. R. (1961). Recent developments in rocket nozzle configurations. *ARS journal*, *31*(11), 1488-1494. Published Online: 6 Jun 2012. https://doi.org/10.2514/8.5837

Reynolds, O. (1883). XXIX. An experimental investigation of the circumstances which determine whether the motion of water shall be direct or sinuous, and of the law of resistance in parallel channels. *Philosophical Transactions of the Royal society of London*, (174), 935-982. https://doi.org/10.1098/rstl.1883.0029

Reynolds, O. (1895). IV. On the dynamical theory of incompressible viscous fluids and the determination of the criterion. *Philosophical Transactions of the Royal Society of London*. (a.), (186), 123-164. https://doi.org/10.1098/rsta.1895.0004

Rizal, M., Razak, M. A., & Mustapha F. (2018). Performance analysis of a conical nozzle for a small-scale rocket propulsion system. *Aerospace Science and Technology*, *72*, 153-160.

Roy, V. P., Kriparaj, K. G., Tide, P. S., & Biju, N. (2022). Effect of Lobe Count and Lobe Length of Corrugated Lobed Nozzle on Subsonic Flow Characteristics. *Journal of Applied Fluid Mechanics*, *16*(2), 353-361. https://doi.org/10.47176/JAFM.16.02.1269

Rylov, A. I. (1976). Analysis of some supersonic nonsymmetric nozzles. *Fluid Dynamics*, *11*(3), 477-479. https://doi.org/10.1007/BF01014473

Rylov, A. I. (1977). Design of supersonic asymmetric nozzles. *Fluid Dynamics*, *12*(3), 414-420. https://doi.org/10.1007/BF01050573

Sasaki, K., Nakamura, Y., & Hasegawa, T. (2017). Design optimization of three-dimensional multi-grid profiles nozzle for high-altitude rocket engine. *Journal of Spacecraft and Rockets, 54*(6), 1261-1271.

Schlichting, H., & Gersten, K. (2016). Boundary-layer theory. springer.

Shen, Y., Gao, M., & Chang, S. (2019). Numerical investigation of plug nozzle performance using adaptive mesh refinement, *Aerospace Science and Technology*, *94*, 105415.

Shin, S., & Jeong, S. (2015). Numerical investigation of plug nozzle flow characteristics for a small-scale rocket engine, *International Journal of Aeronautical and Space Sciences, 16*(4), 397-406.

Schomberg, K., Olsen, J., & Doig, G. (2015). Analysis of a low-angle annular expander nozzle. *Shock and Vibration*, *2015*. https://doi.org/10.1155/2015/675861

Schomberg, K., Olsen, J., Neely, A., & Doig, G. (2014, December). Experimental analysis of a linear expansion-deflection nozzle at highly overexpanded conditions. In *19th Australasian Fluid Mechanics Conference* (pp. 74-77).

Schorr, C. J. (1970). Constant chamber pressure throttling of an expansion-deflection nozzle. *Journal of Spacecraft and Rockets*, *7*(7), 843-847. Published Online: 23 May 2012. https://doi.org/10.2514/3.30051

Silbey, R. J., Alberty, R. A. Papadantonakis, G. A. & Bawendi, M. G., (2021). Physical Chemistry, 5th ed., Wiley. ISBN 978-0-470-56660-2

Stokes, G. G. (1880), On some cases of fluid motion, Mathematical and Physical Papers by George Gabriel Stokes, Cambridge University Press, Cambridge, 17-68.

Sutherland, W. (1893). LII. The viscosity of gases and molecular force. *The London, Edinburgh, and Dublin Philosophical Magazine and Journal of Science, 36*(223), 507-531. https://doi.org/10.1080/14786449308620508

Sutton, G. P., & Biblarz, O. (2016). Rocket propulsion elements. John Wiley & Sons. ISBN: 978-1-118-75388-0

Thangaraj, T., & Kaushik, M. (2023). Effects of circular and non-circular nozzle exit geometries on subsonic and supersonic jet propagations. *Proceedings of the Institution of Mechanical Engineers, Part G: Journal of Aerospace Engineering*, *237*(1), 209-229. https://doi.org/10.1177/09544100221097537

Uyeki, D. Y. K. (2018). A design method for a supersonic axisymmetric nozzle for use in wind tunnel facilities. *MSc in Aerospace Engg, Dept of Aerospace Engg, Dan José University*, *201*.

Van der Waals, J. D. (1910). The equation of state for gases and liquids. Nobel lectures in Physics, 1, 254-265.

Verma, M., Arya, N., & De, A. (2020). Investigation of flow characteristics inside a dual bell nozzle with and without film cooling. *Aerospace Science and Technology*, *99*, 105741. https://doi.org/10.1016/j.ast.2020.105741

Vianna Moizes, D. A., Kotler, A. R., Thornton, M. R., & Ahmed, K. A. (2023). Comparison and Analysis of Hypersonic Scramjet Nozzles. In *AIAA SCITECH 2023 Forum* (p. 0716). Published Online: 19 Jan 2023. https://doi.org/10.2514/6.2023-0716

Wada, T., Fujita, K., & Tsujimoto, T. (2017). Design optimization of a dual-bell nozzle for a reusable rocket engine. *Journal of Spacecraft and Rockets*, *54*(6), 1213-1223.

Ward, A. (2022). Aftbody design of winged-cone derived hypersonic vehicles. [PhD thesis, University of Queensland, Brisbane]. https://doi.org/10.14264/ee04424

Winarto, H., & Stalker, R. J. (1984). Design parameters and performance of two-dimensional, asymmetric, 'sliding block', variable Mach number, supersonic nozzles. *The Aeronautical Journal*, *88*(876), 270-280. Published online: 04 July 2016. https://doi.org/10.1017/S0001924000020625

Yahya, S. M. (2006). *Gas tables for compressible flow calculations*. New Age International. ISBN 81-224-1555-5

Yahya, S. M. (2010). Fundamentals of compressible flow: with aircraft and rocket propulsion. New Age Science, 4th Ed. ISBN 978-1-906-57432-1

Yang, L., Huang, Y. & Chen, X. (2021). Effects of asymmetric nozzle on aerodynamic heating of a hypersonic vehicle, *Aerospace Science and Technology*, *118*, 106162

Yang, X., Li, L., & Li, J. (2020). A review of multi-grid profiles nozzle research for supersonic and hypersonic propulsion, *Chinese Journal of Aeronautics*, *33*(11), 2354-2367.

Yunpeng, W. A. N. G., & Zonglin, J. I. A. N. G. (2021). A review of theories and methods for hypersonic nozzle design. *Advances in Mechanics*, *51*(2), 257-294. https://doi.org/10.6052/1000-0992-20-002

Zhao, J., Fan, C., Li, S., & Li, W. (2022). Parametric study of a 3D expansion-deflection nozzle with two-dimensional optimization. *Aerospace Science and Technology*, *126*, 106731.

Zhu, M., Fu, L., Zhang, S., & Zheng, Y. (2018). Design and optimization of three-dimensional supersonic asymmetric truncated nozzle. *Proceedings of the Institution of Mechanical Engineers, Part G: Journal of Aerospace Engineering*, *232*(15), 2923-2935. https://doi.org/10.1177/0954410017718567

Zucrow, M. J., & Hoffman, J. D. (1977). Gas dynamics. Volumes 1 & 2 2. *Jonh Wiley & Sons*, *New York*.

_____

Appendix A:

IMPLEMENTATION OF THE MOC TO A STEADY, INVISCID AND AXISYMMETRIC FLOWFIELD

A.1 : Governing equations

The MoC is generally applied for the solution of hyperbolic-type differential equation that govern the supersonic flow-field taking place within the divergent section of a C-D nozzle. The equations governing such a steady, isentropic, irrotational flow of an inviscid fluid may be expressed as:

$$\left(u^2 - a^2\right)\frac{\partial u}{\partial x} + \left(v^2 - a^2\right)\frac{\partial v}{\partial y} + 2uv\frac{\partial u}{\partial y} - \delta\frac{a^2 v}{y} = 0 \tag{2.124}$$

$$\frac{\partial u}{\partial y} - \frac{\partial v}{\partial x} = 0 \tag{2.125}$$

where: $\delta = 1$ for an axisymmetric flow-field,

$\delta = 0$ for a plane flow-field.

A.2 : Characteristic and compatibility equations

In the case of a supersonic flow, i.e. $\left(\dfrac{u^2 + v^2}{a^2} \succ 1\right)$, the equations are of hyperbolic form and the method of characteristics can therefore be applied. Moreover, Equation 2.124 and Equation 2.125 being coupled have to be solved simultaneously. The characteristic equation and the compatibility equation are derived by first multiplying these equations by the unknowns (σ_1) and (σ_2). Summing and arranging results in:

$$\sigma_1\left(u^2 - a^2\right)\left[\frac{\partial u}{\partial x} + \frac{\sigma_1(2uv) + \sigma_2}{\sigma_1\left(u^2 - a^2\right)}\frac{\partial u}{\partial y}\right] + \left(-\sigma_2\right)\left[\frac{\partial v}{\partial x} + \frac{\sigma_1\left(v^2 - a^2\right)}{-\sigma_2}\frac{\partial v}{\partial y}\right] - \frac{\sigma_1\delta a^2 v}{y} = 0 \tag{2.127}$$

The development performed in section 2.6 led to the characteristic equation that defines two kinds of characteristics (one called the left-hand characteristic and the other called the right-hand characteristic that are in fact the Mach lines as represented in Figure A-1):

$$\lambda_{\pm} = \left.\frac{dy}{dx}\right|_{\pm} = tg\left(\theta \pm \alpha\right) \tag{2.135}$$

And the compatibility equation that is also a total differential equation:

$$\left(u^2 - a^2\right)du_{\pm} + \left[-\left(u^2 - a^2\right)\lambda_{\pm} + 2uv\right]dv_{\pm} - \left(\delta\frac{a^2 v}{y}\right)dx_{\pm} = 0 \tag{2.137}$$
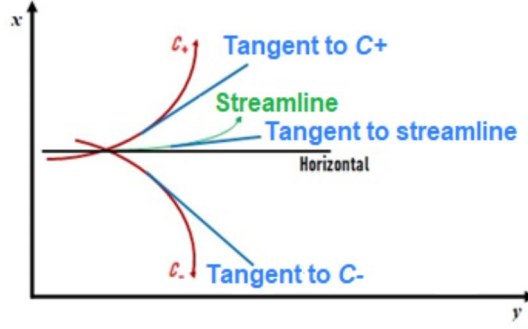
Figure A-1: Representation of the streamline along with the right-and and left-hand characteristics

The characteristic and compatibility equations are non-linear total difference equations. Their solution is obtained through the application a finite difference procedure. The resulting mesh will replace the characteristic portion connecting two nodes with straight line segments. The numerical integration is carried out using the modified Euler predictor-corrector algorithm. According to this method, the finite difference equations corresponding to Equation 2.135 and Equation 2.137 are obtained by replacing (dx), (dy), (du) and (dv) by the differences (Δx), (Δy), (Δu) and (Δv). Therefore:

$$
\begin{cases}
(a) & \Delta y_{\pm} = \lambda_{\pm} \Delta x_{\pm} \\
(b) & Q_{\pm} \Delta u_{\pm} + R_{\pm} \Delta v_{\pm} - S_{\pm} \Delta x_{\pm} = 0 \\
(c) & \lambda_{\pm} = tg(\theta \pm \alpha) \\
(d) & Q = u^2 - a^2 \\
(e) & R = 2uv - \left(u^2 - a^2\right)\lambda \\
(f) & S = \delta \dfrac{a^2 v}{y}
\end{cases}
\tag{2.138}
$$

The area where the flow takes place in the divergent section needs to be divided into specific nodes. These nodes include those within the flow (internal nodes), along the axis of symmetry (axial nodes) and on the wall (wall nodes). The approach to finding a solution varies based on these node positions.

A.3 : Procedure for an internal node

In the case of an internal node localized by its coordinates (x_4) and (y_4) in Figure A-2, the procedure will result in Equations A-1 derived from Equation 2.138-a:

$$
\begin{cases}
y_4 - \lambda_+ x_4 = y_2 - \lambda_+ x_2 \\
y_4 - \lambda_- x_4 = y_1 - \lambda_- x_1
\end{cases}
\tag{A-1}
$$

The slopes of the characteristics (C_+) and (C_-) noted (λ_+) and (λ_-) are defined by the application of Equation 2.138-c:

$$
\begin{cases}
\lambda_+ = tg(\theta + \alpha) \\
\lambda_- = tg(\theta - \alpha)
\end{cases}
\tag{A-2}
$$

where: $\theta_{\pm} = tg^{-1}\left(\dfrac{v_{\pm}}{u_{\pm}}\right)$; $\alpha_{\pm} = \sin\left(\dfrac{1}{M_{\pm}}\right)$; $M_{\pm} = \dfrac{V_{\pm}}{a_{\pm}}$; $V_{\pm} = \sqrt{u_{\pm}^2 + v_{\pm}^2}$; $a_{\pm} = a\left(V_{\pm}\right)$ (A-3)
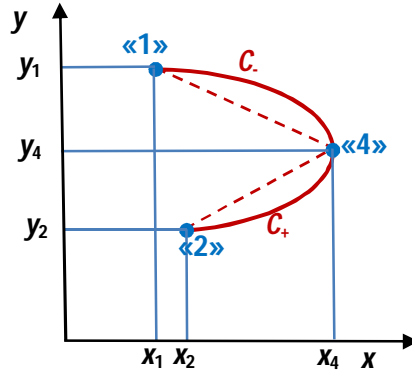
Figure A-2: Internal node solution procedure

It therefore comes out that $(\theta_\pm)$, $(\alpha_\pm)$ and therefore $(\lambda_\pm)$, will be determined for specific values of the two velocity components (u_4) and (v_4) that would be determined from the solution of Equation 2.138-b that can be written as:

$$\begin{cases} Q_+ u_4 + R_+ v_4 = T_+ \\ Q_- u_4 + R_- v_4 = T_- \end{cases} \tag{A-4}$$

with:

$$\begin{cases} T_+ = S_+ \left(x_4 - x_2 \right) + Q_+ u_2 + R_+ v_2 \\ T_- = S_- \left(x_4 - x_1 \right) + Q_- u_1 + R_- v_1 \\ Q_+ = u_+^2 - a_+^2 \\ Q_- = u_-^2 - a_-^2 \\ R_+ = 2u_+ v_+ - Q_+ \lambda_+ \\ R_- = 2u_- v_- - Q - \lambda_- \\ S_+ = \delta \dfrac{a_+^2 v_+}{y_+} \;\; ; \;\; S_- = \delta \dfrac{a_-^2 v_-}{y_-} \end{cases} \tag{A-5}$$

For specific values of $(u_\pm)$, $(v_\pm)$ and $(y_\pm)$, the parameters $(Q_\pm)$, $(R_\pm)$, $(S_\pm)$ and $(T_\pm)$ are determined. Equation A-1 and Equation A-4 lead to the application of the numerical integration procedure.

A.4 : Numerical integration procedure

The numerical integration procedure applies the Euler's predictor-corrector algorithm. The predictor step is represented by:

$$\begin{cases} u_+ = u_2 \; ; \; v_+ = v_2 \; ; \; y_+ = y_2 \\ u_- = u_1 \; ; \; v_- = v_1 \; ; \; y_- = y_1 \end{cases} \tag{A-6}$$

This will determine (x_4^0), (y_4^0), (u_4^0) and (v_4^0). The corrector step will be applied by setting:

$$u_+ = \frac{u_2 + u_4^0}{2} \; ; \; v_+ = \frac{v_2 + v_4^0}{2} \; ; \; y_+ = \frac{y_2 + y_4^0}{2} \; ; \; u_- = \frac{u_1 + u_4^0}{2} \; ; \; v_- = \frac{v_1 + v_4^0}{2} \; ; \; y_- = \frac{y_1 + y_4^0}{2} \tag{A-7}$$

The corrector step is applied iteratively. It would lead to the computation of (x_4^1), (y_4^1), (u_4^1) and (v_4^1) and in a next phase (x_4^2), (y_4^2), (u_4^2) and (v_4^2) … etc. The corrector step is applied as many times as necessary until the required tolerance represented by $|P^{n-1} - P^n| \leq$ error, (P) representing (x_4), (y_4), (u_4) or (v_4).

A.5 : Procedure for other nodes

A similar procedure is applied to the other nodes such as the axis of symmetry node, the direct wall and inverse nodes and some particular cases (Haddad, 1988).

———————————————————
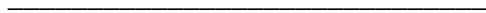
Appendix B:

ELLIPTIC NOZZLE SUBSONIC SECTION DESIGN

B.1 : Introduction

The subsonic section of a C-D nozzle has for essential mission the gradual acceleration of the incoming combustion gases from low subsonic velocities to sonic velocities. This is performed through narrowing down the flow passage gradually until the throat where the velocity should attain that of the sound. Therefore, its design is critical to achieving the desired flow conditions and lead thr supersonic expansion that takes place in the supersonic section.

B.1 : Elliptic subsonic section design

The throat being elliptic, and the incoming pipe used to transport the air under pressure (cf. Appendix C) being circular, the subsonic section should move the geometry from elliptic to circular. This is performed through a series of circles that start at the throat to reach the circular inlet of the subsonic section that would connect, through a flange, to the supplying pipe. Figure B-1 represents such circles.
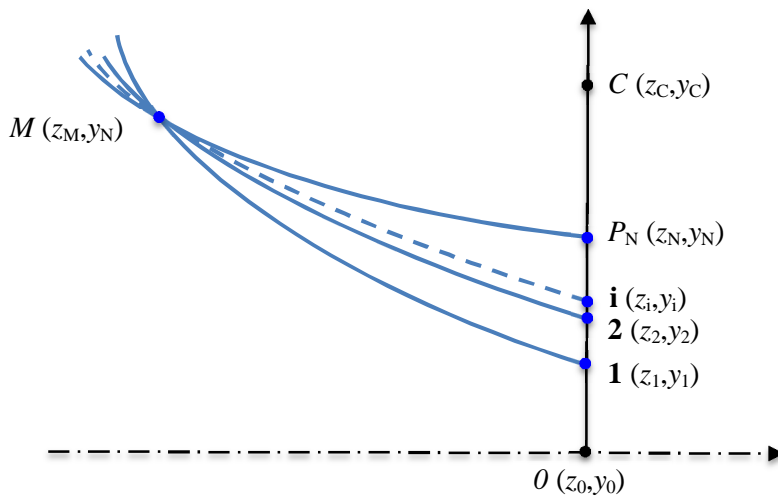

Figure B-1: Subsonic section design moving from elliptic to circular

The arcs of circle shaping the subsonic convergent section of the elliptical nozzle are expressed by Equation B-1 and Equation B-2. As the points (**i**) and (**M**) belong to the same circle, we can write:

$$\left(z_i - z_{oc}\right)^2 + \left(y_i - y_{oc}\right)^2 = R_i^2 \tag{B-1}$$

$$\left(z_M - z_{oc}\right)^2 + \left(y_M - y_{oc}\right)^2 = R_i^2 \tag{B-2}$$

---

with: - $z_{oc} = 0$ representing the distance along the axis from the circle's center to the coordinate system's origin.

    - $z_i = 0$

    - z_M, y_M these dimensions are specified by the inlet section that ensures the alignment with the exit of the supplying pipe.

The simultaneous solution of Equation B-1 and Equation B-2 leads to defining the ordinate of the circle of center (C) in Figure B-1 as:

$$y_{oc} = \frac{y_M^2 + z_M^2 - y_i^2}{2(y_M - y_i)} \tag{B-3}$$

$$R_i = |y_i - y_{oc}| \tag{B-4}$$

In terms of the coordinate system $(0,z,y)$, the general relationship describing a circle may be expressed as:

$$(z - z_{oc})^2 + (y - y_{oc})^2 = R_i^2 \tag{B-5}$$

Replacing (y_{oc}) and (z_{oc}) by their relationships expressed in Equation B-3 and Equation B-4 respectively leads to the final expression of the series of circles linking the elliptical throat to the circular supplying pipe:

$$z^2 + \left[y - \frac{y_M^2 + z_M^2 - y_i^2}{2(y_M - y_i)} \right]^2 = (y_i - y_{oc})^2 \quad ; \quad i = 1, N \tag{B-6}$$

Thirteen circles have been used to define the subsonic section linking the elliptical throat to the circular supplying pipe.

_____

Appendix C:

EXPERIMENTAL APPARATUS

C.1 : Introduction

The results obtained through performing CFD computations on the elliptical cross-section nozzle (section 6) have been compared to the experimental results performed on a similar nozzle (Haddad & Moss, 1990), the intention being to provide a simple proof-of-concept.

C.2 : Experimental Methodology

The experiments were carried out in an open jet-test arrangement as shown in Figure C-1. The pressurized air was delivered from compressors through a flow meter and a pressure regulating valve. A flange enables a tight connection between the supplying pipe and the inlet section of the nozzle convergent section.
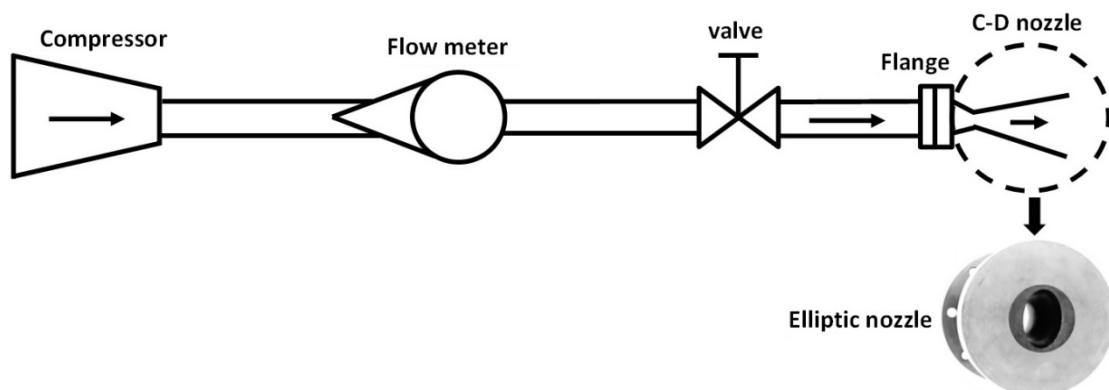

Figure C-1: Schematic layout of the supersonic test arrangement

The external body of the elliptic configuration was manufactured. Machined in an aluminum alloy with a tolerance of 0.1 mm, it supports the internal shape which was cast in Araldite MY-750 (an epoxy resin filled with aluminum) that achieves the necessary finish (N7) therefore avoiding any protuberance in the surface that may disturb the flow within either the subsonic or the supersonic sections. The hardener used is HT-972 that allows a maximum working temperature 130°C (Figure C-2).

The pressure readings were taken at different evenly distributed stations along the centerline of the nozzle, as well as along the major and minor axes of the elliptic nozzle exit. Two probes were used, an internal pressure probe for the measurement of the pressure along the centerline and an external one for the measurement of the pressure along the exit cross-section major and minor axes. These experimental data were compared to the CFD results (cf. section 6.2.4). These measurements were conducted under the specified design conditions that have been recorded and used for carrying

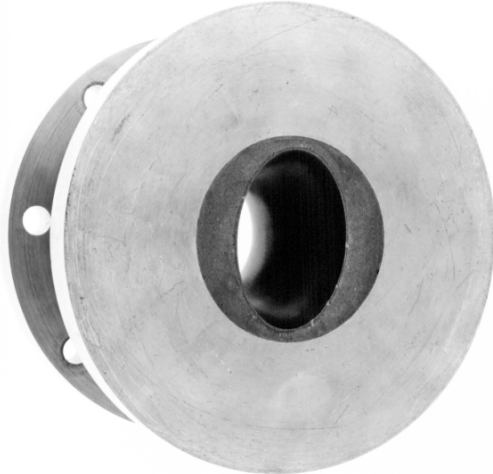out the CFD computations. The inlet pressure, ambient temperature, and mass flow rate were also recorded.

Figure C-2: The elliptical nozzle showing the exit section and the bores used to connect the nozzle to the flange

_____

Appendix D:
ANSYS-FLUENT PLATFORM

D.1 : Introduction

'ANSYS Fluent' is a CFD software tool widely used for simulating a variety of fluid flow phenomena, including supersonic steady turbulent viscous flows. 'Fluent' provides a powerful and flexible environment for modeling, simulating, analyzing and visualizing various complex fluid flow behaviors.

D.2 : Fundamental equations solved

In steady viscous turbulent supersonic flow simulations like those used in the present research, 'ANSYS Fluent' solves the fundamental governing equations of fluid dynamics and turbulence modeling. They include:

- The equation of mass conservation or continuity that ensures the mass balance in the flow, and may be expressed as:

$$\nabla \cdot V = 0$$

- The equation of momentum conservation described by the Navier-Stokes equations that accounts for the motion and forces in the fluid. It may be expressed as:

$$\rho C_p \left(\frac{\partial V}{\partial t} + V \cdot \nabla V \right) = -\nabla P + \mu \nabla^2 V + \rho g$$

- The equation of energy conservation that accounts for the thermal aspects of the flow i.e. heat conduction, convection, and viscous dissipation effects. It may be expressed as:

$$\rho C_p \left(\frac{\partial T}{\partial t} + V \cdot \nabla T \right) = \nabla \cdot \left(k \nabla T \right) + \dot{q}$$

- The turbulence modeling with various turbulence models being available for use. These models, such as the RANS equations which include turbulence closure models like k-epsilon (k-ε) or k-omega (k-ω) or a combination of the two known as the called the k-omega shear stress transport (sst k-ω), add extra equations to account for turbulent viscosity and model the effects of turbulence on the flow.

- The equation of state appropriate for compressible flows which, for ideal gases, is represented by the ideal gas law:

$$P = \rho RT$$

where: T : is the temperature ; C_p : is the specific heat at constant pressure

k : is the thermal conductivity ; $\dot{q}$: any internal heat generation or absorption

P : is the pressure ; ρ : is the density ; R : is the gas constant

---

D.3 : Modules f Ansys Fluent

ANSYS Fluent is organized into different modules, each serving a specific purpose within the simulation process. The primary sections are:

- Preprocessing : integrates **geometry modeling** and **meshing**. The geometry modeling section allows users to create or import complex 3D geometries, and includes the necessary tools for geometry creation, modification, and cleanup. The meshing module provides tools for generating structured or unstructured meshes. It supports various mesh element types, boundary layer meshing, and mesh refinement techniques.

- Solver Setup : Integrates the **boundary conditions** that the user defines. Examples of boundary conditions include the inlet, the outlet, the wall as well as other various boundary conditions for the simulation. It also includes the **solver settings** that allow users to select the appropriate solvers, specify the numerical methods, and set the convergence criteria. Finally, the solver setup covers the different **turbulence models** that the user can choose from in order to capture turbulence effects.

- Solution : This section initiates the **simulation** process based on the defined setup presented above, iteratively solving the governing equations until convergence. While the solution is initiated, users can **monitor** its progress, check residuals, and intervene if necessary to ensure the simulation is proceeding correctly.

- Post-Processing : Within this section, **visualization** tools are provided for creating contour plots, vector plots, animations, streamline … etc. Quantitative **data can be extracted**, such as performance metrics can be extracted in order to be visualized or in order to **generate graphs and reports**.

- Additional modules : Additional sections, such as multiphase modeling, combustion modeling and heat transfer, are offered along with an adjunct solver that allows for sensitivity analysis and optimization.